Design of Vibration Tolerant Microelectrodes and Field Effect Characterization of MoS_2

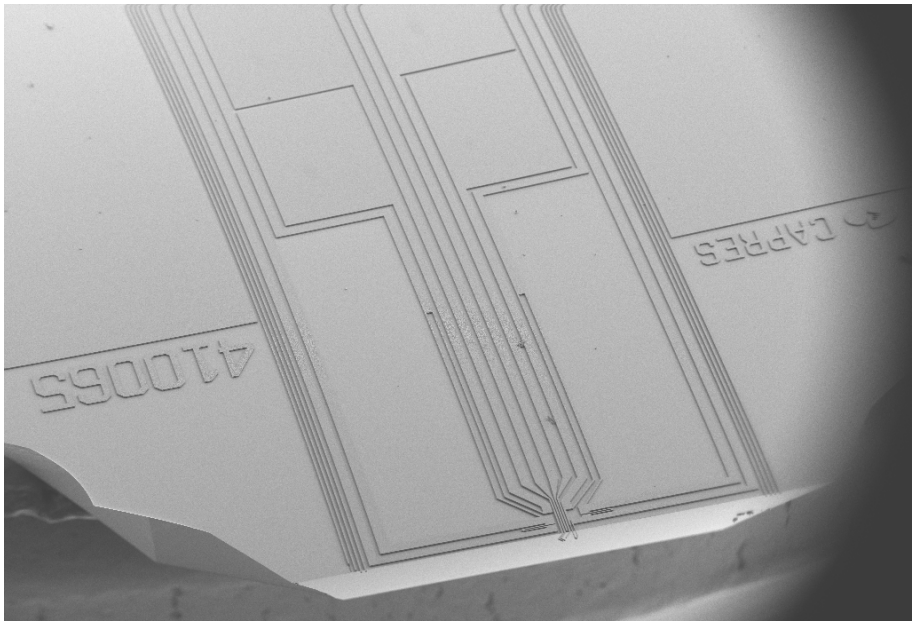

Kristoffer Gram Kalhauge

Supervisors
Senior Researcher, Dirch Hjorth Petersen
Professor, Peter Uhd Jepsen
Professor Emeritus, Ole Hansen

Group: Nanoelectronics Metrology

DTU Physics
PhD Thesis
The Technical University of Denmark 30-11-2019

Abstract

Since the industrial revolution metrology has played and important role behind the scene. With the invention of the transistor and later the development of modern integrated circuits, that role has only become more and more important. One of the key methods in electrical characterization is the four-point measurement. Where four contacts are made to a sample, these are then used to pass a current between two of them and measure the corresponding potential drop across the other two. As the critical dimension shrunk, first below a micrometer and then to the nanometer-scale, the traditional four point probe became increasingly unsuited for the job. Micro four-point probes, consisting of electrodes on the micrometer scale, have since been a viable and often superior alternative.

Several different measuring methods have been developed using the micro four-point probe. Including micro Hall, sheet resistance measurements and measurements on ultra-shallow junctions.

In this thesis the governing mechanics of cantilevers, consisting of two beams joint at an angle, is derived. This is then used to optimize an existing cantilever to achieve a higher tolerance to vibrations. In order to do this an expression for the vibration tolerance is derived and tested. Based on the existing cantilever, two new designs are found. Not only does the new designs improve the mechanical performance by a factor of two or more. But they achieve this while either keeping the minimum pitch or decreasing it from 1.5µm to 1.1µm.

This thesis also presents the use of micro four-point probes to perform field effect measurements on two dimensional materials. Only a single crystal basis thick, these materials form large continues flakes that in bulk are held together by van der Waals forces. However, it is their properties as a single or a few layer materials that is of interest in the development of electronics. The most known of these is graphene. With a high mobility and semi-metallic electron behavior. Graphene has seen its introduction in everyday electronics already. Due to its conductive nature its uses in many devices are limited. Alternatively, other materials such as transition metal dichalchoginites show interesting physical attributes. And, the one studied in this thesis (molybdenum disulfide - MoS_2) is a semiconductor, making it interesting as a transistor material. To measure on this material a microRSP-M200 tool from CAPRES, was modified so that it could source voltage in DC.

On this modified setup field effect measurements were successfully performed, allowing for the measurement of threshold voltage and field effect mobility on the material. A precision of the measured current within the same engage of 10% was achieved.

Resumé

Metrologi har spillet en vigtig rolle siden den industrielle revolution. Opfindelsen af transistoren og senere det integreret kredsløb, har kun gjort metrologi endnu vigtigere. En af de vigtigste metoder inde for elektriskkarakterisering er fire punktmålingen. Som den kritiske dimension blev mindre og mindre, så blev brugbarheden af traditionelle fire punktmålinger også mindre. Mikro fire punktmålinger er en metode der benytter elektroder på mikrometer skala, i stedet for millimeter skala. Denne metode er blevet brugbart og ofte bedre alternativ til den traditionelle fire punktmåling.

Der eksisterer allerede en række metoder der bygger på mikro fire punktmålinger, så som mikro Hall, flademodstandsmålinger og målinger på ultra-shallow junctions.

I denne afhandling er den underliggende mekanik for to bjælke kantilevere, en elektrode type benyttet i mikro fire punktmålinger, udledt og brugt til at optimere designet af eksisterende prober, så de kan modstå større vibrationer. To nye designs er fremlagt, det ene beholder den samme elektrodeafstand og det andet mindsker elektrodeafstanden fra 1,5µm til 1,1µm. For at kunne gøre dette er der blevet udviklet og testet et udtryk for vibrationstolerancen.

Denne afhandling præsenterer også brugen af mikro fire punktmålinger til at foretage felteffekts målinger på todimensionale materialer. Disse kommer fra en familie af materialer som består af lag et atom tykt, som er holdt sammen med van der Waals kræfter. Det todimensionale materiale er et enkelt af disse lag. Det mest velkendte af disse materialer er grafen, som består af karbon i en heksagonal krystal. Mange todimensionale materialer udviser interessante egenskaber og det materiale, der er studeret i denne afhandling (molybdæn disulfid – MoS_2) er en halvleder, hvilket gør den interessant som en transistor. For at kunne måle på dette materiale, var et microRSP-M200 tool fra CAPRES ændret til at kunne levere en jævnspænding.

På dette modificerede udstyr er det lykkedes at fortage felteffekt målinger, og dermed at måle tærskelspændingen of felteffektmobiliteten for materialet. En præcision på 10% i den samme måling blev opnået

Preface

I would like to thank the all the people that helped me during this project. In particular I would like to thank my supervisors Dirch Petersen and Peter Jepsen, for supervision and guidance. Where Dirch as my main supervisor, has been a great help and support through the past three years. I also want to thank Ole Hansen, that with his wast knowledge has more than once aided me past problems that otherwise seemed unmanageable. David Mackenzie and Henrik Henrichsen, for their help with building my measurement setup. Hans Henrik Jankjær and Mette Balslev for help with all the small technical stuff that comes up. Abhay Shivayogimath and Tim Booth, for their help with getting samples to measure on, and for going out of their way to help me. Lior Shiv for great conversations on the mechanics of cantilevers, and exchanging ideas on their design. Maria Witthøft for tolerating my weird antics, sharing an office for two and a half years, and generally making work a more amusing place to be.

A special thanks to CAPRES for letting me borrow and modifying their microRSP-M200 tool.

Finally, thanks to the entirety of my group for three hard but good years.

Kristoffer Kalhauge
Kgs. Lyngby, 14th of October 2019

This project has received funding from the European Union's Horizon 2020 research and innovation program under grant agreements Nos. 692527.

Contents

Acronyms

2B Two-Beam 17

2D Two Dimensional 2

BOX Buried Oxide Layer 3

CD Critical Dimension 38

CVD Chemical Vapor Deposition 3

FET Field Effect Transistor 9

ITO Indium-Tin-Oxide 34

M4PP Micro Four-Point Probe 1

M7PP Micro Seven-Point Probe 48

MoS_2 Molybdenum Disulfide 2

MOSFET Metal-Oxide-Semiconductor Field-Effect Transistors 3

Ψ-MOSFET Pseudo-Metal-Oxide-Semiconductor Field-Effect Transistor 3

PCB Printable Circuit Board 49

SEM Scanning Electron Microscope 1

SOI Silicon-on-Isolator 3

TMD Transition Metal Dichalcogenide 2

vdP van der Pauw 6

1 | Introduction

In modern physics and engineering metrology plays a key role in measuring and quantifying the world around us. And, as tolerances becomes tighter and requirements higher, the need for metrology also increases. There are few places where this is more evident than in micro- and nanoelectronics. In more than 50 years the number of transistors in integrated circuits have roughly doubled every two years [1]. This corresponds to around 32 million times the number of transistors in a computer today compared to 1970. In order to make room for all these new transistors their size have had to go down. This has happened to a degree where the critical dimension for commercially available chips have reached sub 10nm. This exponential miniaturization of components has meant that good metrology have moved from a benefit, to a necessity [2].

1.1 Micro Four-Point Probe

Four-point measurements have existed for more than a century [3], and have since its inception become the method of choice for precise electrical measurements, as well as being the standard in the semiconductor industry for the past 61 years [4]. Since then the four-point probe have developed into the Micro Four-Point Probe (M4PP) [5, 6]. This have allowed four-point measurements to measure on fragile and thin materials [7], but also just to measure on smaller areas which taken to the extreme have allowed for four-point measurements directly on fin-structures [8].

There are multiple variants of M4PP including but not limited to: all metal cantilevers [9], metal coated polymer cantilevers [10], monocantilevers where all four electrodes are on the same cantilever [11], probes were the individual electrodes can move compared to each other [12] and the designs considered here. These designs consists of four cantilevers connected to a common probe-body. The cantilevers are made out of either silicon dioxide or poly silicon with a metal coating on one side to form the electrical contact [6, 13]. A Scanning Electron Microscope (SEM) micrograph of a commercially available M4PP from CAPRES is shown in Figure 1.1.

Through the use of lock-in amplification, advanced algorithms for data treatment [14] and automatic configuration switching. The M4PP has through the past 10 years become the most reliable electrical method available for characterization of ultra-thin semiconductors [15, 16, 17]. Were both sheet resistance [18], magnetoresistance measurements [19] and micro Hall effect measurements [13, 20] are possible.

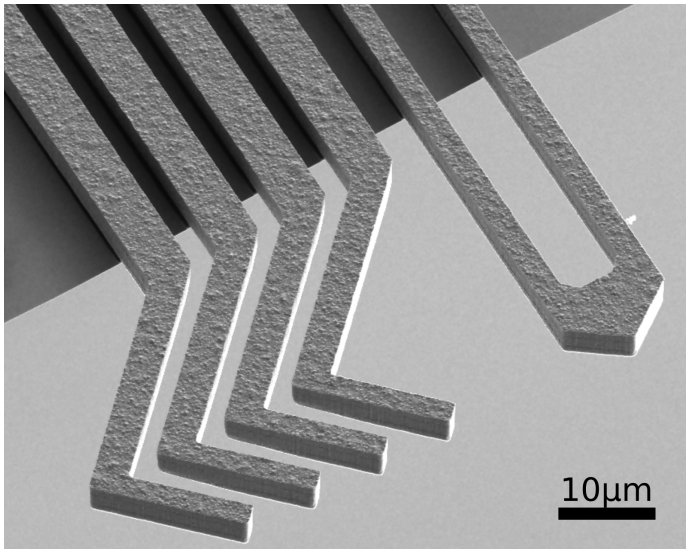

Figure 1.1: SEM micrograph of an L-shaped M4PP. The four L-shaped electrodes used for measuring is shown on the left. The cantilever on the right, that looks like two cantilevers joint at the tip, is a strain gauge.

1.1.1 Stability at the Nanometer Scale

When performing M4PP measurements it is very important that the electrodes stay in place on the surface for the duration of the measurement. Since any movement during measurement leads to measurement errors [21]. Depending on what is measured this could be measured in seconds, or as will be shown in this thesis tens of minutes. A lot of work have gone into removing the impact of static positioning errors, i.e. errors from all electrodes not being in the nominal position, that occurs during an engage, but does not change during the engage [21, 22]. Dynamic positioning errors on the other hand, can be estimated for a measurement but cannot be removed analytically [21]. Dynamic positioning errors are most likely caused by vibrations in the system. To counter act this, the L-shaped cantilever was introduced [23, 24]. Since then the minimum electrode pitch have become an issue, were more closely packed probes are desired. Consequently, probes with a smaller angle on the bend have been introduced [14]. But, without a theoretical understanding of their mechanical behavior direct comparisons have been difficult. The idea of a measure of the vibration tolerance for micro electrodes was discussed in the D. H. Petersen's PhD thesis [25] and has since then been expanded and formalized during this PhD study [26].

1.2 Two Dimensional Materials

Since the introduction of graphene in electronics [27, 28, 29], several new Two Dimensional (2D) materials have been discovered [30]. Among these are the family of materials know as the 2D Transition Metal Dichalcogenide (TMD) [31]. Where graphene is semi-metallic or metallic in nature many of the TMDs are semiconductors [32]. One of these TMDs is Molybdenum Disulfide (MoS_2), a material that, just like graphene, can be found in abundance in nature, in the form of molybdenite crystals [33], which can be exfoliated to stable mono-layer materials [34]. With its direct band-gap of 1.8eV and high mobility of up

to 200 $cm^2V^{-1}s^{-1}$ [35] MoS_2 is highly interesting. People are looking in to the possibility of using it in a wide number of applications, including: solar cells [36], peizo-electrics [37], supercapacitors [38], flexible electronics [39], biosensors [40] and others. Many of which utilizes the MoS_2 in a field effect transistor structure. Thus far, most data and theory concerning MoS_2 have been based on exfoliated material [32]. However, a lot of work have been put in to developing synthesis processes, such as Chemical Vapor Deposition (CVD) [41, 42]. CVD grown materials is of particular interest to the industry because of its scalability, making it easier and less labor intensive to produce more material and as a consequence the devices using the material [41].

1.2.1 Electrical characterization of MoS_2

Traditionally if you wanted to characterize an MoS_2 flake, it was necessary to either build a finished device and characterize that, or make a simpler test structure that still needed a lithographic step [43]. As the production of TMD moves from the lab to the fab (fabrication plant) non-destructive methods of characterization becomes increasingly desirable. On such method is the use of THz Time Domain Spectroscopy to measure on the sample. This method is still a while of from working fully on these materials due to the high resistances. An alternative would be to use M4PP to perform a field effect measurement on MoS_2. Something similar with four-point probes have already been done to characterize as-grown Silicon-on-Isolator (SOI) wafers by the semiconductor industry [44, 45]. This method is known as the Pseudo-Metal-Oxide-Semiconductor Field-Effect Transistor (Ψ-MOSFET) characterization method [44]. The method uses macroscopic probes, either in a two probe or a four point probe technique to perform a field effect measurement [46]. While measurements are performed on the device layer, a gate voltage is applied to the handle of the SOI. The Buried Oxide Layer (BOX) acts like the insulator between the gate and channel in a traditional Metal-Oxide-Semiconductor Field-Effect Transistors (MOSFET). The entire measurement setup is without the need for lithography [44].

A similar method to the Ψ-MOSFET method, is presented in this thesis for measuring on MoS_2, but instead of using macroscopic probes with a contact force around 0.5N [47], microscopic probes are used, that have a pressure around 50µN [24]. In other words the equivalent weight is four orders of magnitude lower. In comparison this is the same weight relation as comparing a can of soda (330mL) with two and a half average European cars (∼3500kg) [48].

1.3 Aim of the Thesis

This thesis has two overall goals that it attempts to achieve. As part of a larger European Union project (Three Dimensional Advanced Metrology - 3DAM) the main goal was to build a measurement setup, using M4PP, that is able to perform field effect measurements on 2D materials, such as MoS_2. By using M4PP instead of lithographically designed contacts, measurements can be made directly on the material. In theory this allows for either near or in-line characterization of the materials, without the loss of real-estate on the wafer for test structures.

The goal in this thesis was not to necessarily reach a point were using M4PP became the automatic go to for field effect measurements. But rather to make a proof of concept setup.

Showing that these types of measurements are possible, despite the long measurement times, and high contact resistances. Consequently the target is to reach a precision of around 10%.

The goal of the other part of the thesis was to characterize the mechanical behavior of micro-electrodes, so to better understand how they behave during vibrations. But also to develop a fundamental understanding of how changing different dimensions of the micro-electrode changes their behavior. As part of this, an analytic expression for the stiffness and compliance of the micro-electrodes needed to be derived. The unifying idea of the two parts, are in its essence a desire to make the best possible field effect measurements on MoS_2. For this we need to be able to make probes that have a small electrode pitch. But that can be relied on to stay in place, during measurements that can easily take more than half an hour to complete.

As the project progressed, a limitation in the number of usable MoS_2 samples from our collaboration partners, forced the focus of the thesis to shift from primarily focusing on the field effect measurements, to focus more on the design optimization of micro-electrodes.

1.4 Outline

This thesis is separated into two parts, a part that is about the mechanical behavior of M4PP, and a part that talks about the use of M4PP to do field effect measurements on MoS_2.

Chapter 2 Theory chapter, describing some of the basic theory used in the thesis.

The first part consists of three main chapters.

Chapter 3 This chapter consists of the derivations of the compliance tensor that is used to describe a cantilevers mechanical behavior.

Chapter 4 Here the concept of vibration tolerance is introduced. An expression for the vibration tolerance is derived and experimentally tested.

Chapter 5 The last chapter in this part of the thesis deals with the problem of optimizing a cantilever design. This chapter contains a general study of how each design parameter of the cantilever affects the performance of the hole. Finally the chapter presents two examples of optimization on a cantilever design.

The second part of the thesis, dealing with the measurements on MoS_2, consists of two chapters.

Chapter 6 This chapter deals with all the work that went into creating the setup used in the field effect measurements. Here the physical setup, the LabView code and the reference measurements are presented. The chapter also includes a short study of the possible damage a M4PP can do to a MoS_2 sample.

Chapter 7 After a description of the samples, this chapter delves into the actual field effect measurements done on MoS_2 samples.

The last chapter in the thesis (Chapter 8) presents an outlook and conclusion to the thesis.

2 | Theory: Micro Four-Point and Field Effect Measurements

2.1 Basics of Micro Four-Point Probing

In this thesis the main use of four-point measurements have been through the use of a M4PP, where all electrodes were evenly spaced and co-linear.

In a four-point measurement, four contacts to a material is made. Two of which is used as a source and drain for a current. This is either done by forcing a current I_{SD} or by applying a potential difference V_{SD} between the two contacts. While the current is running the potential drop between the two other contacts is measured. Since there is no current running through the sensing electrodes, the potential drop inside these electrodes is zero. Consequently the only potential drop that the sensing pins will measure is the potential drop inside the sample. This potential drop will moving forward be referred to as the four-point voltage. Combining the four-point voltage with the sourced current gives the four-point resistance. One or more four-point resistances can be used to calculate the sample/material parameter known as the sheet resistance.

Looking at a co-linear probe consisting of four electrodes there are 24 ways of choosing the positions of the sourcing and sensing electrodes. However, only six of these give rise to unique results. All other configurations gives either the same results as the six unique or the same result with opposite sign. This is only the case if the sample behaves ohmic, meaning that the resistance does not depend on the direction of the current. E.g. a diode would be an example of something not ohmic. The basic six unique configurations for a M4PP are shown in figure 2.1. These six configurations are connected through the relation $R_A + R_{A_P} = R_B + R_{B_P} + R_C + R_{C_P}$ [15] where in the absence of a magnetic field $R_A = R_{A_P}$, $R_B = R_{B_P}$ and $R_C = R_{C_P}$ [49]. These relations can be used to self validate the results from a four point measurement. This is called the reciprocity theorem

2.1.1 Sheet Resistance and Sheet Conductance

M4PP has been used to measure a wide variety of parameters, but for the purpose of this thesis the most important is the sheet resistance, R_S, or sheet conductance, G_S. One being the inverse of the other. The equations in this chapter will mainly refer to the sheet resistance, but all references to the sheet resistance could be replaced with the sheet conductance by using that $G_S = R_S^{-1}$. For ease of reading and brevity the derivations

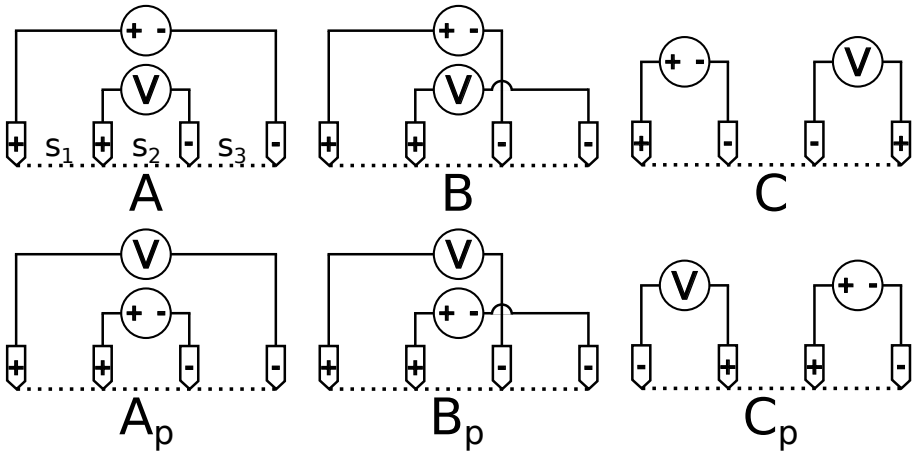

Figure 2.1: Sketch showing the six unique configurations possible with M4PP. Note that the prime configurations are simply a swap of the source-drain electrodes with the sensing electrodes. s_1, s_2 and s_3 are the distance between the first and second, second and third, and third and fourth electrode respectively.

shown here will only discuss sheet resistance.

The sheet resistance is derived from the resistivity, ρ. The resistivity of a material is given by [50].

$$1/\rho = ne\mu_e + pe\mu_h, \tag{2.1}$$

where n and p are the concentrations of electrons and holes in the material respectively, e is the elemental charge, and μ_e and μ_h are the mobility of electrons and holes in the material respectively. For semiconductors the charge concentrations (and therefore the resistivity) depends heavily on doping and the presence of any electric fields.

Where ρ (and consequently conductivity) is a material parameter, the sheet resistance is a device specific parameter. Meaning two objects of the same material can have widely different sheet resistances. In its most basic description the sheet resistance is the electrical resistance for passing a current from on side of a square to the other, through a material with uniform thickness, d [51].

$$R_S = \frac{\rho}{d} \tag{2.2}$$

This is also the reason why the unit for sheet resistance, while being measured in Ω, is often reported in Ω/□. In this thesis sheet resistance and sheet conductance will be given in Ω and S respectively.

Using M4PP the sheet resistance of a infinite sheet can in general be calculated by using a modification to the van der Pauw (vdP) equation [49].

$$\exp\left(-\frac{\pi R_A}{R_S}\right) + \exp\left(-\frac{\pi R_B}{R_S}\right) = 1 \tag{2.3}$$

where R_S is the sheet resistance. Note that this equation is only valid for collinear probes.

Alternatively the sheet resistance can also be calculated using constant corrections factors to the measured four-point resistances

$$R_i = \frac{R_S}{2\pi} \ln \frac{|\mathbf{r}_{V_-} - \mathbf{r}_{I_+}||\mathbf{r}_{V_+} - \mathbf{r}_{I_-}|}{|\mathbf{r}_{V_+} - \mathbf{r}_{I_+}||\mathbf{r}_{V_-} - \mathbf{r}_{I_-}|} \tag{2.4}$$

where $i \in \{A, B, C\}$, $\mathbf{r}_j$ is the position of the j'th electrode, so that $|\mathbf{r}_j - \mathbf{r}_k|$ is the distance between the j'th and k'th electrode [4, 25, 22]. As an example the four-point resistance for a B-configuration is given by:

$$R_B = \frac{R_S}{2\pi} \ln \frac{(s_1 + s_2 + s_3)s_2}{s_1 s_4} = \frac{R_S}{2\pi} \ln 3 \tag{2.5}$$

where s_i is the electrode pitch between i'th and $i+1$'th electrode. For a equidistant probe, the logarithmic term simplifies to $\ln 3$, as $s_i = s$ for all i. The electrode pitches are shown in Figure 2.1.

The method shown in (2.4) will not correct for any electrode position errors that might, and most likely will, occur during measurements. For this reason it is advised to use the vdP expression whenever possible (Equation (2.3)).

2.1.2 Position Errors

Position error is an umbrella term that contains all sources of errors that causes the four-point probe electrodes not to be in the intended position during measurement. Generally they can be sorted into three categories [21].

Probe geometry errors are errors that are a result of variations in the design of the probe used. E.g. these variations can be caused by uncertainty or a mistake in the fabrication process of the probe. Statistically this category contains all position errors that are constant and independent of the engage and can be considered a systematic error.

Static position errors are errors that are introduced during the engage. E.g. this could be caused by a rough surface that made each electrode slide in a different way. Statistically this category contains all position errors that are constant during a single engage, but varies from engage to engage and can be considered a systematic error within a single engage.

Dynamic position errors are errors from the electrodes moving on the surface during measurement. E.g. this could be due to vibrations in the system, making the electrodes oscillate on the sample. Statistically this category contains all position errors that varies within a single engage and can be considered a random error.

When dealing with these position errors it is assumed that the three categories of position errors are independent of each other. Meaning that the dynamic position error does not depend on the engage, and that the static position errors does not depend on the probe geometry. In reality any one source of position errors would probably affect all three categories. However each of these contributions will be dealt with as a separate error source.

Going forward in this description of position errors the formalism used in Kjær et al [21] will be used.

When talking about position errors we are not interested in the absolute positions of the electrodes but rather their relative position. That means that the position of the first electrode can be defined as being $(x, y) = (0, 0)$. With x being in-line and y being off-line position. Figure 2.2 shows a sketch of an in- and off-line error. This in turn means that the nominal position of all other electrodes are positioned at $\mathbf{r}_{n0} = (x_{x0}, 0)$. Where

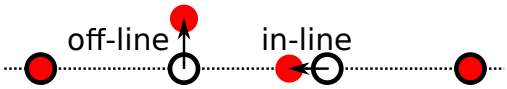

Figure 2.2: Sketch of an in- and off-line error. The black rings indicate the nominal position of the electrodes. The red dot indicates the actual position of the electrode.

$n, m \in \{1, 2, 3, 4\}$ indicates electrode 1 through 4 with $n \neq m$. Taking the three sources of error into account the actual position is given by,

$$\mathbf{r}_n = (x_{n0} + \Delta_{nx}, \Delta_{ny}) \tag{2.6}$$

where Δ_{nx} and Δ_{ny} are the total position errors in- and off-line respectively [21].

Now looking at the effect of an position error on one of the distance terms in equation (2.4),

$$\begin{aligned} |\mathbf{r}_n - \mathbf{r}_m| &= \sqrt{(x_{n0} + \Delta_{nx} - x_{m0} - \Delta_{mx})^2 + (\Delta_{ny} - \Delta - my)^2} \\ &= |x_{n0} - x_{m0}| \sqrt{\left(1 + \frac{\Delta_{nx} - \Delta_{mx}}{|x_{n0} - x_{m0}|}\right)^2 + \left(\frac{\Delta_{ny} - \Delta_{my}}{|x_{n0} - x_{m0}|}\right)^2}. \end{aligned} \tag{2.7}$$

By doing a taylor expansion and using the probe is equidistant, $|x_{n0} - x_{m0}| = s|n - m|$, this can be simplified to [21]

$$|\mathbf{r}_n - \mathbf{r}_m| \approx s|n - m| \left(1 + \frac{\Delta_{nx} - \Delta_{mx}}{s|n - m|} + \frac{1}{2}\left(\frac{\Delta_{ny} - \Delta_{my}}{s|n - m|}\right)^2\right). \tag{2.8}$$

From this it can be concluded that the off-line position errors are a second order term, where in-line errors are a first order term [21]. Meaning that for small positional errors, compared to the electrode pitch, off-line errors are negligible.

Assuming all position errors are normally distributed and in-line, their effect on a four-point measurement can be calculated as

$$\sigma_{R_i}^{\text{rel}} = \frac{1}{R_i} \sum_{n=1}^{4} \left(\frac{\partial R_i}{\partial x_n} \sigma_x\right)^2 \tag{2.9}$$

where $\sigma_{R_i}^{\text{rel}}$ is the relative standard deviation of the four-point resistance from the static position errors and σ_x is the standard deviation of the static position errors [23, 21]. For an equidistant probe this can be simplified to

$$\sigma_{R_A}^{\text{rel}} = \frac{\sqrt{5}}{\ln 4} \frac{\sigma_x}{s} \cong 1.61 \frac{\sigma_x}{s} \tag{2.10}$$

$$\sigma_{R_B}^{\text{rel}} = \frac{4\sqrt{5}}{3 \ln 3} \frac{\sigma_x}{s} \cong 2.71 \frac{\sigma_x}{s}. \tag{2.11}$$

Similarly for the dynamic position error

$$\sigma_{R_A}^{\text{rel,dyn}} = \frac{\sqrt{5}}{\ln 4} \frac{\sigma_x^{\text{dyn}}}{s} \tag{2.12}$$

$$\sigma_{R_B}^{\text{rel,dyn}} = \frac{4\sqrt{5}}{3 \ln 3} \frac{\sigma_x^{\text{dyn}}}{s}. \tag{2.13}$$

Where σ_x^{dyn} is the standard deviation of the dynamic position errors [21].

The static in-line position error can be compensated for by using the vdP expression in Equation (2.3). The dynamic position errors cannot be compensated for analytically, since it is a random error and are indistinguishable from the electric noise. The effect of the dynamic position errors on the position-corrected sheet resistance for an equidistant probe is, [21]

$$\sigma_{R_S}^{\text{rel}} \cong 5.61 \frac{\sigma_x^{\text{dyn}}}{s} \tag{2.14}$$

where $\sigma_{R_S}^{\text{rel}}$ is the relative standard deviation of the sheet resistance. This expression is based on a first-order calculation [21]. In case of non-equidistant probes the geometrical coefficients can be found in Kjær et al. [21] and will not be recreated here.

Chapter 4 and 5 will deal with designing cantilevers that passively suppress dynamic position errors in the form of vibrations.

2.2 Field Effect Measurements

One of the most interesting applications of semiconductor materials is the fabrication of Field Effect Transistor (FET). Transistors form the foundation of modern society, and without them there would be no computers. Therefore, it is very important to be able to characterize their behavior. The most common of these transistors is the FET. Simply put a FET is a piece of semiconductor with two electrical terminals; a source and a drain. Between the two terminals are placed a gate terminal. The gate consists of a conductive material separated from the semiconductor by an insulator. By applying a potential at the gate, charges can either be introduced or removed from the semiconductor near the gate. If enough potential is applied, the number of charges will reach a point where the semiconductor becomes conductive. In layman's terms a transistor acts like a switch.

The transistor structures considered in this thesis are a slight variation on a MOSFET, where the metal in the gate is replaced with highly conductive silicon on the backside of the structure. An equivalent setup is used when measuring on SOI ans is called a Ψ-MOSFET [44]. A sketch of a typical MOSFET is shown in figure 2.3 (left). The source is where charge carriers enter the structure and the drain is where they leave. In the case of electrons this means that the high potential is on the drain [51]. In the derivation made here it will be assumed that the source is at zero potential.

The following explanations and derivations are to a large degree, based on the book "Handbook of Silicon Semiconductor Metrology" by Diebold [51].

2.2.1 Threshold Voltage

One of the most important metrics when it comes to a MOSFET is the threshold voltage, V_T, which indicates the gate voltage, V_G, needed to change the transistor from the off-state to the on-state. The magnitude of V_T influences, to a large degree, the use of the transistor. When the transistor is in the on-state a current can pass from the drain to the source (or vice versa). This current is typically known as the drain current, I_D. V_T can be determined from the curve of I_D plotted against V_G. In this section two methods for extracting V_T from this curve will be presented. The two methods are valid in two

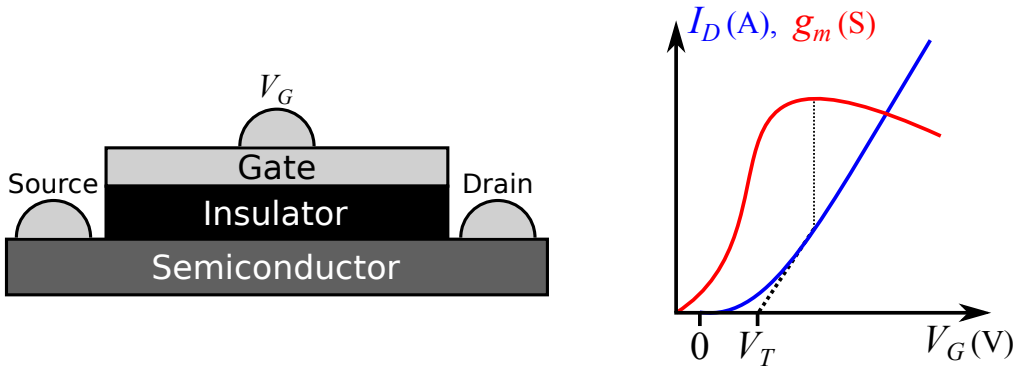

Figure 2.3: (Left) Sketch of a typical MOSFET. I_S and I_D are the source and drain currents respectively. V_G is the gate voltage. The semicircles indicates contacts. (Right) Sketch of how to find the linearly extrapolated threshold voltage, V_T. The sketch is not to scale, and should not be used for anything besides visualizing how to extract V_T.

different operation regimes of a MOSFET, namely the linear and saturation regime. The linear regime is achieved if the transistor is operated with a low source-drain voltage, V_D, i.e. $V_D < V_G - V_T$ [52]. In this regime the transistor functions roughly like a resistor. The saturation regime is when the transistor is operated with a high V_D, i.e. $V_D > V_G - V_T$ [52]. In this regime the potential drop between the source and drain is high enough to cause a pinch-off in a traditional MOSFET [52].

Linear Regime

The first method is by linear extrapolation of the I_D–V_G curve. The slope of the I_D–V_G curve is better known as the transconductance, g_m.

$$g_m = \frac{\partial I_D}{\partial V_G} \tag{2.15}$$

The extrapolation is performed from where g_m is largest, and goes to zero current. A sketch of the extrapolation is shown in Figure 2.3 (right). The threshold voltage is the gate voltage at which the extrapolation reaches zero [51].

This method is only valid if the transistor is operated in the linear regime. The drain current in this regime can be modeled as

$$I_D = \mu c C_{ox} \left(V_G - V_T - \tfrac{1}{2} V_D \right) V_D \tag{2.16}$$

where μ is the minority carrier mobility, C_{ox} is the capacitance of the transistor gate and c is the device specific geometric factor. For a standard MOSFET this would be the width divided by the length of the channel [51].

Saturation Regime

The other method of finding V_T is valid when the transistor is operated in the saturation regime. In this case V_T is found in much the same manner as for the linear, but the $\sqrt{I_{SD}}$–V_G curve is used instead. From this curve the threshold is found by linear extrapolation to zero. The drain current for a MOSFET in the saturation regime can be modeled

as [51]

$$I_D = \frac{\mu c C_{ox}}{2}(V_G - V_T)^2 \tag{2.17}$$

2.2.2 Field Effect Mobility

The field effect mobility, μ_{FE}, is the measure for μ gained from a field effect measurement. Strictly μ_{FE} is given by

$$\mu_{\mathrm{FE}} = \mu \frac{n_s}{n_{\mathrm{ind}}} \tag{2.18}$$

where n_s is the concentration of free conduction band electrons, and n_{ind} is the induced charge concentration [52]. For traditional MOSFET $n_s = n_{\mathrm{ind}}$ meaning that $\mu_{\mathrm{FE}} = \mu$ [52]. Just as with V_T, how to determine μ_{FE} depends on which regime the transistor is operated in.

Linear Regime

Using Equation (2.16) the transconductance is calculated.

$$g_m = \frac{\partial I_D}{\partial V_G} = \mu c C_{ox} V_D \tag{2.19}$$

Using that μ_{FE} and μ is the same, μ_{FE} is simply isolated from the expression for g_m [51].

$$\mu_{\mathrm{FE}} = \frac{g_m}{C_{ox} V_D} \frac{1}{c} \tag{2.20}$$

Saturation regime

Instead of isolating μ_{FE} from g_m, it is here isolated from the slope of the $\sqrt{I_D}$–V_G curve instead. For this we introduce a new variable g_s.

$$g_s = \frac{\partial \sqrt{I_D}}{\partial V_G} = \sqrt{\frac{1}{2}\mu c C_{ox}} \tag{2.21}$$

μ_{FE} is then simply isolated from the expression for g_s [51].

$$\mu_{\mathrm{FE}} = \frac{g_s^2}{C_{ox}} \frac{2}{c} \tag{2.22}$$

Four-Point Measurements

Using a four-point measurement technique, μ_{FE} can be determined from Equation (2.20), substituting $I_D/(cV_D)$ with the sheet conductance, G_S [41].

$$\mu_{\mathrm{FE}} = \frac{\partial G_S}{\partial V_G} \frac{1}{C_{ox}} \tag{2.23}$$

Since this is based on the expression for the linear regime it is naturally only valid in that regime.

Following the same logic the saturation regime should be given by

$$\mu_{\mathrm{FE}} = \frac{\partial G_S}{\partial V_G} \frac{2V_D}{C_{ox}}. \tag{2.24}$$

Part I

Mechanical Behavior and Design of Micro Electrodes

3 | Cantilever Compliance and Stiffness

In most cases when working with cantilevers in micro four-point probes but also in other applications, a parameter of great interest is the cantilevers spring constant, or to be more clear its stiffness tensor $\mathbf{K}$. The stiffness tensor is usually a three by three matrix that describes which forces $\mathbf{F}$ arises when the cantilever is deflected $\boldsymbol{\delta}$ in some direction in space [53].

$$\mathbf{F} = \mathbf{K}\boldsymbol{\delta}$$
$$\begin{bmatrix} F_x \\ F_y \\ F_z \end{bmatrix} = \begin{bmatrix} K_{xx} & K_{xy} & K_{xz} \\ K_{yx} & K_{yy} & K_{yz} \\ K_{zx} & K_{zy} & K_{zz} \end{bmatrix} \begin{bmatrix} \delta_x \\ \delta_y \\ \delta_z \end{bmatrix} \tag{3.1}$$

However often it is hard to calculate the stiffness tensor analytically. Instead the inverse of the stiffness tensor, the compliance tensor $\mathbf{C}$, is calculated. The compliance tensor can be written as the sum of individual compliance contributions [53].

$$\mathbf{C} = \mathbf{K}^{-1} \tag{3.2}$$

The compliance describes the deflection that results from an applied force. It is much easier to apply a force mathematically than it is to apply a deflection. This is due to the other important parameters, such as bending moment and shear force, are directly linked to the force but not the deflection.

3.1 Evaluation of Compliance Elements

The deflection of a beam in relation to an applied load is described by the Euler-Bernoulli equation [53].

$$\frac{\mathrm{d}^2}{\mathrm{d}x^2}\left(EI\frac{\mathrm{d}^2\delta(x)}{\mathrm{d}x^2}\right) = q(x) \tag{3.3}$$

Corresponding to a bending in either the y or z-direction at some position x. Here E is the Young's modulus for the beam, often a constant along the x-direction. I is the area moment of inertia for the beam, and depends on the shape of the beam. $\delta(x)$ is the

deflection orthogonal to the x-axis at x. $q(x)$ is the applied load on the beam. For the Euler-Bernoulli equation to be applicable the beam must be modeled as a one-dimensional object, additionally it is assumed that only small deflections are applied. As long as the length of the beam is considerably larger than its other dimensions, the one-dimensional model is a good choice.

In the case of calculating the deflection of cantilevers affected by a point force, it makes more sense to use the second order linear differential equation, that relates the deflection with the bending moment [53].

$$\frac{\mathrm{d}^2\delta(x)}{\mathrm{d}x^2} = -\frac{M(x)}{EI} \tag{3.4}$$

where $M(x)$ is the bending moment. This equation can be derived from equation (3.3), but is also a fundamental equation of beam bending.

Additionally forces applied along the direction of the beam will result in an elongation of the beam. The elongation is given by [53]

$$\delta_{elong} = \frac{F}{EA}L \tag{3.5}$$

where A is the cross sectional area of the beam and L is the length of the beam. All further equations and investigations are based on eq. (3.4) and (3.5).

To find the total deflection of the cantilever the bending moment, Young's Modulus and area moment of inertia needs to be determined. Young's modulus is a material constant that can easily be found for most materials either online or in engineering textbooks. For now it is left as E in the equations.

The area moment of inertia depends on the cross-sectional design of the beam. Here the focus will be on simple beams with a rectangular cross-section. Besides resulting in simple expressions for the area moment of inertia, it is also the nominal design of most cantilevers used in micro four-point probes. The area moment of inertia, for a rectangular beam rotated around an axis orthogonal to the beam direction is given by [54]:

$$I_j = \int k^2 \mathrm{d}a = \frac{w_j w_k^3}{12}. \tag{3.6}$$

where (i, j, k) is an orthogonal base, with the beam pointing along i and rotates around j. a is the cross sectional area of the beam in the jk-plane. w_j and w_k are the dimensions of the beam in the j and k directions respectively. E.g. the beam shown in Figure 3.1, rotated around the y-axis, has an area moment of inertia of $I_y = WH^3/12$.

In general the bending moment is given as the cross product of the location vector and the force vector; $\mathbf{M} = \mathbf{r} \times \mathbf{F}$. However in the case of micro-electrodes this can be simplified considerably. First of it is assumed that all beams are one dimensional, meaning the bending moment collapses to a scalar. Additionally the considered cantilevers are always fixed (clamped) in one end, and a force is a applied in a single point at the other end. These corresponds to where the cantilever is connected to the probe-body, and where the cantilever touches the sample, respectively. A beam that is fixed in one end and is affected by a point force at the other end is subject to a constant shear force along the beam. This in turn means that the bending moment can be expressed as:

$$M(\ell) = F(L - \ell). \tag{3.7}$$

where F is the point force, L is the length of the beam and ℓ is a point along the length of the beam.

Returning to the differential equation (3.4). A beam with one end fixed and one free, will always lead to a pair of Dirichlet and Neumann boundary conditions [55].

$$\textit{Dirichlet:} \qquad \delta(x_0) = t_1 \tag{3.8}$$

$$\textit{Neumann:} \qquad \frac{\mathrm{d}}{\mathrm{d}x}\delta(x_0) = t_2 \tag{3.9}$$

where t_1 and t_2 are constants, and x_0 is specific value of x.

Every new beam added to the cantilever results in an extra differential equation that needs to be solved. These new beams are in turn fixed at the end of the previous beam, meaning their boundary conditions will also be a pair of Dirichlet and Neumann boundary conditions [53, 55]. While the first beam will have the homogeneous Dirichlet and Neumann boundary conditions (i.e. $t_1 = t_2 = 0$), any subsequent beam will have inhomogeneous boundary conditions that depends on the previous beam. A linear ordinary differential equation with a mixture of Dirichlet and Neumann boundary conditions can always be solved by integration.

The compliance elements C''_{ij} can be found as the deflection in the i-direction from a force in the j-direction divided by the magnitude of said force ($\delta_i = C_{ij}F_j$). Where i and j are x, y or z. The double prime notation (i.e. C'') indicates that the compliance element is written in the cantilever coordinate system. This becomes relevant in the next chapter when the compliance tensor in the sample coordinates is needed. Following this method the full compliance tensor can be calculated by applying a force in each of the three directions one by one and calculating the resulting deflections.

In the remainder of this chapter the compliance tensor for the straight cantilever and Two-Beam (2B) cantilevers will be derived. 2B cantilevers consists of two beams connected at the ends with an arbitrary angle in the xy-plane. A sketch of such a cantilever is shown in Figure 3.2.

3.2 Straight Cantilever

The simplest cantilever design that was originally used in M4PP is the straight cantilever. This is simply a rectangular beam of length L that is connected orthogonally to the probe-body. A sketch of a straight cantilever is shown in Figure 3.1. When used the cantilever tip will be engaged on a surface, resulting in a force being applied on the tip of the cantilever. By using eq.(3.6) the area moments of inertia for rotating around the y- and z-axis are found to be:

$$I_y = \frac{WH^3}{12}, \qquad I_z = \frac{W^3H}{12}$$

Force in x-direction

Applying a force at the tip of the cantilever in x-direction, i.e. along the cantilever, will not result in any bending of the cantilever [6]. It will however result in an elongation.

$$\delta_{xx}(L) = \frac{L}{EWH} F_x \tag{3.10}$$

Force in y- and z-direction

A force in the y- or z-direction will cause a bending in that respective direction. Equation (3.4) with the area moments of inertia for this cantilever gives this equation:

$$\frac{\mathrm{d}^2}{\mathrm{d}x^2}\delta_{ii}(x) = -\frac{F_i(L-x)}{EI_j}\sin\eta \qquad \left| \begin{array}{rr} \text{BC:} & \delta(0) = 0 \\ & \frac{\mathrm{d}}{\mathrm{d}x}\delta(0) = 0 \end{array} \right.$$

where $(i,j) = (y,z)$ or $(i,j) = (z,y)$.

Solving this using homogeneous boundary conditions gives the deflections:

$$\delta_{yy}(L) = \frac{L^3}{3EI_z} F_y = \frac{4L^3}{EW^3H} F_y \tag{3.11}$$

$$\delta_{zz}(L) = \frac{L^3}{3EI_y} F_z = \frac{4L^3}{EWH^3} F_z \tag{3.12}$$

A bending of a cantilever in either the y- or z-direction will naturally make the tip of the cantilever move slightly in the x-direction. However due to the small angle assumption made earlier, this is negligible. Elongation is also ignored in y- and z-directions, since they are negligible compared to the bending.

The compliance tensor for a straight cantilever is then found to be [54]:

$$\mathbf{C}'' = \begin{bmatrix} \frac{L}{EWH} & 0 & 0 \\ 0 & \frac{4L^3}{EW^3H} & 0 \\ 0 & 0 & \frac{4L^3}{EWH^3} \end{bmatrix} \tag{3.13}$$

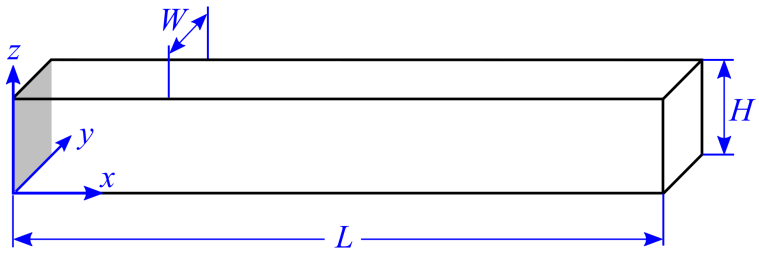

Figure 3.1: Sketch of a straight cantilever. Relevant parameters are shown on the figure. The grayed out area is the surface on which the cantilever is connected to a probe body. For calculation purposes the cantilever is considered clamped on this surface.

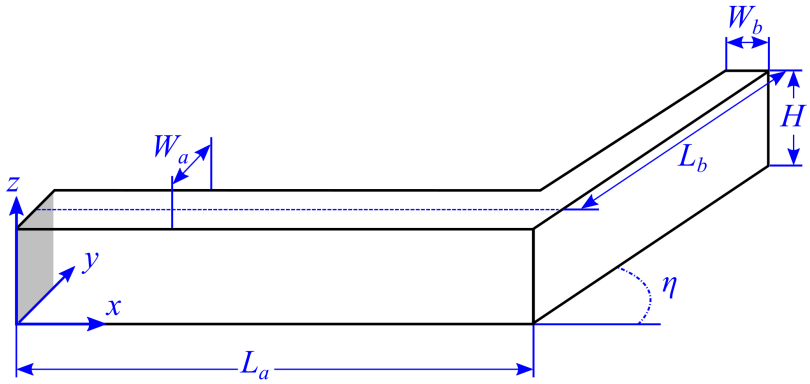

Figure 3.2: Sketch of a cantilever with an bend of arbitrary angle. Relevant parameters are shown on the figure. The grayed out area is the surface on which the cantilever is connected to a probe body. For calculation purposes the cantilever is considered clamped on this surface.

3.3 Cantilever with Bent of Arbitrary Angle

Instead of having a straight cantilever, a bend can be introduced to allow for greater control of the cantilevers mechanical behavior when engaged. These types of cantilevers are here collectively referred to as 2B cantilevers. A sketch of such a cantilever is shown in Figure 3.2. These cantilevers can be modeled as two beams, where the second beam connects to the first beam at an angle η. Here the two beams have been named a and b for the first and second beam respectively. Moving forward the joint between the two beams will be referred to as the "elbow" of the cantilever. Likewise, the point where the cantilever is clamped to the probe-body will be referred to as the "shoulder".

The derivations for the special case where $\eta = 90°$ is shown in the paper “Three-Way Flexible Cantilever Probes for Static Contact” by Fei Wang et al. [24]. The expression for which will be shown in the next section.

When calculating the compliance tensor elements for 2B cantilevers the procedure is much the same as for the straight probe. However, due to the bend at the elbow, a force in x- and y-direction will also cause a deflection y- and x-direction respectively. Additionally a force in the z-direction will not only cause the cantilever to bend, but also to twist.

There are four relevant area moments of inertia for these cantilevers; the moment around the z-axis of both beams, the moment around the y-axis for beam a, and the moment around the transverse axis for beam b. This vector will be referred to as m and the direction along beam b will be referred to as ℓ. Both are shown in Figure 3.3.

$$\begin{aligned} I_{z,a} &= \frac{W_a^3 H}{12}, \qquad I_{z,b} = \frac{W_b^3 H}{12} \\ I_{y,a} &= \frac{W_a H^3}{12}, \qquad I_{m,b} = \frac{W_b H^3}{12} \end{aligned} \tag{3.14}$$

The boundary conditions for beam a are the homogeneous boundary conditions also used for the straight cantilever. The boundary conditions for beam b will depend on the deflection of beam a.

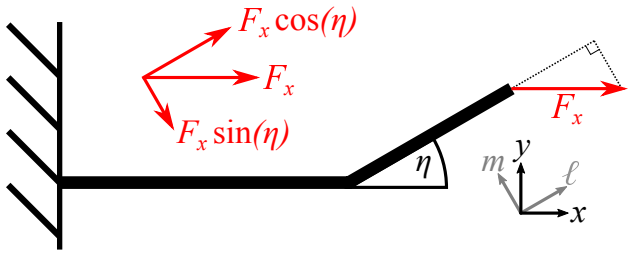

Figure 3.3: Sketch of the force diagram for a force in the x-direction on a cantilever with arbitrary bent.

3.3.1 Force in the x-direction

First the deflection of beam a is calculated. Figure 3.3 depicts a sketch how the force can can be split into a part that is orthogonal to beam b and a part that is parallel. A new coordinate system has also been introduced, ℓ and m which are parallel and orthogonal to beam b respectively and has its origin in the elbow. The part that is parallel to beam b will only cause an elongation. The orthogonal part gives rise to a constant shear force in beam b and by extension a linearly increasing bending moment going from the tip of the cantilever to the elbow. Since the cantilever is in a steady state. Segment a most have a constant bending moment that has the same magnitude as the bending moment in b at the elbow, but with an opposite sign.

$$\begin{aligned} M_a &= L_b F_x \sin\eta \\ M_b(\ell) &= -(L_b - \ell) F_x \sin\eta \end{aligned} \tag{3.15}$$

where ℓ indicates a position on beam b. The differential equation (3.4) for beam a becomes;

$$\frac{\mathrm{d}^2}{\mathrm{d}x^2}\delta(x) = -\frac{L_b F_x}{E I_{za}} \sin\eta \qquad \left| \begin{array}{rl} \text{BC:} & \delta(0) = 0 \\ & \frac{\mathrm{d}}{\mathrm{d}x}\delta(0) = 0 \end{array} \right.$$

Solving this gives the deflection of beam a at the elbow in the y-direction.

$$\delta_{yx,a} = -\frac{6 L_a^2 L_b}{E W_a^3 H} F_x \sin\eta \tag{3.16}$$

Naturally this deflection also leads to a change in the angle of the second beam. Under the small angle assumption the angle of the deflection is equal to the slope Θ_x of the beam.

$$\Theta_x = \frac{\partial \delta_{yx,a}}{\partial L_a} = -\frac{12 L_a L_b}{E W_a^3 H} F_x \sin\eta \tag{3.17}$$

Now the differential equation is solved for beam b, in the (ℓ, m)-coordinate system. Due to the deflection of beam a and the subsequent angle, the Neumann boundary condition for beam b is changed to match this angle shift. The differential equation becomes

$$\frac{\mathrm{d}^2}{\mathrm{d}\ell^2}\delta(\ell) = \frac{(L_b - \ell)}{E I_{zb}} F_x \sin\eta \qquad \left| \begin{array}{rl} \text{BC:} & \delta(0) = 0 \\ & \frac{\mathrm{d}}{\mathrm{d}\ell}\delta(0) = \Theta_x \end{array} \right.$$

Solving this gives a deflection in the m-direction ($\delta_{\ell x}$) that then needs to be translated back into deflections in the x- and y-directions. The total deflection in m at the tip of the

cantilever becomes:

$$\delta_{mx} = -\frac{4}{EH}\left(\frac{L_b^3}{W_b^3} + 3\frac{L_a L_b^2}{W_a^3}\right) F_x \sin\eta. \tag{3.18}$$

When translated back to x, y-coordinates the deflections becomes:

$$\delta_{xx,b} = -\delta_{mx}\sin\eta = \frac{4}{EH}\left(\frac{L_b^3}{W_b^3} + 3\frac{L_a L_b^2}{W_a^3}\right) F_x \sin^2\eta \tag{3.19}$$

$$\delta_{yx,b} = \delta_{mx}\cos\eta = -\frac{4}{EH}\left(\frac{L_b^3}{W_b^3} + 3\frac{L_a L_b^2}{W_a^3}\right) F_x \sin\eta\cos\eta \tag{3.20}$$

That last thing that is needed in the equation is the terms that comes from the elongation of the cantilever. These are quite easy to calculate following the method demonstrated in the derivations on the straight cantilever (sec. 3.2), while remembering that beam b is elongated along ℓ.

$$\delta_{xx,e} = \left(\frac{L_a}{EW_a H} + \frac{L_b}{EW_b H}\cos^2\eta\right) F_x \tag{3.21}$$

$$\delta_{yx,e} = \frac{L_b}{EW_b H} F_x \cos\eta\sin\eta \tag{3.22}$$

Combining all of these terms the compliance tensor element C_{xx} becomes:

$$\begin{aligned} C''_{xx} &= \frac{\delta_{xx,b} + \delta_{xx,e}}{F_x} \\ &= \frac{1}{EH}\left(\left[\frac{4L_b^3}{W_b^3} + \frac{12L_a L_b^2}{W_a^3}\right]\sin^2\eta + \frac{L_a}{W_a} + \frac{L_b}{W_b}\cos^2\eta\right) \end{aligned} \tag{3.23}$$

The compliance tensor element C''_{yx} becomes:

$$\begin{aligned} C''_{yx} &= \frac{\delta_{yx,a} + \delta_{yx,b} + \delta_{yx,e}}{F_x} \\ &= -\frac{1}{EH}\left(\frac{6L_a^2 L_b}{W_a^3} + \left[\frac{4L_b^3}{W_b^3} + \frac{12L_a L_b^2}{W_a^3} - \frac{L_b}{W_b}\right]\cos\eta\right)\sin\eta \end{aligned} \tag{3.24}$$

These expressions are still quite unwieldy. So three dimensionless constants are introduced: $\lambda = L_a/L_b$, $\alpha = H/W_a$, $\beta = H/W_b$. Written with these dimensionless constants the tensor elements becomes

$$C''_{xx} = \frac{4L_a^3}{EH^4}\left(\frac{\beta^3}{\lambda^3} + 3\frac{\alpha^3}{\lambda^3}\right)\sin^2\eta + \frac{L_a}{EH^2}\left(\alpha + \frac{\beta}{\lambda}\cos^2\eta\right) \tag{3.25}$$

$$C''_{yx} = -\frac{4L_a^3}{EH^4}\left(\frac{3}{2}\frac{\alpha^3}{\lambda} + \left[\frac{\beta^3}{\lambda^3} + 3\frac{\alpha^3}{\lambda^2}\right]\cos\eta\right)\sin\eta + \frac{L_a}{EH^2}\frac{\beta}{\lambda}\cos\eta\sin\eta \tag{3.26}$$

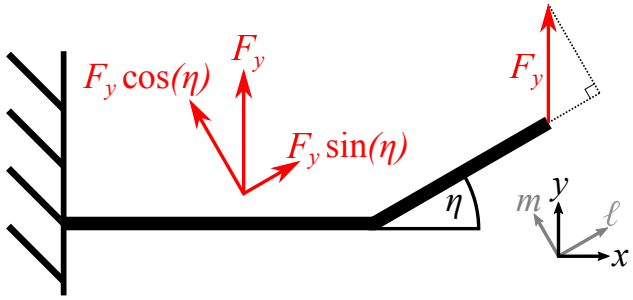

Figure 3.4: Sketch of the force diagram for a force in the y-direction on a cantilever with arbitrary bent.

Test of Solution

As a test the angles $\eta = 90°$ and $\eta = 0°$ is inserted, and compared to the solutions for the straight cantilever (sec. 3.2) and that of the L-shaped cantilever found in [24].

When inserting $\eta = 0°$, and using that $W = W_a = W_b$ and that $L = L_a + L_b$, the compliance element becomes;

$$C''_{xx}(\eta = 0°) = \frac{L}{EWH}$$
$$C''_{yx}(\eta = 0°) = 0$$

When looking at the compliance matrix for the straight cantilever, Equation (3.13), this is as expected.

Now inserting $\eta = 90°$, the compliance elements becomes;

$$C''_{xx}(\eta = 90°) = \frac{L_a^3}{EH^4}\left(4\frac{\beta^3}{\lambda^3} + 12\frac{\alpha^3}{\lambda^2}\right) + \frac{L_a}{EH^2}\alpha$$
$$C''_{yx}(\eta = 90°) = -6\frac{L_a^3}{EH^4}\frac{\alpha^3}{\lambda}$$

Besides the addition of an elongation term, which were ignored in [24], this matches with what was expected for L-shaped cantilever. The compliance tensor for the L-shaped cantilever is shown in eq. (3.44).

3.3.2 Force in the y-direction

The procedure to find the deflections when the cantilever is acted upon by a force in the y-direction is much the same as for the force in the x-direction. A force diagram is shown in Figure 3.4. First the deflection is calculated for beam a. The bending moments for the two beams can be found to be:

$$M_a(x) = -\left(L_a + L_b \cos\eta - x\right) F_y$$
$$M_b(\ell) = -\left(L_b - \ell\right) F_y \cos\eta \tag{3.27}$$

The Euler-Bernoulli equation for beam a becomes:

$$\frac{\mathrm{d}^2}{\mathrm{d}x^2}\delta(x) = \frac{L_a + L_b\cos\eta - x}{EI_{za}}F_y \qquad \left|\begin{array}{rl} \text{BC:} & \delta(0) = 0 \\ & \frac{\mathrm{d}}{\mathrm{d}x}\delta(0) = 0 \end{array}\right.$$

The deflection and slope Θ_y of beam a at the elbow are found by, following the same steps as the derivation for the force in the x-direction.

$$\begin{aligned} \delta_{yy,a} &= \frac{2}{EW_a^3H}\left(2L_a^3 + 3L_a^2L_b\cos\eta\right)F_y \\ \Theta_y &= \frac{6}{EW_a^3H}\left(L_a^2 + 2L_aL_b\cos\eta\right)F_y \end{aligned} \tag{3.28}$$

The deflection is then calculated for beam b.

$$\frac{\mathrm{d}^2}{\mathrm{d}\ell^2}\delta(\ell) = \frac{L_b - \ell}{EI_{zb}}F_y\cos\eta \qquad \left|\begin{array}{rl} \text{BC:} & \delta(0) = 0 \\ & \frac{\mathrm{d}}{\mathrm{d}\ell}\delta(0) = \Theta_y \end{array}\right.$$

Which solves to

$$\delta_{\ell y} = \frac{4}{EH}\left(\frac{3}{2}\frac{L_a^2L_b}{W_a^3} + 3\frac{L_aL_b^2}{W_a^3}\cos\eta + \frac{L_b^3}{W_b^3}\cos\eta\right)F_y \tag{3.29}$$

Like for the force in the x-direction the solution is translated from the (ℓ, m)-coordinate system back to the (x, y)-coordinate system.

$$\begin{aligned} \delta_{xy,b} &= -\delta_{\ell y}\sin\eta \\ &= -\frac{4}{EH}\left(\frac{3}{2}\frac{L_a^2L_b}{W_a^3} + \left[3\frac{L_aL_b^2}{W_a^3} + \frac{L_b^3}{W_b^3}\right]\cos\eta\right)F_y\sin\eta \end{aligned} \tag{3.30}$$

$$\begin{aligned} \delta_{yy,b} &= \delta_{\ell y}\cos\eta \\ &= \frac{4}{EH}\left(\frac{3}{2}\frac{L_a^2L_b}{W_a^3}\cos\eta + \left[3\frac{L_aL_b^2}{W_a^3} + \frac{L_b^3}{W_b^3}\right]\cos^2\eta\right)F_y \end{aligned} \tag{3.31}$$

And the elongation terms are calculated:

$$\delta_{xy,E} = \frac{L_b}{EW_bH}F_y\cos\eta\sin\eta \tag{3.32}$$

$$\delta_{yy,E} = \frac{L_b}{EW_bH}F_y\sin^2\eta \tag{3.33}$$

Using the (α, β, λ)-notation from before the compliance elements becomes:

$$C''_{xy} = -\frac{4L_a^3}{EH^4}\left(\frac{3}{2}\frac{\alpha^3}{\lambda} + \left[3\frac{\alpha^3}{\lambda^2} + \frac{\beta^3}{\lambda^3}\right]\cos\eta\right)\sin\eta + \frac{L_a}{EH^2}\frac{\beta}{\lambda}\cos\eta\sin\eta \tag{3.34}$$

$$C''_{yy} = \frac{4L_a^3}{EH^4}\left(\alpha^3 + 3\frac{\alpha^3}{\lambda}\cos\eta + \left[3\frac{\alpha^3}{\lambda^2} + \frac{\beta^3}{\lambda^3}\right]\cos^2\eta\right) + \frac{L_a}{EH^2}\frac{\beta}{\lambda}\sin^2\eta \tag{3.35}$$

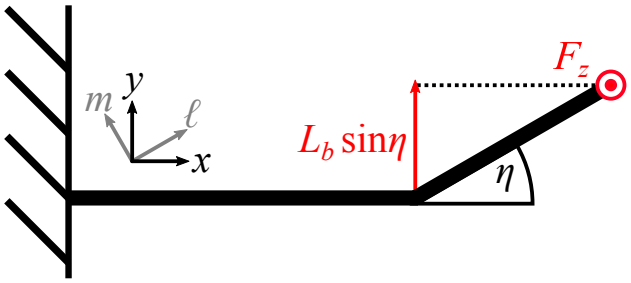

Figure 3.5: Sketch of the force diagram for a force in the z-direction on a cantilever with arbitrary bent.

Test of Solution

For an isotropic material it is known that off diagonal elements must match, so that C''_{xy} from equation (3.34) and C''_{yx} from equation (3.26) has to be identical, which is also the case. Secondly the new solution can be tested against known solutions for the straight (sec 3.2) and L-shaped probe [24] for C''_{yy}, corresponding to $\eta = 0$ and $\eta = 90°$ respectively. Using that for the straight cantilever $L_a + L_b = L$ and $W_a = W_b$.

$$C''_{yy}(\eta = 0°) = \frac{4L^3}{EW^3H}$$

$$C''_{yy}(\eta = 90°) = \frac{4L_a^3}{EH^4}\alpha^3 + \frac{L_a}{EH^2}\frac{\beta}{\lambda}$$

For zero degrees this is exactly the same result as for the straight cantilever. For 90 degrees this is the same result as in [24] (also reproduced in (3.44)) but with addition of a elongation term $L_a\beta/(\lambda EH)$

3.3.3 Force in the z-direction

The response to a force in the z-direction consists of a pure bending part and a torsion part. A force diagram is shown in Figure 3.5. Focusing on the bending part to begin with. The derivations are reminiscent of the derivations done for forces in x and y. The bending moments in the two beams becomes

$$\begin{aligned} M_a(x) &= -\left(L_a + L_b\cos\eta - x\right)F_z \\ M_b(\ell) &= -\left(L_b - \ell\right)F_z \end{aligned} \tag{3.36}$$

Looking at the differential equation for beam a, it becomes clear that the only difference between this equation and the one for a force in the y-direction is the force subscript and area moment of inertia

$$\frac{\mathrm{d}^2}{\mathrm{d}x^2}\delta(x) = \frac{L_a + L_b\cos\eta - x}{EI_{ya}}F_z \quad \Big| \quad \begin{aligned} \text{BC:} \quad \delta(0) &= 0 \\ \tfrac{\mathrm{d}}{\mathrm{d}x}\delta(0) &= 0 \end{aligned}$$

The deflection and slope Θ_z of beam a at the elbow is:

$$\begin{aligned} \delta_{zz,a} &= \frac{2}{EH^3}\left(2\frac{L_a^3}{W_a} + 3\frac{L_a^2L_b}{W_a}\cos\eta\right)F_z \\ \Theta_z &= \frac{6}{EW_aH^3}\left(L_a^2 + 2L_aL_b\cos\eta\right)F_z \end{aligned} \tag{3.37}$$

The differential equation for the second beam is given by:

$$\frac{\mathrm{d}^2}{\mathrm{d}\ell^2}\delta(\ell) = \frac{L_b - \ell}{EI_{ma}}F_z \qquad \left| \begin{array}{rl} \text{BC:} & \delta(0) = 0 \\ & \frac{\mathrm{d}}{\mathrm{d}x}\delta(0) = \Theta_z \cos\eta \end{array} \right.$$

Note the extra $\cos\eta$ on the Neumann boundary condition.

This solves to:

$$\delta_{zz,b} = \frac{2}{EH^3}\left(2\frac{L_b^3}{W_b} + 6\frac{L_a L_b^2}{W_a}\cos^2\eta + 3\frac{L_a^2 L_b}{W_a}\cos\eta\right)F_z \tag{3.38}$$

There are no elongation terms worth taking into account, since the force is acting orthogonally on all beams. However, there is a torsion term from the second beam twisting the first beam. The torsion deflection is given by the torsion angle φ_τ multiplied by the orthogonal distance from the force point of attack to the elbow.

$$\delta_{z,\tau} = \varphi_\tau L_b \sin\eta \tag{3.39}$$

In turn the torsion angle is given by the torque ($F_z L_b \sin\eta$) multiplied by the length of the twisted beam (L_a), divided by the shear modulus ($G = \frac{1}{2}\frac{E}{1+\nu}$, where ν is Poisson's Ratio) and the so called torsion constant J.

$$\varphi_\tau = \frac{F_z L_a L_b}{GJ}\sin\eta \tag{3.40}$$

Finding the torsion constant for a rectangular beam is by no means a trivial matter. Luckily Timoshenko have derived it in his book "Theory of Elasticity" [56].

$$J = W_a^3 H\left(\frac{1}{3} - \frac{64W_a}{\pi^5 H}\sum_{n\in\mathbb{O}}\frac{1}{n^5}\tanh\frac{n\pi H}{2W_a}\right) = W_a^3 H k_\alpha \tag{3.41}$$

where $\mathbb{O}$ is the set of all odd natural numbers. k_α is a constant, introduced to carry the cumbersome sum. The torsion deflection is then:

$$\delta_{z,\tau} = \frac{2}{EH}\frac{L_a L_b^2}{W_a^3}\frac{1+\nu}{k_\alpha}F_z \sin^2\eta \tag{3.42}$$

Combining all of this gives the following compliance tensor element in (α, β, λ) notation:

$$C''_{zz} = \frac{4L_a^3}{EH^4}\left(\alpha + 3\frac{\alpha}{\lambda}\cos\eta + 3\frac{\alpha}{\lambda^2}\cos^2\eta + \frac{\beta}{\lambda^3} + \frac{\alpha^3}{\lambda^2}\frac{1+\nu}{2k_\alpha}\sin^2\eta\right) \tag{3.43}$$

Test of Solution

Just like for the force in the x- and y-direction the solution is tested against the two known cases, $\eta = 0°$ and $\eta = 90°$.

$$C''_{zz}(\eta = 0°) = \frac{4L^3}{EWH^3}$$

$$C''_{zz}(\eta = 90°) = 4\alpha^3 + \frac{4\beta}{\lambda^3} + \frac{\alpha^3}{\lambda^2}\frac{2(1+\nu)}{k_\alpha}$$

Both of these results matches perfectly the results found for the straight cantilever (3.2) and the L-shaped cantilever ([24] equation (3.44)).

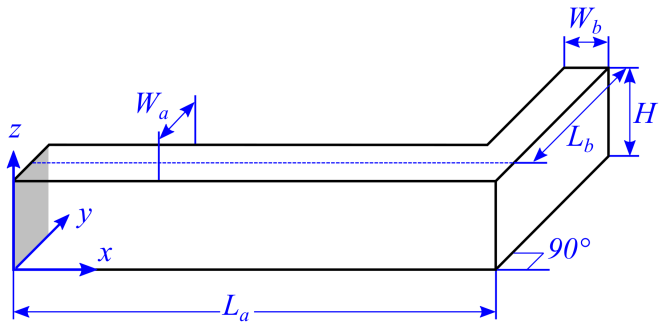

Figure 3.6: Sketch of an L-shaped cantilever. Relevant parameters are shown on the figure. The grayed out area is the surface on which the cantilever is connected to a probe body. For calculation purposes the cantilever is considered clamped on this surface.

3.4 L-Shaped Beam

For ease of reference, the solution for L-shaped beam shown in [24], is shown here, in the notation used in this thesis, without any derivations. The compliance tensor is

$$\mathbf{C}'' = \frac{L_a^3}{EH^4}\begin{bmatrix} \frac{12\alpha^3}{\lambda^2}+\frac{4\beta^3}{\lambda^3} & -\frac{6\alpha^3}{\lambda} & 0 \\ -\frac{6\alpha^3}{\lambda} & 4\alpha^3 & 0 \\ 0 & 0 & 4\alpha^3+\frac{4\beta}{\lambda^3}+\frac{2(1+\nu)\alpha^3}{k_\alpha\lambda^2} \end{bmatrix} \tag{3.44}$$

The elongation terms for the L-shaped cantilever is written in it own tensor $\mathbf{C}''_\Delta$ below.

$$\mathbf{C}''_\Delta = \begin{bmatrix} \alpha\frac{L_a}{EH^2} & & 0 \\ 0 & \frac{\beta}{\lambda}\frac{L_a}{EH^2} & 0 \\ 0 & 0 & 0 \end{bmatrix}$$

3.5 Rotation from Cantilever to Sample Coordinates

Thus far the compliance tensors shown have been in the cantilevers own coordinate system. This was done since it makes the calculations much simpler. However, when engaging the cantilevers to the sample they have typically been rotated as shown in Figure 3.7. To separate the two coordinate systems the cantilever coordinate system is marked with a $''$, e.g. the compliance tensor in the cantilever coordinate system is named $\mathbf{C}''$.

To get from the cantilever system to the sample system two rotations are necessary. First a rotation around the z-axis with an angle of θ. Then a rotation around the y-axis with an angle of ϕ. The rotation matrix for a rotation around the z-axis in three dimensions is given by

$$\mathbf{R}_{z,\theta} = \begin{bmatrix} \cos\theta & \sin\theta & 0 \\ -\sin\theta & \cos\theta & 0 \\ 0 & 0 & 1 \end{bmatrix} \tag{3.45}$$

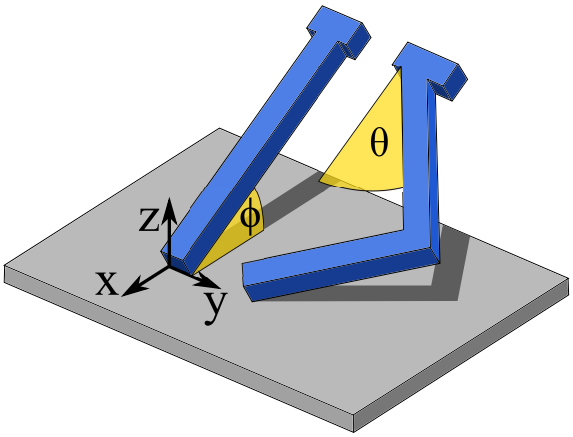

Figure 3.7: Sketch of a straight and an L-shaped cantilever engaged on a surface. The straight probe is only rotated around the y-axis by the angle ϕ. The L-shaped cantilever is both rotated around the y-axis by the angle ϕ, but also around the z-axis by the angle θ. Figure originally from [26].

Note that since the probe is actually upside down when engaged, θ rotates in the opposite direction than what is normal convention. This has been taken into account in the rotation matrix, resulting in the change of sign on the sinus elements.

The rotation matrix around the y-axis in three dimensions is given by

$$\mathbf{R}_{y,\phi} = \begin{bmatrix} \cos\phi & 0 & \sin\phi \\ 0 & 1 & 0 \\ -\sin\phi & 0 & \cos\phi \end{bmatrix} \tag{3.46}$$

The full rotation matrix from cantilever coordinates to sample coordinates then becomes:

$$\mathbf{R} = \mathbf{R}_{y,\phi}\mathbf{R}_{z,\theta} = \begin{bmatrix} \cos\theta\cos\phi & \sin\theta\cos\phi & \sin\phi \\ -\sin\theta & \cos\theta & 0 \\ -\cos\theta\sin\phi & -\sin\theta\sin\phi & \cos\phi \end{bmatrix} \tag{3.47}$$

and the rotation matrix from sample coordinates back to cantilever coordinates is

$$\mathbf{R}^{-1} = \begin{bmatrix} \cos\theta\cos\phi & -\sin\theta & -\cos\theta\sin\phi \\ \sin\theta\cos\phi & \cos\theta & -\sin\theta\sin\phi \\ \sin\phi & 0 & \cos\phi \end{bmatrix} \tag{3.48}$$

This is the same rotation matrix found in [24].
Finally the compliance and stiffness tensor can be transformed from cantilever coordinates into sample coordinates by:

$$\mathbf{C} = \mathbf{R}\mathbf{C}''\mathbf{R}^{-1} \tag{3.49}$$

$$\mathbf{K} = \mathbf{R}\mathbf{K}''\mathbf{R}^{-1} \tag{3.50}$$

3.6 Conclusion to Compliance and Stiffness Calculations

In this chapter the compliance and stiffness tensor for any cantilever that consists of two straight beams connected at the ends, were derived. The compliance tensor can be written

as four unique tensor elements summarized below.

$$
\begin{aligned}
C''_{xx} &= \frac{4L_a^3}{EH^4}\left(\frac{\beta^3}{\lambda^3}+3\frac{\alpha^3}{\lambda^3}\right)\sin^2\eta+\frac{L_a}{EH^2}\left(\alpha+\frac{\beta}{\lambda}\cos^2\eta\right)\\
C''_{yy} &= \frac{4L_a^3}{EH^4}\left(\alpha^3+3\frac{\alpha^3}{\lambda}\cos\eta+\left[3\frac{\alpha^3}{\lambda^2}+\frac{\beta^3}{\lambda^3}\right]\cos^2\eta\right)+\frac{L_a}{EH^2}\frac{\beta}{\lambda}\sin^2\eta\\
C''_{zz} &= \frac{4L_a^3}{EH^4}\left(\alpha+3\frac{\alpha}{\lambda}\cos\eta+3\frac{\alpha}{\lambda^2}\cos^2\eta+\frac{\beta}{\lambda^3}+\frac{\alpha^3}{\lambda^2}\frac{1+\nu}{2k_\alpha}\sin^2\eta\right)\\
C''_{xy}=C''_{yx} &= -\frac{4L_a^3}{EH^4}\left(\frac{3}{2}\frac{\alpha^3}{\lambda}+\left[3\frac{\alpha^3}{\lambda^2}+\frac{\beta^3}{\lambda^3}\right]\cos\eta\right)\sin\eta+\frac{L_a}{EH^2}\frac{\beta}{\lambda}\cos\eta\sin\eta\\
C''_{xz}=C''_{zx} &= 0\\
C''_{yz}=C''_{zy} &= 0
\end{aligned}
\tag{3.51}
$$

where $\lambda = L_a/L_b$, $\alpha = H/W_a$ and $\beta = H/W_b$. Before this compliance tensor can be used it needs to be rotated to sample coordinates, as described in section 3.5.

An experiment is presented in Section 4.3, were the compliance tensor is used to correctly predict the C_{zz} and K_{zz} elements for three cantilevers, with η ranging from 0° to 140°, made from Polyactic Acid.

4 | Vibration Tolerance and Cantilever Contact Types

When designing micro-electrodes, that needs to measure on a micrometer scale or smaller, it is important to ensure that the probe stays in place during the measurements. Even movements on the nanometer scale can cause a large increase in measurement error [23]. In this chapter a parameter named the vibration tolerance, Γ, is introduced, derived and experiments measuring it for two M4PP designs is presented. This chapter will, to a large extend, present the findings of the article "Vibration Tolerance of Micro-Electrodes" by K. Kalhauge et. al. [26].

When a cantilever is engaged on a surface, one of two things will happen: Either the cantilever will slide on the surface, until the forces tangential to the surface becomes lower than the friction; or the cantilever stays still on the surface. These will be referred to as sliding contact and static contact respectively going forward. Sliding contact may be expected for most cantilever designs, while static contact has quite strong requirement. Most 2B cantilevers will form sliding contacts. However, it is possible to design cantilevers to have static contact [23, 24]. For the purpose of calculating the vibration tolerance of a cantilever, it is of greater interest to look at the sliding contact.

The expression presented in this chapter, are in many ways similar to the expression presented in D. H. Petersen's PhD thesis [25]. However, this expression does differentiate it self in some distinct ways. The first, and probably least exciting, it fixes a mistake where $K_{zz}\delta_z$ is used instead of $C_{zz}^{-1}\delta_z$. The second, it introduces the possibility of vibrations in any direction in the xy-plane, instead of looking only at vibrations 45° to the x- and y-axis. Finally the two expressions are fundamentally answering two different questions. The expression presented here gives the minimum relative deflection (deflection divided by engagement depth) in the xy-plane needed, to make a cantilever overcome the static friction and start to slide. The expression given in [25] gives the smallest needed static friction coefficient needed to avoid a specific deflection of the cantilever, from making it slide on the surface.

4.1 Vibration Tolerance and Sliding Contact

It makes sense to calculate the vibration tolerance assuming that the cantilever have reached the point on the surface where the tangential force is zero. Any cantilever that have not reached this point will have a lower vibration tolerance, than a cantilever that

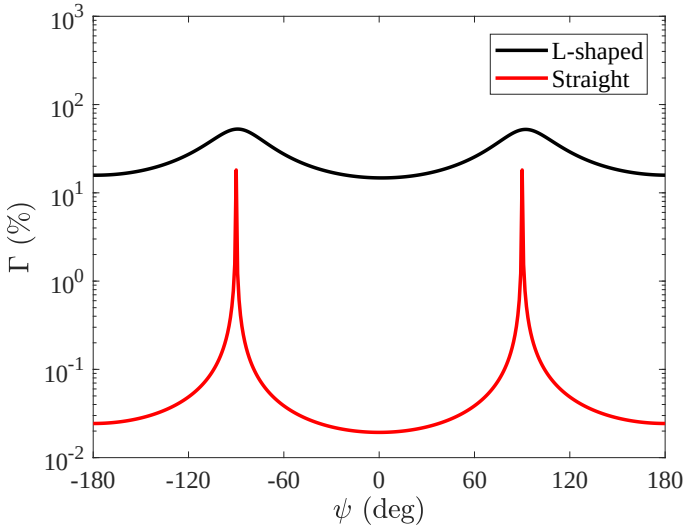

Figure 4.1: Angle dependent vibration tolerance of the straight and L-shaped cantilever used in [26], with a friction coefficient of $\mu = 0.2$. The dimensions are also written in Table 4.2. Figure is a simplificant of the one presented in [26]

have reached it, due to built in spring forces. Additionally, a cantilever moving on the surface will on average move towards this point. Assuming that vibrations are random, any movement, on the surface can be described as a random walk in a harmonic potential, and consequently will normally distribute around the zero tangential force point. The forces affecting a cantilever that has already reached the zero tangential force point can be written as

$$\mathbf{F} = F_z\hat{\mathbf{z}} = C_{zz}^{-1}\delta_z\hat{\mathbf{z}} \tag{4.1}$$

where δ_z is the engage depth. C_{zz}^{-1} will later be referred to as the engage stiffness [26].

From this point we are interested in the strongest possible vibration that does not cause the cantilever to move. This means that the tangential force due to a vibration must not exceed the the total normal force multiplied by the static friction coefficient.

$$|F_T| \leq \mu F_{N,\text{tot}}. \tag{4.2}$$

Thus far the vibrations have simply been mentioned as random. So to formalize the vibrations a bit more, they are now modeled as in-plane sample-body vibrations at an arbitrary polar angle ψ.

$$\tilde{\boldsymbol{\delta}}(t) = A\sin(\omega t)\begin{bmatrix}\cos\psi\\ \sin\psi\\ 0\end{bmatrix} \tag{4.3}$$

where A is the amplitude, ω is the angular vibration frequency and t is time [26]. The total force as a result of this vibration is the sum of the normal force from the engage and the vibrational force

$$\mathbf{F} = C_{zz}^{-1}\delta_z\hat{\mathbf{z}} + \mathbf{K}\tilde{\boldsymbol{\delta}}(t). \tag{4.4}$$

Which can be separated into the normal and tangential parts

$$F_{N,\text{tot}} = C_{zz}^{-1}\delta_z + K_N(\psi)A\sin(\omega t) \tag{4.5}$$

$$F_T = K_T(\psi)A\sin(\omega t) \tag{4.6}$$

where $K_N(\psi)$ and $K_T(\psi)$ are the effective normal and transverse spring constants respectively [26]. Written out, based on the stiffness tensor elements, $K_N(\psi)$ and $K_T(\psi)$ becomes:

$$K_N(\psi) = K_{zx}\cos\psi + K_{zy}\sin\psi \tag{4.7}$$

$$K_T(\psi) = \sqrt{(K_{xx}\cos\psi + K_{xy}\sin\psi)^2 + (K_{yx}\cos\psi + K_{yy}\sin\psi)^2} \tag{4.8}$$

Naturally the worst case scenario happens when the vibrations are at its peak ($|\sin(\omega t)| = 1$). In addition since $K_T(\psi)$ is positive for all values of ψ, the vibration amplitude must fulfill

$$\begin{aligned} K_T(\psi)A &\leq \mu\left(C_{zz}^{-1}\delta_z - A|K_N(\psi)|\right) \\ \Rightarrow \frac{A}{\delta_z} &\leq \frac{\mu C_{zz}^{-1}}{K_T(\psi) + \mu|K_N(\psi)|} \equiv \Gamma(\psi), \end{aligned} \tag{4.9}$$

to avoid the cantilever sliding on the sample in accordance to eq. (4.2) [26]. This we define as the angle dependent vibration tolerance and can be seen in Figure 4.1 for the L-shaped and straight cantilever used in [26]. By choosing the polar angle ψ where the vibration tolerance is at its global minimum, the angle independent vibration tolerance (or simply vibration tolerance for short) is found as

$$\Gamma \equiv \min_{\psi\in\Psi}\Gamma(\psi), \quad \Psi = [-\pi, \pi]. \tag{4.10}$$

This minimum is often found at either $\psi = 0 \pm \pi$ or with a small offset from this. Maximum is typically found at $\psi = \pm\frac{\pi}{2}$ or offset slightly from this [26]. Therefore the vibration tolerance can normally be estimated by

$$\Gamma \approx \Gamma(0) = \frac{\mu C_{zz}^{-1}}{\sqrt{K_{xx}^2 + K_{yx}^2} + \mu|K_{zx}|} \tag{4.11}$$

When vibration tolerance is used in this thesis, it will be calculated using the full expression shown in Equation (4.9) and (4.10).

4.2 Static Contact

It is possible to design cantilevers that are so flexible, that when engaged they do not slide over the surface but stay in place. As mentioned this is what is called static contact. In order for a probe to be of this type the following relation needs to be fulfilled [24, 23],

$$\mu K_{zz} \geq \sqrt{K_{xz}^2 + K_{yz}^2} \tag{4.12}$$

The vibration tolerance for a probe in static contact can be calculated by solving for Γ in the following equation.

$$\begin{aligned} &\mu K_{zz} + \mu K_N(\psi)\Gamma \\ &= \sqrt{(K_{xz} + [K_{xx}\cos\psi + K_{xy}\sin\psi]\Gamma)^2 + (K_{yz} + [K_{yx}\cos\psi + K_{yy}\sin\psi]\Gamma)^2} \end{aligned} \tag{4.13}$$

		Cantilever contact type		
Dimension	Unit	Sliding	Stick-slip	Static
L_a	(mm)	60	60	60
L_b	(mm)	30	30	30
W_a	(mm)	3.9	1.9	1.9
W_b	(mm)	3.9	1.9	1.9
H	(mm)	4.1	5.1	5.1
η	(deg)	0	90	140
θ	(deg)	0	45	70

Table 4.1: Dimensions of the cantilevers used in the stick-slip experiment. The cantilevers have a Young's modulus of $E = 2.347 GPa$ [58] and Poisson's ratio of $\nu = 0.33$ [59]. Reproduced from [57].

Solving this, results in a very long expression. The vibration tolerance calculated from this, is a metric for how large vibrations the static contact can sustain before it turn into a sliding contact and the previous expression for the vibration tolerance is valid instead (Equation (4.9)).

The requirements for static contact was investigated and discussed in F. Wang's paper [24].

4.3 Stick-Slip Contact

This section is largely based on an experiment presented in the article "Vibration Tolerant Two-Beam Cantilevers for Small Pitch Micro-Electrodes" by K. Kalhauge et al. [57]. The experiment was designed in collaboration with A. K. Pedersen, and was performed by A. K. Pedersen.

Thus far everything that is not static contact has been described as a sliding contact. This is overall a good approximation, but also a simplification. As mentioned previously most cantilevers will slide during engagement until the friction becomes larger than the transverse forces. If the engage depth is increased further, the cantilever tip will remain in place until the transverse forces are able to overcome the friction again. This type of contact is called a stick-slip contact.

An experiment was performed, where 3D printed cantilevers were engaged on a scale, at increasingly large engage depths. Three cantilevers were designed using the compliance tensor in Equation 3.51: a straight cantilever that was expected to make a sliding contact and two 2B cantilevers expected to make a stick-slip contact and static contact respectively. The dimensions of the cantilevers are reported in Table 4.1. The cantilevers were drawn and printed in Polyactic Acid (PLA) by A. K. Pedersen on a Ultimaker 2 3D-printer [57]. The results from the experiment are shown in Figure 4.2.

The straight cantilever, expected to have a sliding contact, show contact force in excellent agreement with the expected force from C_{zz}^{-1} (Figure 4.2 a). A slight curving of the force is observed, that is most likely caused by plastic deformation. The disengagement show a large hysteresis, the cause of which is not entirely clear to us, but is probably a result of a change in friction type. The signal on the engage is rather noisy, with several small

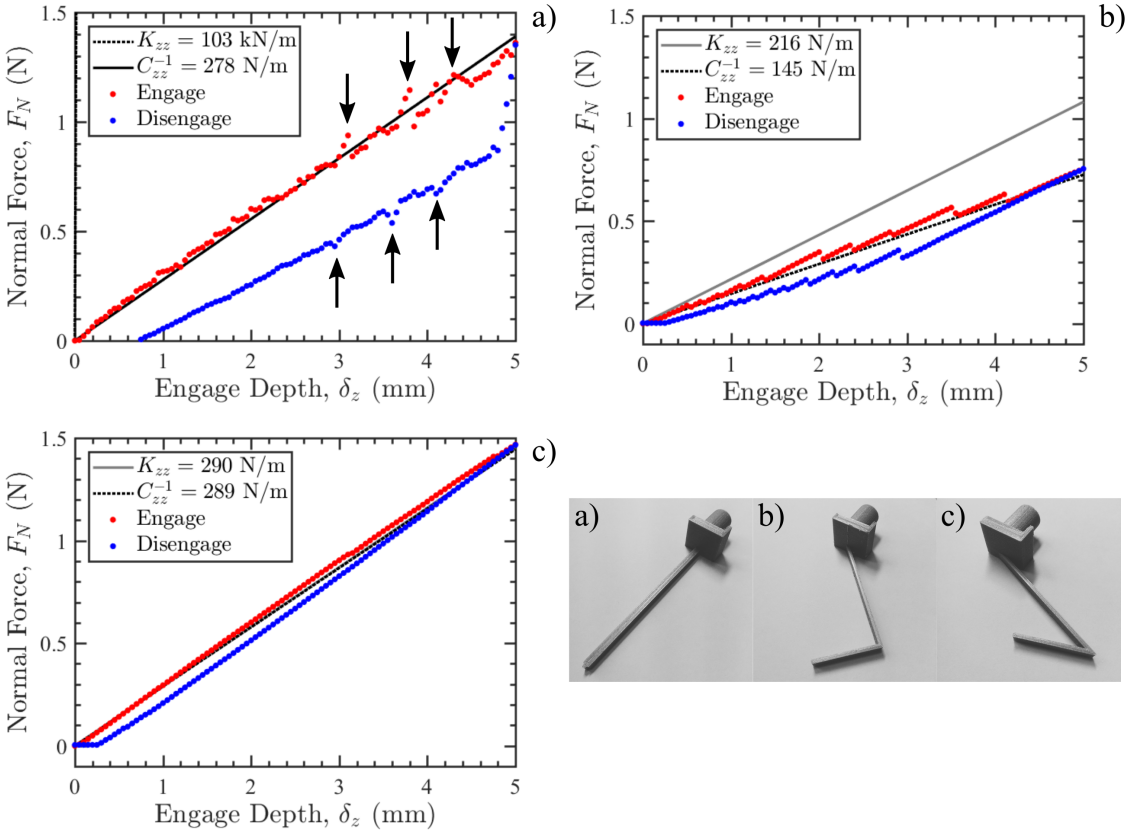

Figure 4.2: Contact force as a function engage depth. The also contains photographs, in bottom right corner, of the three cantilevers used. Red dots indicate engagement. Blue dot indicate disengagement. The dotted gray line and the solid black line are the theoretical curves for K_{zz} and C_{zz}^{-1} respectively. a) Response from the straight cantilever, arrows indicate areas of interest. K_{zz} for this design falls on top of the y-axis. b) Response from 2B cantilever with stick-slip contact. c) Response from 2B cantilever with static contact. Figure originally from [57].

jumps. Our hypothesis is that this is due to surface roughness. There are especially three large disruptions that are reproduced during the disengagement. On Figure 4.2 they are marked with black arrows. Going from engage to disengage the peaks move 0.2mm down in engage depth. This is the same change in engage depth in which the contact force rapidly decrease, right after changing from engaging to disengaging, suggesting that the cantilever tip is stationary in that part [57].

The 2B cantilever, expected to have a static contact, (Figure 4.2 c) show no sudden changes in contact force and only minimal hysteresis, which is probably due to plastic deformation. Based on this it seems fair to say that the cantilever tip have indeed remained stationary during the engage. Since the values of K_{zz} and C_{zz}^{-1} are so similar it impossible based on these measurements to determine which the force follows [57].

Now with both sliding and static contact examined, the cantilever, expected to have a stick-slip contact, is considered. The contact force is shown to rise linearly until they suddenly drop, and then start rising again. Repeating multiple times during the engagement. The phases in which the contact force is rising are parallel to the line from K_{zz}, suggesting that the cantilever tip is stationary in these phases. When the contact force drops, it

L-beam		I-beam	
Symbol	Value (µm)	Symbol	Value (µm)
H	9.7	H_{I}	9.9
L_a	92.1	L_{I}	201.0
L_b	36.9		
W_a	4.8	W_{I}	12.0
W_b	2.3		
θ	45°	θ_{I}	0°
η	90°	η_{I}	0°
ϕ	30°	ϕ_{I}	30°

Table 4.2: Dimensions of the two cantilevers designs used in the vibration tolerance experiments. The electrode pitch of both probes is 20 µm. Table was taken from [26].

obtains the value described by the line from C_{zz}^{-1}, suggesting that the cantilever tip have moved to a position with close to zero transverse force. Since the cantilever always returns to the C_{zz}^{-1} line, it will on average behave like a sliding contact probe [57]. This in turn supports the use of (4.9) to calculate the vibration tolerance for these cantilevers.

4.4 Vibration Tolerance Experiments

Vibration experiments were performed by Henrik H. Hartmann using two types of probes, a straight and an L-shaped. The L-shaped had a complete 90° bend at the elbow. The dimensions for the two cantilever types are shown in Table 4.2, and the angle dependent vibration tolerance for these design are shown in Figure 4.1.

For the experiments the probes were engaged on either Indium-Tin-Oxide (ITO) or silicon. While engaged on the surface, electrical measurements were continuously performed while the vibration amplitude was increased. The vibrations were supplied by a small piezoelectric element that was driven at a frequency of 100Hz. The point of probe failure due to vibrations were defined as the minimum amplitude required to make the electrical measurement fail five times in a row. Using this method the vibration tolerance was measured for engagement depths ranging from 500nm to 3000nm. Where the engagement depth was measured using a strain gauge with an error of max 200nm.

It quickly became clear during analysis that due to how stiff the straight cantilever is in the length direction, a system compliance element had to be added to the straight cantilevers C''_{xx} element. This element represents the compliance of the rest of the system, i.e. the probe body, probe holder and the rest of the machine. To estimate this compliance element. It was used that it appeared that the straight cantilever had made indentations in the ITO. This had prevented it from sliding on the surface. Modeling the vibration tolerance for this situation was done assuming that $\mu \to \infty$ giving:

$$\Gamma(\psi) = \frac{1}{C_{zz}|K_N(\psi)|} \tag{4.14}$$

By fitting this to the measurement on ITO with the straight probe, gave a system com-

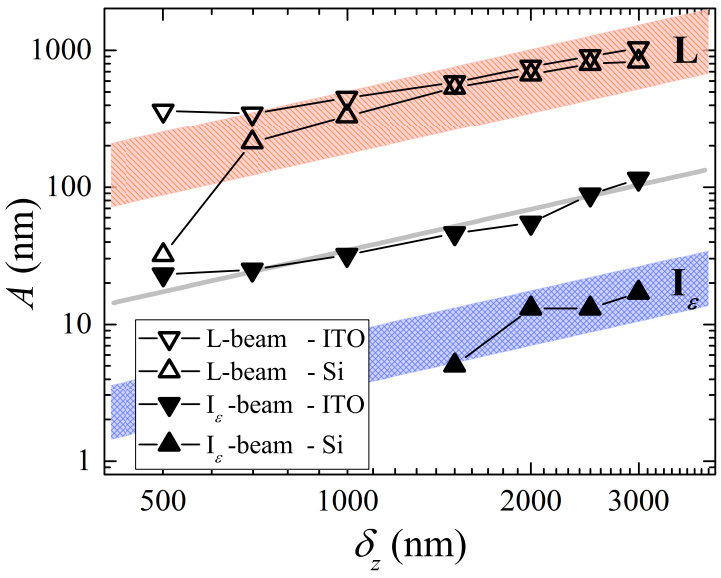

Figure 4.3: Results from measurements of the vibration tolerance of two cantilever types. The filled symbols are measurements with a straight cantilever. The hollow symbols are measurements with an L-shaped cantilever. Theoretical predictions are shown as blue and red areas. The full gray line represents a straight probe engaged on a surface with artificially large friction coefficient ($\mu \to \infty$). The plot was reproduced from [26].

pliance of $\varepsilon = 0.2mm/N$.

$$\mathbf{C}''_{\varepsilon} = \begin{bmatrix} \varepsilon & 0 & 0 \\ 0 & 0 & 0 \\ 0 & 0 & 0 \end{bmatrix} \tag{4.15}$$

This compliance tensor was added to the straight probe, effectively increasing its C''_{xx} element by roughly an order of magnitude, But was not added to the compliance tensor of the L-shaped probe, since it would only change the element size by less than 0.5%.

The results from the experiment are shown in Figure 4.3. Figure 4.3 shows that there is a good correlation between the theoretical predictions for the L-shaped probe and the experiments. The measurement error on the vibration amplitude (a few nm) meant it was impossible to measure the vibration tolerance for the straight beam below an engagement depth of 1500nm. The plot also shows that the measurements with the straight probe on ITO has significantly higher vibration tolerance than what is expected for a friction coefficient between 0.2 and 0.6. The gray line sows the fitted system compliance assuming $\mu \to \infty$.

5 | Optimization of Cantilever Design

In this chapter the analytical expressions for the vibration tolerance (4.9) and the compliance tensor (section: 3.3) are used to study how changing different design parameters for a cantilever will change its mechanical behavior. Finally the expressions are used to optimize an existing cantilever design.

The cantilever design that is going to be optimized and is going to form the basis for this study, is the probe that A. Cagliani, et al. [14] used in their paper on improving measurement precision. This probe had a smallest possible electrode pitch of 1.5µm, which ultimately influences which samples it can measure on. The probe from [14] has the dimensions shown in Table 5.1 and a sketch of it is shown in Figure 5.1.

5.1 Study of the Effect of Cantilever Parameters on Mechanical Behavior

Using the design in Table 5.1 as a basis. A study of the different parameters effect on the mechanical behavior of a cantilever was initiated. Due to the complexity of the problem (seven possible parameters to optimize), a reduction of the parameter space is necessary before continuing.

Parameter Space

We decided to keep the total length constant throughout the study for easier comparison of designs. In general a longer probe will cause the stiffness of the cantilever to fall while the vibration tolerance stays relatively unchanged. The total length is given by

$$L_T = L_a \cos\theta + L_b \cos(\eta - \theta). \tag{5.1}$$

While the total length is fixed, the length of beam a and beam b were chosen as variables dependent on the two angles, the total length and the ratio $\lambda = L_a/L_b$. From experience working with the optimization of specific probe designs, we knew that the best vibration

Dimension	Value
L_a	8.7µm
L_b	4.3µm
W_a	0.91µm
W_b	0.50µm
H	1.11µm
θ	20°
η	40°
E	69GPa
ν	0.17
Γ	0.0157
C_{zz}^{-1}	13.1 N/m

Table 5.1: Design Parameters for the probe in [14]. Young's modulus and Poisson's ratio are for SiO_2 and are taken from [53]. The stiffness and vibration tolerance were calculated using the expressions presented in this thesis.

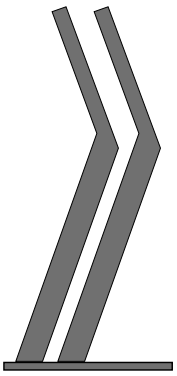

Figure 5.1: A sketch of two cantilevers from 5.1, placed with the minimum spacing.

tolerance is achieved for λ between one and five.

$$L_a = \frac{\lambda L_T}{\lambda \cos\theta + \cos(\eta - \theta)} \tag{5.2}$$

$$L_b = \frac{L_T}{\lambda \cos\theta + \cos(\eta - \theta)} \tag{5.3}$$

$$\lambda \in [1; 5] \tag{5.4}$$

This reduces the number of parameter that needs to be studied by one.

From experience it has also become clear that the highest possible vibrational tolerance is always achieved when the width of beam b is as small as possible. How small this can be made depends heavily on the fabrication method chosen. Cantilevers of the dimensions we are looking at are typically defined using UV-lithography. As a consequence we have chosen a Critical Dimension (CD) of 500nm. While it is possible to do smaller CD with some UV-lithography systems, 500nm should be achievable by most modern systems.

$$W_b = 0.5\text{µm} \tag{5.5}$$

This further reduces the number of parameters that needs to be studied.

In this study the height and the width of beam a is chosen in rough steps to show their overall effect on the mechanical behavior. Three heights were chosen; $H = 1.5$µm, $H = 2.0$µm and $H = 2.5$µm, two widths were chosen; $W_a = 0.5$µm and $W_a = 1.0$µm.

We decided that any angle for θ more than 45° is not relevant. If the angle is increased beyond this angle, beam a begins to hug the probe-body. In the same track, η is at least the same value as θ. If η was smaller the overall direction of the cantilever would not be in the x-direction, meaning a cantilever with a smaller θ could have been chosen instead. Additionally, η is chosen to be less than $60° + \theta$.

$$\theta \in [0; 45°] \tag{5.6}$$

$$\eta \in [\theta; \theta + 60°] \tag{5.7}$$

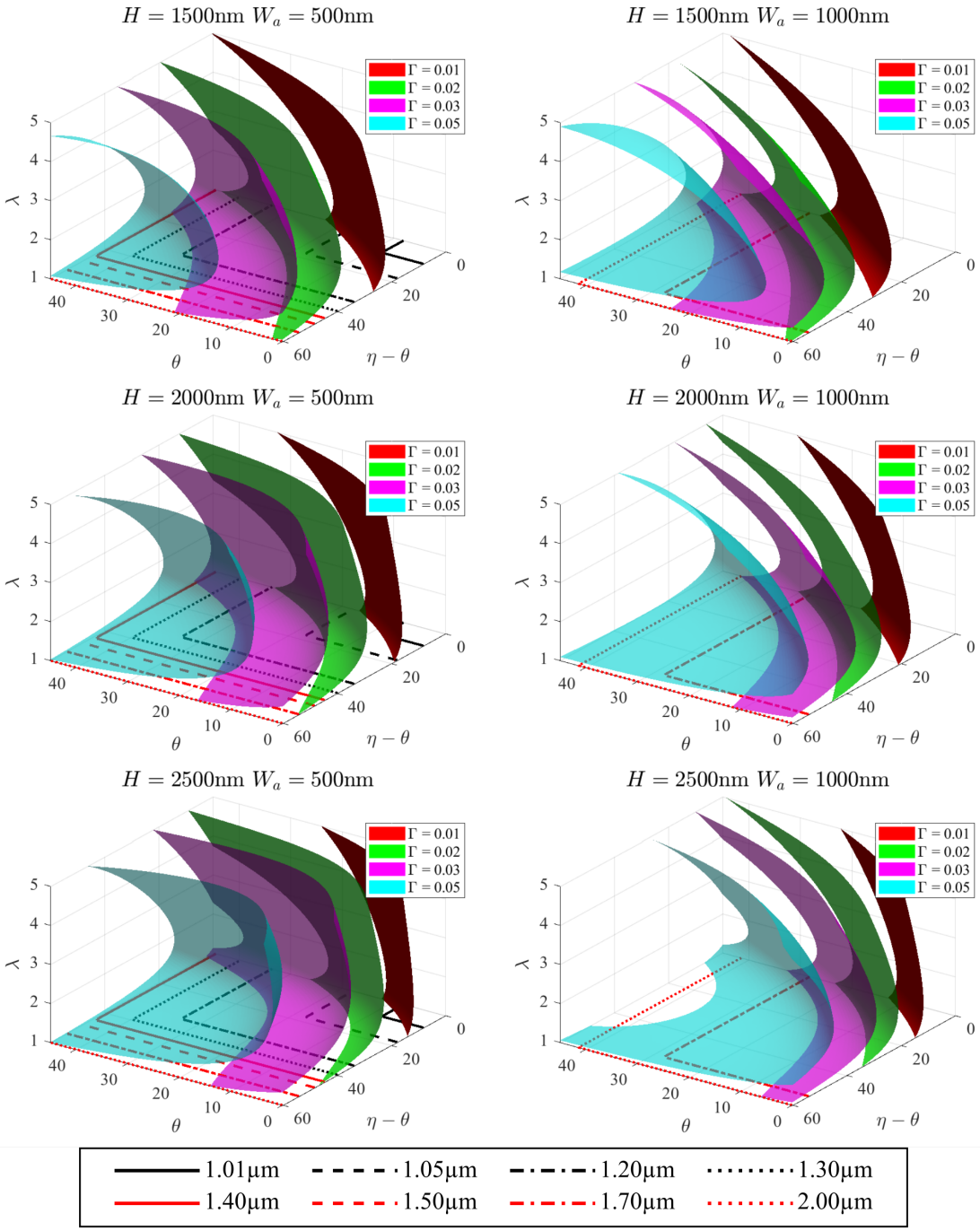

Figure 5.2: Shell plot of the vibration tolerance as a function of θ, $(\eta - \theta)$ and $\lambda = L_a/L_b$. Each shell shows the limit between going from under to over the value shown in the legend. Pitch lines are shown on the θ $(\eta - \theta)$ plane, these shows which areas of the angle plane were it is possible to achieve the given pitch. Notice that as the width increases some pitches are no longer possible anywhere in angle plane.

This has reduced the total number of parameters to five making it possible to make a three dimensional shell plot for each combination of W_a and H, with θ, $(\eta - \theta)$ and λ on the axis. The result from this is shown in Figure 5.2 and Figure 5.3.

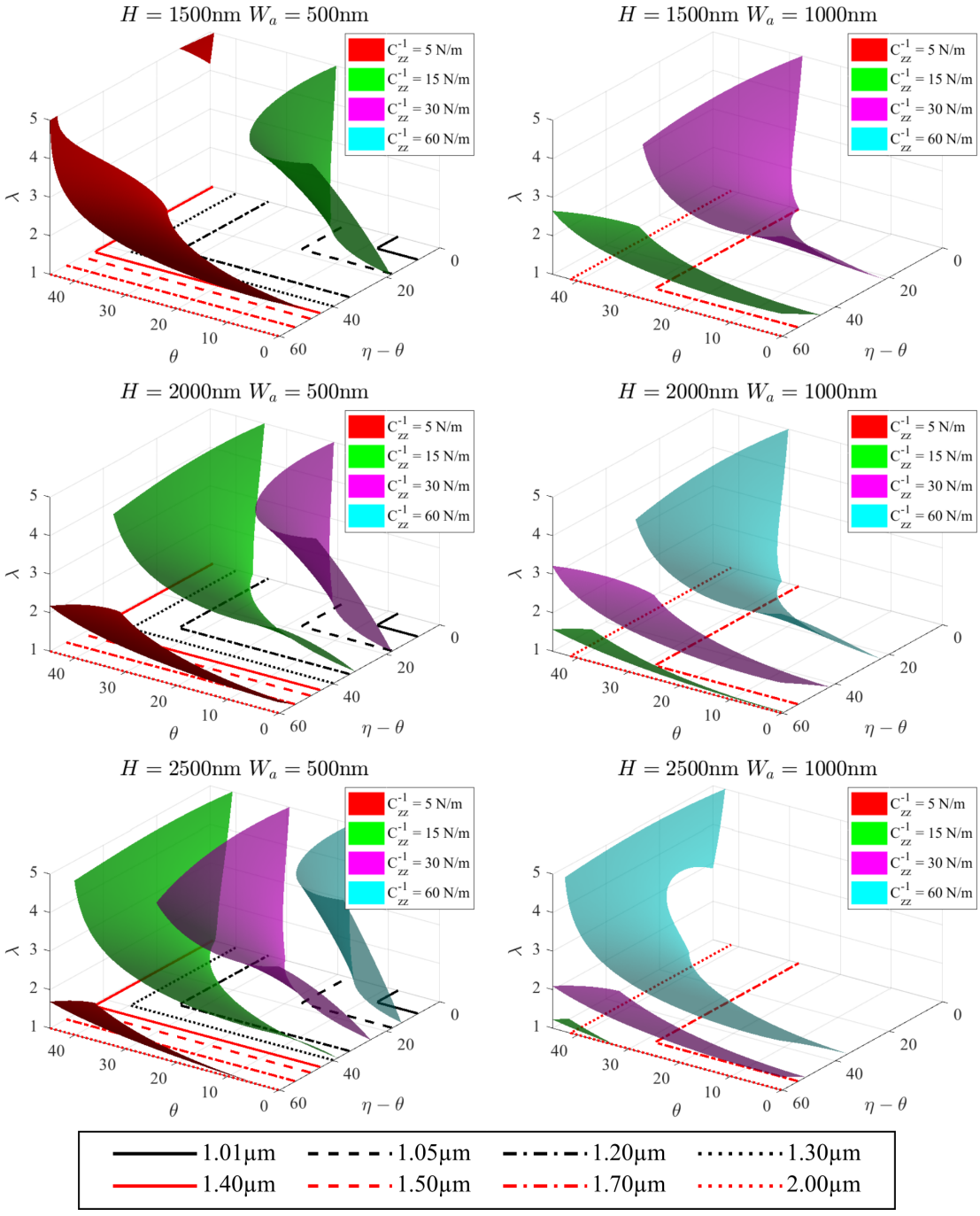

Figure 5.3: Shell plot of the inverse of the zz-element of the compliance tensor, here referred to as the engage stiffness, as a function of θ, $(\eta - \theta)$ and $\lambda = L_a/L_b$. Each shell shows the limit between going from under to over the value shown in the legend. Pitch lines are shown on the θ $(\eta - \theta)$ plane, these shows which areas of the angle plane were it is possible to achieve the given pitch. Notice that as the width increases some pitches are no longer possible anywhere in angle plane.

The plots of the vibration tolerance (Figure 5.2) show that going towards higher angles increases the vibration tolerance. This is as we would expect. The plots also show that increasing either the width of beam a or the height will also increase the vibration tolerance. This was not immediately clear from the offset, and is most likely caused by

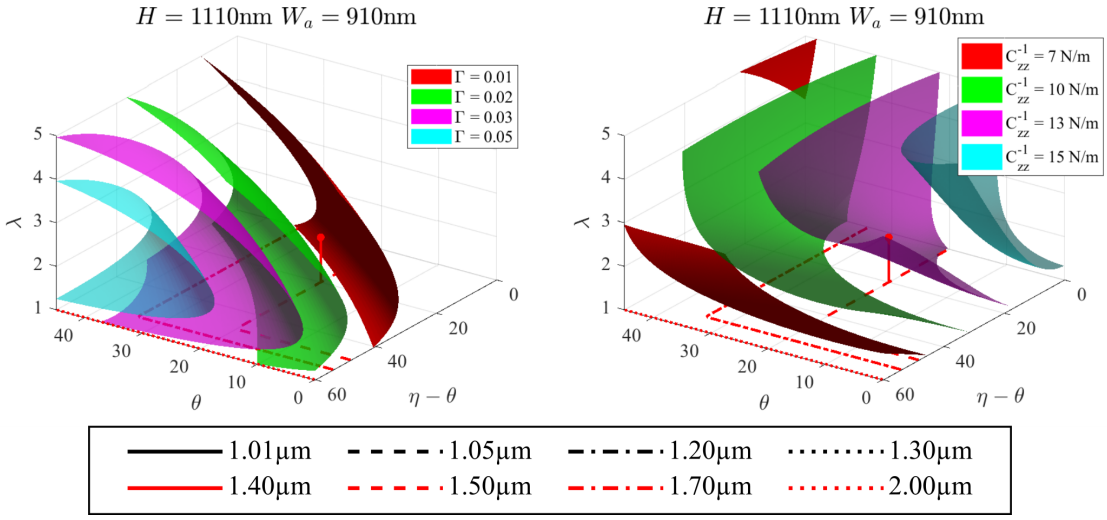

Figure 5.4: Shell plot of the cantilever shown in Table 5.1. The shell shows the what happens if either one of the angles or λ is changed. The small red dot, on a red pillar, indicates were the cantilever design is in this parameter space. Pitch lines are shown on the θ $(\eta - \theta)$ plane, these shows which areas of the angle plane were it is possible to achieve the given pitch. (Left) Shell plot of the vibration tolerance. (Right) Shell plot of the engage stiffness.

the additional height causing the engage stiffness (C_{zz}^{-1}) to increase while the transverse stiffness (K_T) is largely unchanged. Lastly, as mentioned earlier, the shape of the surfaces makes it clear that the optimal value for λ is indeed between one and five.

Now looking at the engage stiffness plots (Figure 5.3), the engage stiffness decreases as the angles increase. From Equation (4.9) it is known that the vibration tolerance is linearly dependent on the engage stiffness. Which might make the fact that the vibration tolerance increases while the engage stiffness decreases slightly surprising. However when increasing the angles all stiffness elements decreases. The other stiffness elements compensate for the lower engage stiffness, thereby increasing the vibration tolerance. It is also clear from the plots that increasing λ will generally increase the engage stiffness. This is clearer from the plots with high values of W_a. That is as expected since high λ means that most of the cantilever length is in L_a, thereby making it look more like a straight cantilever.

The code used to calculate these designs are shown in Appendix A.5 and proved to be roughly 225000 times faster than doing finite element simulations. The plotting script is shown in Appendix A.6.

5.2 Same Pitch Optimization of Cantilever

The goal of the optimization presented in this section, is to improve the vibration tolerance of the cantilever shown in Table 5.1. This has to be done while keeping the electrode pitch, engage stiffness and widths constant. Figure 5.4 shows a shell plot of the cantilever design and its surroundings in θ, $(\eta - \theta$ and λ. On the figure the specific cantilever design is marked as a red dot.

From the pitch lines on Figure 5.4, we see that it is possible to increase the angle η so that $\eta - \theta = 48.2°$, without changing the minimum possible pitch. From the study done in the previous section, and Figure 5.4 (left), it is known that increasing any of

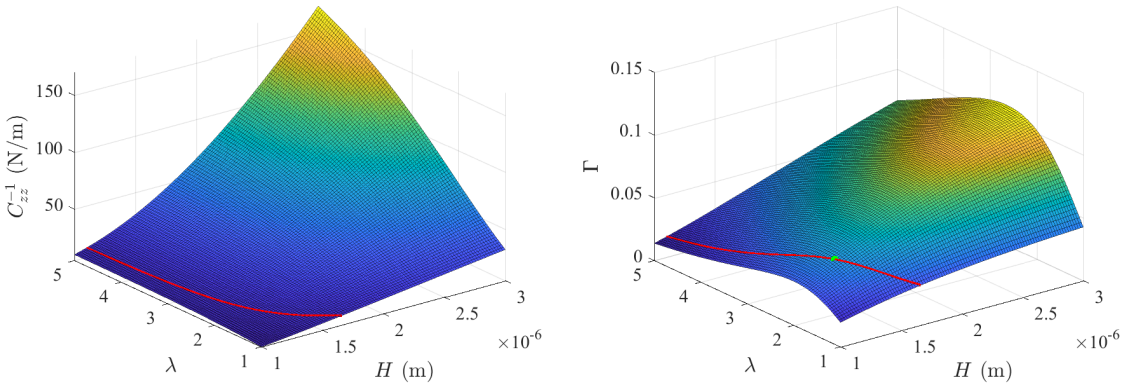

Figure 5.5: (Left) Plot of the engage stiffness for the optimized cantilever as a function of H and λ. The red contour line shows the design with the same engage stiffness as the original cantilever. (Right) Plot of the vibration tolerance for the optimized probe. The red line is the combinations of H and λ that formed the contour line from the engage stiffness plot. The green dot indicates where on the red line the vibration tolerance is largest.

the angles also increases the vibration tolerance. However, by moving to this point, the engage stiffness has decreased. It is possible to compensate for this by modifying some of the other parameters. By changing the angle η, an optimization based on the angles have already been made. This leaves H and λ.

To find the combinations of H and λ that has the desired engage stiffness, the engage stiffness was calculated for all combinations of 101 values of $H \in [1, 3]$µm and $\lambda \in [1, 5]$, totaling 10201 combinations. The engage stiffness surface from this is shown in Figure 5.5 (left). On this surface a contour line corresponding to the desired engage stiffness (13.1N/m) is traced. This contour line is shown in the figure as a red line. All of the designs on this line have the desired engage stiffness, so by tracing the line to a surface plot of the vibration tolerance, the design with the best vibration tolerance can be found by simply maximizing. The vibration tolerance surface is shown in Figure 5.5 (right). The optimal point is shown on this figure with a small green dot. The code used for the optimization is shown in Appendix A.7.

The optimized solution gives $H = 1275$nm, $\lambda = 1.84$ and of course $\eta = 68.2°$, and results in a constant engage stiffness but an increase in vibration tolerance by a factor of three, from 1.6% to 4.7%. To update Figure 5.4 with the new cantilever design, the plot needs to be made for the new height. The new plots are shown in the top row of Figure 5.6. The blue dot indicates where in the parameter space the new solution is. The red dot indicates were the original probe design were in $(\theta, \eta - \theta, \lambda)$ space, but does represent a design with a different height than what the plot shows.

5.3 Optimize Cantilever for Specific Pitch

The goal in this section is to optimize original cantilever to work with a minimum electrode pitch of 1.1µm while still having the same engage stiffness and critical dimension as the original. From some simple geometry it can be realized, that in order to reduce the pitch to 1.1µm, the width of beam a has to be reduced. There is however a point where one can choose between slightly higher angles or a slightly wider beam a. From the plots in

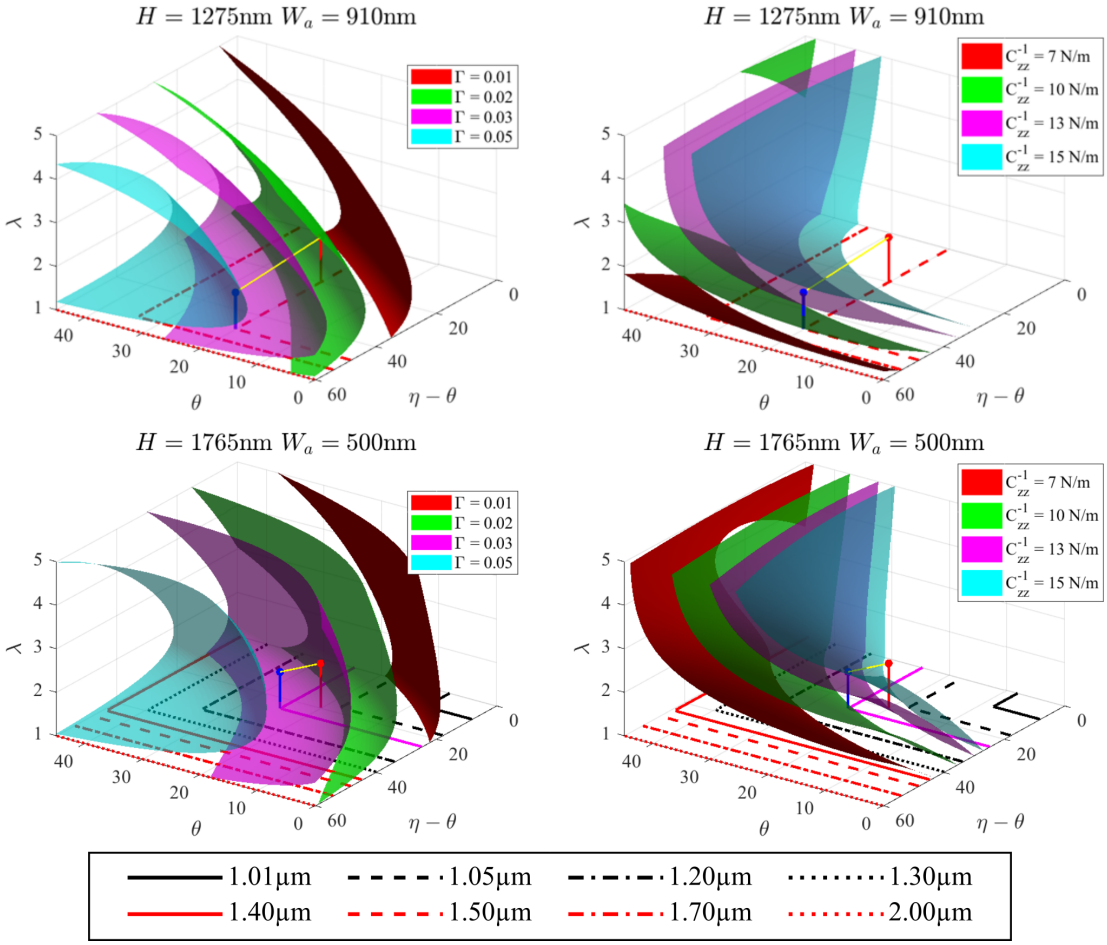

Figure 5.6: Top row: Shell plot of the optimized cantilever keeping the same pitch. Bottom row: Shell plot of the optimized cantilever with a pitch of 1.1μm. The shells show the what happens if either one of the angles or λ is changed. The small red dot, on a red pillar and small blue dot on a blue pillar, indicates were the original cantilever and new design is in this parameter space respectively. Pitch lines are shown on the θ (η − θ) plane, these shows which areas of the angle plane were it is possible to achieve the given pitch. (Left) Shell plot of the vibration tolerance. (Right) Shell plot of the engage stiffness.

Figure 5.2 it is known that both increasing the width of the first beam and increasing the angles will result in a larger vibration tolerance. Since it is hard to determine before hand which will have the greater effect, the angles θ and η will be tied to the value of W_a. So that for any width W_a the largest possible angles are chosen.

$$\theta = \arccos\left(\frac{W_a + \mathrm{CD}}{s}\right) \tag{5.8}$$

$$\eta = \arccos\left(\frac{W_b + \mathrm{CD}}{s}\right) + \theta \tag{5.9}$$

where CD is the critical dimension, and s is the electrode pitch.

An Optimization of the height and width of beam a is performed in the same manner as explained in the previous section. During this optimization λ has not been changed, and perhaps more optimized choices of λ exists. so the optimization in H and W_a is repeated several times. Each time the value of λ is changed slightly. In the end we have a list of optimized designs, each one corresponding to a specific λ. We then simply choose the

Cantilever	Original	Same Pitch	Smaller Pitch
(Analytical) $\boldsymbol{\Gamma}$	1.57%	4.77%	3.82%
(Simulation) $\boldsymbol{\Gamma}$	1.46%	4.59%	3.95%
(Analytical) $\boldsymbol{C_{zz}^{-1}}$	13.1N/m	13.1N/m	13.1N/m
(Simulation) $\boldsymbol{C_{zz}^{-1}}$	13.2N/m	13.4N/m	13.7N/m
$\boldsymbol{L_a}$	8.70µm	9.38µm	8.71µm
$\boldsymbol{L_b}$	4.30µm	5.10µm	4.73µm
$\boldsymbol{\lambda}$	2.02	1.84	1.84
$\boldsymbol{W_a}$	0.91µm	0.91µm	0.50µm
$\boldsymbol{W_b}$	0.50µm	0.50µm	0.50µm
$\boldsymbol{H}$	1.11µm	1.28µm	1.77µm
$\boldsymbol{\theta}$	20.0°	20.0°	24.6°
$\boldsymbol{\eta}$	40.0°	68.2°	49.2°

Table 5.2: Table containing the parameters of the original design as well as the two optimized designs. Simulations consisted of finite element modeling of the compliance and stiffness tensor elements using COMSOL. Finite element model shown in Appendix A.9

design in the list that have the highest vibration tolerance.

The new design has a height of $H = 1765$nm, a width of $W_a = 500$nm, a $\lambda = 1.84$, a $\theta = 24.62°$ and an $\eta = 49.24°$. This design has a vibration tolerance of 3.82%, slightly lower than the optimized probe with the large pitch, but still an improvement of a factor of 2.4 over the original. The new design is shown in the bottom row of plots in Figure 5.6.

5.4 Conclusion to Cantilever Optimization

What have been demonstrated here is the basics of how to optimize the vibration tolerance for a given design. Naturally this is very useful, but it is not the be all and end all of cantilever designs. Parameters such as the lead resistance from the shoulder to the tip are also very important. The method shown here should therefor not be seen as the initial go to for designing a cantilever, but rather the last step, when a lot of constrains on the design have already been imposed by outside sources. In that case this method can help squeezing a little extra out of the cantilever without compromising on any of the important parameters.

The designs that was found in this chapter are summarized in Table 5.2 along with results from finite element simulations of the same designs.

The discrepancies shown between the analytical and numerical results, could be caused by both the simulation and the analytical model. The simulations errors could have come from the meshing or the simplifications to the model (see Appendix A.9) in order make it sound for all designs. For the analytical model a number of assumptions were made that might have led to slight inaccuracies. In the end the difference seen between the models, are smaller than what can be expected from fabrication variations.

Part II

Electrical Characterization of MoS_2

6 | Field Effect Integration in Micro Four-Point Platform

In this chapter the work that have gone into making a functioning setup for doing field effect measurements is presented and explained. This will consist mainly of two parts: the physical modifications to the microRSP-M200 semiautomatic tool from CAPRES [60], now a part of KLM; and the LabView code used to run the experiments.

6.1 M200 Modification

The microRSP-M200 semiautomatic tool (or M200 tool for short) is a machine that uses M4PP to typically either do sheet resistance measurements, or micro-Hall measurements. To do this an alternating current is applied between the two source electrodes while measuring the potential between the two sensing electrodes. By using a AC signal as input, the sensing can be filtered using a lock-in amplifier at the same frequency. Using a lock-in technique has a huge effect on the precision of the measurements, allowing for much better measurements.

When doing field effect measurements, the source has to be DC instead of AC and a potential has to be sourced instead of a current. This means that not only is it not possible to use a lock-in amplifier to improve the signal to noise ratio, it is also necessary to circumvent the entire measurement equipment already present in the M200 tool, replacing it with something else. In this section, what that something else is, will be discussed.

At DTU Nanotech (now DTU Physics) there already existed a setup for doing field effect measurements using macroscopic probes on lithographically defined structures. The setup was built by, former employee at DTU Nanotech, David Mackenzie. It was quickly decided that instead of inventing the wheel again, the modification to the M200 tool would be based on this setup. The setup consists of two Keithley 2400 sourcemeters and a Keithley 2700 multimeter with a Keithley 7709 matrix module. All of which is connected using GPIB cables. The sourcemeters provided either the source drain voltage needed in the measurements or the gate voltage. At the same time the multimeter measures the potential drop across the source electrodes. The matrix module is used to switch between different configurations on the M4PP. The basic setup of sourcemeters and multimeters are mostly the same between the fixed electrode setup and the M200 modification. The big difference between the setups, was located in the connection between the matrix module and the sample.

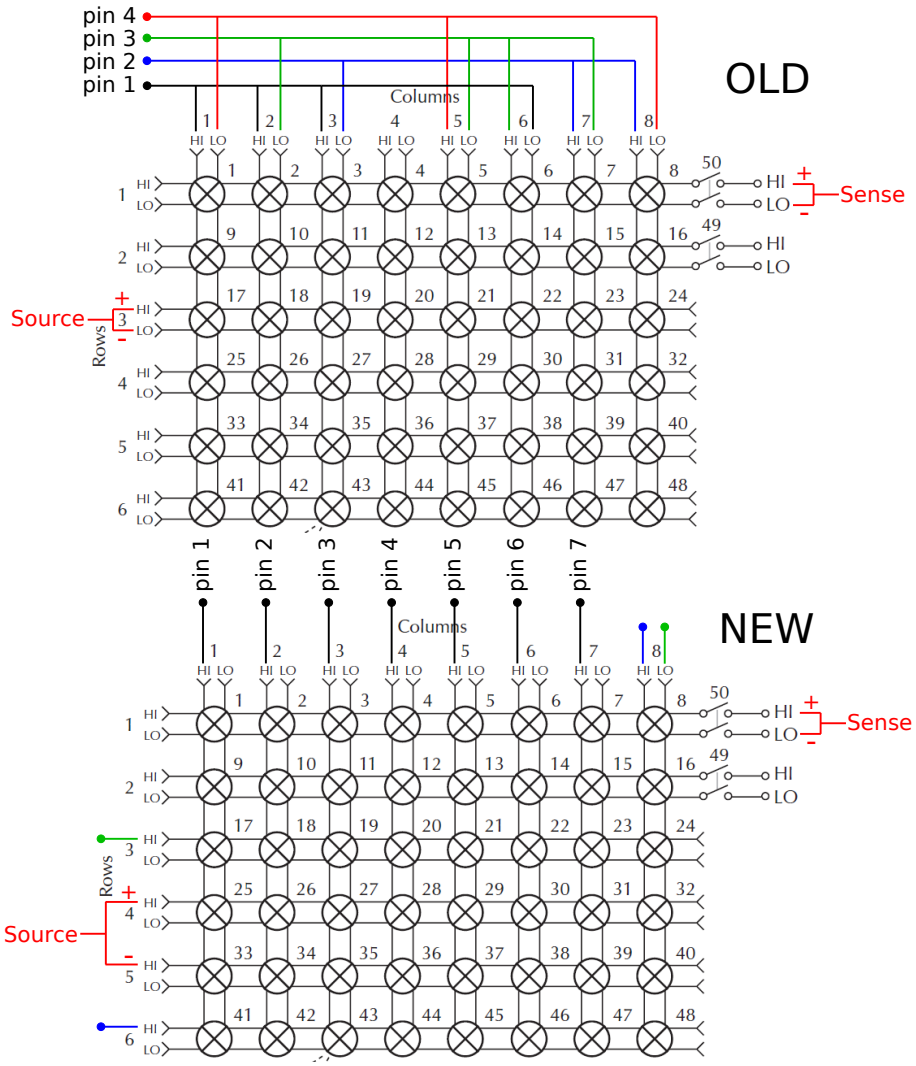

Figure 6.1: Schematic of the switch array in the Keithley 7709. The user can connect to the rows and columns. Schematic reprinted from the "Model 7709 User's Guide" by Tektronix [61]. The old and new wiring is shown drawn on top of the schematic at the top and bottom of the figure respectively.

In the fixed electrode setup the matrix module only needed to be able to multiplex between four contacts, and only the basic six configurations at that. On the M200 tool it is possible to use probes with more electrodes than four. Throughout the measurements a probe with seven electrodes were used, a so called Micro Seven-Point Probe (M7PP). With a M7PP only four electrodes are used in a measurement at any time, but it allows the user to choose any of the possible sub-probes (a selection of four electrodes) and to use multiple different sub-probes during the same engage. In the new setup, in order to take advantage of the M7PP, the matrix module needs to be able to choose any sub-probe as well as any configuration for said sub-probe. This required a complete rework of the wiring, connecting the matrix module to the electrodes, and a rewriting of the program controlling the measurements.

A schematic of the switching array in the matrix module is shown in Figure 6.1 with the old and new wiring. The matrix module consist of multiple rows and columns that can be connected by opening or closing the channels numbered 1 through 48 on the schematic.

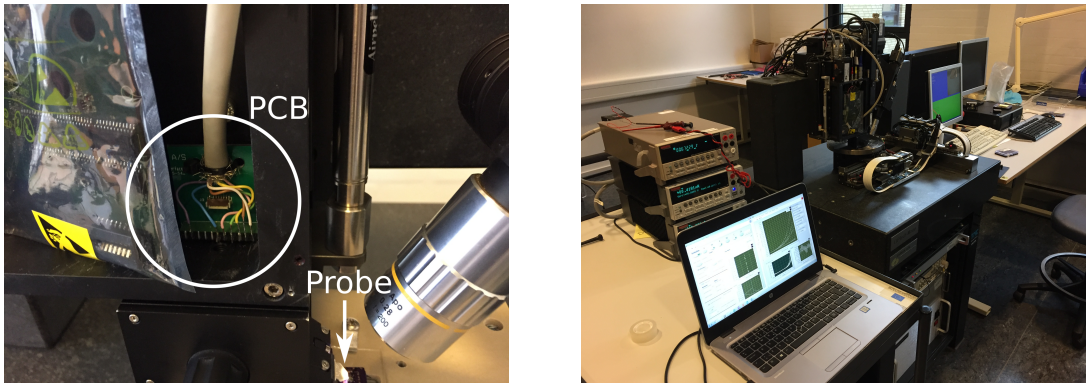

Figure 6.2: (Left) Photograph of the PCB used to connect the matrix module to the probe. On the picture it is mounted inside the machine, with the PCB connecting to the original measurement equipment inside the EDS bag. (Right) Photograph of the entire setup.

Doing so connects Hi with Hi and Lo with Lo. The original setup used the fact that it is possible to write six configurations using only six Hi-Lo electrode pairs (14, 23, 13, 24, 12, 43). So that all six configurations can be written by choosing a pair for the source-drain and a pair for the sensing. As an example 14 could be chosen for the source-drain, so that source is on electrode 1 and drain is on electrode 4, meanwhile sensing would be on 23, so that sense high is on electrode 2 and sense low is on electrode 3. Each of these pairs were then hard wired unto column in the matrix module. In this setup the sourcemeter providing the source and drain is connected to row 3, while the multimeter measuring on the sense electrodes are connected to row 1. This works very well as long as only one sub-probe is available. When the number of possible electrodes goes up this is no longer a possible way to do it.

In the new system each electrode of the M7PP is connected to the Hi of a column. The eighth (and last) column is then connected with its Lo to the Hi on row 3 and its Hi to the Hi on row 6. This is necessary since the multimeter is automatically connected to channel 50 directly. The sourcemeter is then connected with source on Hi on row 4 and ground on Hi on row 5. This setup allows any of the electrodes to act as either source, drain or any of the sensing electrodes as the user sees fit. Thereby allowing for the use of all sub-probes and configurations.

The matrix module is connected to the probe using a Printable Circuit Board (PCB) that is designed to interface with CAPRES probe heads. A picture of the PCB connected to probe head is shown in Figure 6.2 (left). A photo of the entire setup connected is shown in Figure 6.2 (right).

6.2 LabView Program

To connect the equipment and to automate the measurement process, a LabView program was used. This program was based on a program originally written by David Mackenzie. Some of the core code was kept but large segments were replaced to better serve the needs in the new setup. In this section some of the key functionalities and sub-programs are presented and discussed.

Configuration	Order	Example: 1357
A	1234	1357
A_P	2143	3175
B	1243	1375
B_P	2134	3157
C	1432	1753
C_P	3214	5317

Table 6.1: Table of the ordering used to create the configuration strings. The example is based on the sub-probe string '1357'.

6.2.1 Multiplex Compiler

The biggest change to the program, is the new compiler for the multiplexer. The compiler is the part of the program that translates the user choices of configurations (and in the new version, sub-probe) to a series of machine code that can be read by the matrix module. The original program was designed to control the measurements of a fixed electrode vdP setup. In this setup the choice of contacts to use on the surface, was selected by physically moving individual pins to the appropriate contacts. Additionally since the setup is focused on a square vdP setup, only the six basic configurations had to be taken into account. For these reasons the original compiler was quite simple. The only input to the original compiler was the six configurations, which were hard-coded to give a specific piece of machine code each. The new compiler was designed for the use of a M7PP. The addition of three extra pins, changes the number of possible sub-probes from one to 35. On top of this, due to how M4PP works, it can be interesting to also have some of the none basic configurations, so all 24 configurations should be possible. This is a total of 840 possible combinations. In other words way more combinations than is practical to hard code for.

Before continuing with the explanation of how the compiler works, a few code naming choices has to be explained. Code wise all sub-probes are given to the program as a sub-probe string of four digits. This string translates to how an A-configuration would look in the chosen sub-probe. With the first number being the position of the source pin, the second the position of high sense, the third the position of low sense and the fourth the position of the ground (See Figure 2.1). Unless some of the 18 non-traditional configurations are wanted, the string should be in ascending order. So as an example if the user wants to do the standard six-configuration using the sub-probe consisting of electrode one, three, five and seven, the program should be given the string '1357'.

The first part of the new compiler takes the input sub-probe string, and combines it with the chosen configurations. This is done by taking the sub-probe string and ordering it according to the chosen configurations, resulting in the configuration string. How a sub-probe string should be ordered to give an A, A_P and so on, is hard coded in the program. The ordering is shown in Table 6.1. The configuration strings are stored in a configuration array and passed to the next part of the compiler.

Since each of the source pins and each of the sense pins have a row in the matrix module, and each electrode on the M7PP has a column. The channels that need to be closed can easily be found as a fixed number unique to the pin plus the electrode number. I this case the numbers are 16, 24, 32 and 41 for the sense low, source, ground and sense high respectively. Additionally since the matrix module was installed in slot one of the

1234 *A*-config	**Electrode #**	**Pin #**	**Module Slot**	**Channel #**
Source	1	24	100	125
Ground	4	32	100	136
Sense Hi	2	40	100	142
Sense Lo	3	16	100	119

Table 6.2: Example of how to calculate the channels to close for a measurement using an A configuration for the sub-probe 1234

multimeter the channel numbers have to be increased by a further 100. An example of the calculation of the channel numbers are shown in Table 6.2 for an A configuration with sub-probe using electrodes 1 through 4. Finally the channel 108 and 150 also needs to be closed to connect the multimeter to the probe. Channel numbers are shown in the matrix module schematic on Figure 6.1. Notice, when a channel is opened or closed, it means that it is disconnected or connected respectively.

A channel can be opened or closed by using the commands `:ROUT:MULT:OPEN(@142,119)` and `:ROUT:MULT:CLOS(@142,119)` respectively, where 142 and 119 are the channel numbers used in this example. The compiler writes a long machine command string of these consisting of all changes to the channels throughout the entirety of the measurement sequence. However, the compiler does not simply close or open all the channels at the same time. The order in which the channels are opened and closed, as the measurement changes from one to another configuration, will now be addressed. We will start by looking at the rules implemented for how the ground should be connected.

The first thing that needs to be connected to the sample is the ground. There should always be a ground connected to the sample at all times, in order to avoid unintentional built ups of charge in the sample. Therefore, all changes to the ground happens when all other channels are open. For each configuration that needs to be measured the compiler looks at the configuration array and does one of four things.

- If the configuration is the first in the entire measurement sequence it closes the ground channel.
- If the configuration is the last in the entire measurement sequence and all other channels are open, it opens the ground channel.
- If the configuration is followed by a configuration that shares the same ground electrode, it does nothing to the ground.
- If the configuration is followed by a configuration with a different ground electrode, it first closes for the new ground channel and then opens for the old ground channel.

After the ground channel is closed, all other relevant channels are closed except the source channel. Finally when they have been closed the source channel is closed and the measurement is performed. After a measurement the source channel is the first channel to be opened again. As an example the complete machine command string, for a measurement sequence consisting of only the A and B configuration for sub-probe 1234, will look like this:

```
:ROUT:OPEN:ALL                        opens all channels
:ROUT:MULT:OPEN(@148)                 filler string
:ROUT:MULT:CLOS(@136)                 ground close
:ROUT:MULT:CLOS(@142,119,108,150)     sense close
:ROUT:MULT:CLOS(@125)                 source close - measurement here
:ROUT:MULT:OPEN(@125)                 source open
:ROUT:MULT:OPEN(@142,119,108,150)     sense open
:ROUT:MULT:OPEN(@148)                 filler string
:ROUT:MULT:CLOS(@135)                 new ground close
:ROUT:MULT:OPEN(@136)                 old ground close
:ROUT:MULT:CLOS(@142,120,108,150)     sense close
:ROUT:MULT:CLOS(@125)                 source close - measurement here
:ROUT:MULT:OPEN(@125)                 source open
:ROUT:MULT:OPEN(@142,120,108,150)     sense open
:ROUT:MULT:OPEN(@135)                 ground open
:ROUT:OPEN:ALL                        opens all channels
```

On the right side of the code there is written some comments. These are not present in the real output, but have been added here for ease of reading. To keep all configuration segments the same length a filler line is added whenever the ground does not need to change, or it is the first configuration to be measured. This is done, so the program always have to get the same string length for all configurations.

6.2.2 Gate Sweeping

The other large change to the original program is the way measurements are done during a sweep of the gate voltage. In the original program, if a sweep of the gate voltage was wanted, it would first do the sweep for one configuration and would then do it for the next and so on. This works well for the large connections that it was designed for. However, with M4PP two measurements performed in the same engage, cannot necessarily be compared if measured too far apart temporally. Basically the longer one waits the large the chance that something happens that changes either the electrode position or the electrical contact in general. The new program was changed so that instead, all configurations would be measured before the gate voltage is changed.

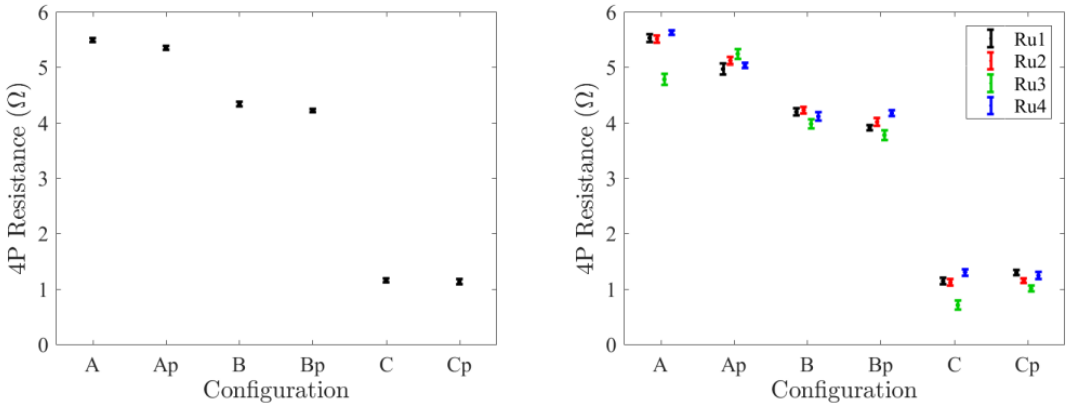

Figure 6.3: (Left) Plot of the mean four-point (4p) resistance, measured on the gold sample, as a function of configuration. (Right) Plot of the mean four-point (4p) resistance, measured on the ruthenium sample, as a function of configuration. The bars indicate one standard deviation.

6.3 Reference Measurements on Gold and Ruthenium

The system has undergone multiple iterations of improvements and changes. In the latest version reference measurements have been performed on gold and ruthenium samples. All the reference measurements were performed at a source voltage of 10mV resulting in a current around 5µA to 6µA. The voltage and current were chosen this low to emulate the conditions that will exist when measuring on MoS_2.

The calculated four-point resistances from the measurements are shown in Figure 6.3. The first two series of measurements on ruthenium (Ru1 and Ru2) were measured on the same day using the same sub-probe. The last two series of measurements on ruthenium (Ru3 and Ru4), were measured the day after Ru1 and Ru2, and with different sub-probes. All measurements on ruthenium were measured on the same sample, and all measurements within a measurement series were done in the same engage. Looking at the data it quickly becomes clear that the configuration pairs (i.e. R_i and R_{i_P}, where i is A, B or C) are not the same, and that the difference is largest for the A configurations (see section 2.1). Additionally, it is clear that the measurement, Ru3, behaves completely different to the other three measurement series on ruthenium. This odd man out could be caused by leak current running inside the sub-probe. Most of the difference seen between the other B and C configuration pair, cannot be distinguished from the measurement noise at a 95% confidence level. The differences for the A configuration pairs could be caused any number of systematic errors, from transient currents when switching configurations to a small leak inside the setup. However, the differences seen here are small enough that for the purposes of the setup this is more than precise enough.

Looking at the relation between the four-point resistance in the A configurations with those in the B and C configurations (see Figure 6.4 (left)), it again becomes very clear that something strange is going on with the measurement series Ru3. All the other measurements distribute nicely around 1, as they should, with an error of around 2%. On Figure 6.4 (right) the measured vdP corrected sheet resistance is shown for the different measurement series. Once again it is clear the the measurement series Ru3 is doing something completely different than expected based on the other measurements. The variance in the measured sheet resistance, from the other measurements on ruthenium, is considerably

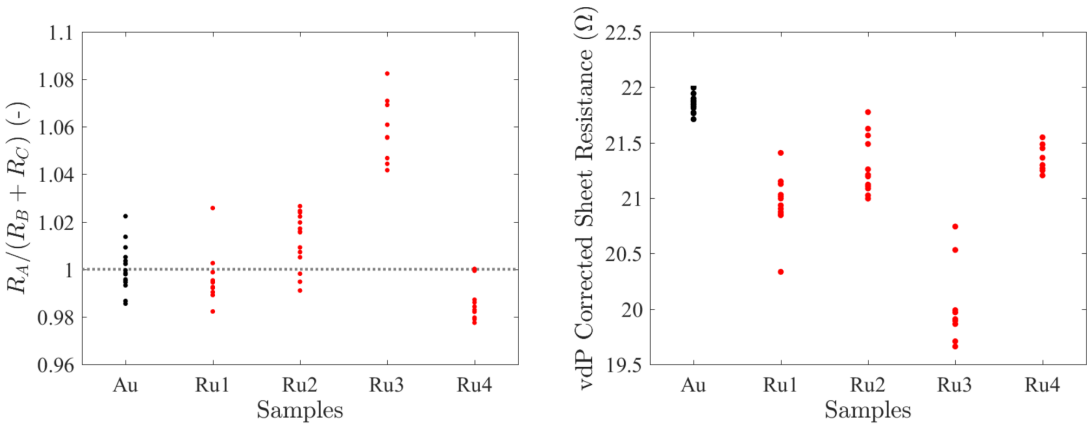

Figure 6.4: (Left) Plot of the relation $(R_A + R_{A_P})/(R_B + R_{B_P} + R_C + R_{C_P}$ for the different measurements series. (Right) The van der Pauw corrected sheet resistance calculated for the different measurement series.

larger than for the measurements on gold. The reason for this is not entirely clear.

All in all based on these measurements it is clear that there are certain systematic measurement errors present in the system. However, since the system is only expected to measure the source-drain current with a precision of 10%, a systematic error and measurement noise in the range of a few percent is not a problem.

6.4 Sample Damage During Probe Engage

When engaging with a probe on a sample there is a risk of damaging the sample. This would typically happen if the probe slides over the surface during engagement, and the sample is either softer or weaker than the probe. When measuring on materials that are only a single to a few atoms thick, the risk of sample damage is quite significant.

Four probe designs were used to engage on four MoS_2 samples. The used designs consisted of two straight designs and two L-shaped designs. Each of the pair consisted of a large probe (pitch of 10µm) and a small probe (varying pitch but smallest 1.5µm). Each design was engaged on two samples along with its size pair. The large probes were engaged 2µm. For standard sheet resistance measurements this would be quite excessive. However, from experience a deeper than normal engage is necessary, due to the difficulties in getting a good electrical contact to MoS_2. The small probes where engaged roughly 1µm. Each probe were engaged several times with a spacing of 5µm. This made it easier to find any damage to the sample afterwards, as it would appear as a dashed line more than 100µm long. Four of these lines can be seen in Figure 6.6 (top). The marks visible in the picture comes from the large (10µm pitch) straight probe engaging from the right and sliding to the left on the surface. The color channels, from a line across three marks made by the large straight probe, is shown in Figure 6.5. This plot shows that the marks are visible in the color channels as an increase in the red channel, but a dip in the green and blue channels. From this plot, it is also evident that the removed material have built up in the left most end of mark, appearing as a sharp dip in the green and blue channel. The best example of this is the third marker in Figure 6.5.

To increase the contrast in the picture for further analysis the green and blue channels were inverted and the red channel had its signal increased. The resulting picture is shown

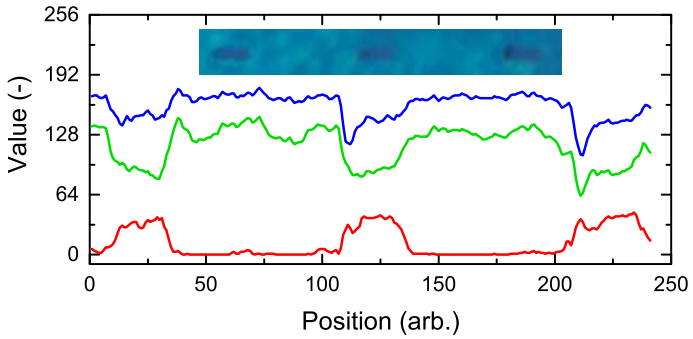

Figure 6.5: Plot of the three color channels from a line across three engage markers. The insert show the three markers used. The markers where made with the large straight probe (10µm pitch).

in Figure 6.6 (mid). The new color scale allows for an easier distinction of the engage markers, with a clear peak in gray-scale. The gray-scale value is shown in Figure 6.6 (bottom). Markers from all four straight cantilevers are visible in the micrograph of the straight cantilever while the corresponding micrographs from an L-shaped cantilever shows only the presence of marks from the strain gauge. The strain gauge is a large straight cantilever used to detect the surface of the sample. A comparison of the two large probe designs are shown in Appendix A.11.

In order to avoid damaging the sample, all measurements on MoS_2 will be done using L-shaped probes.

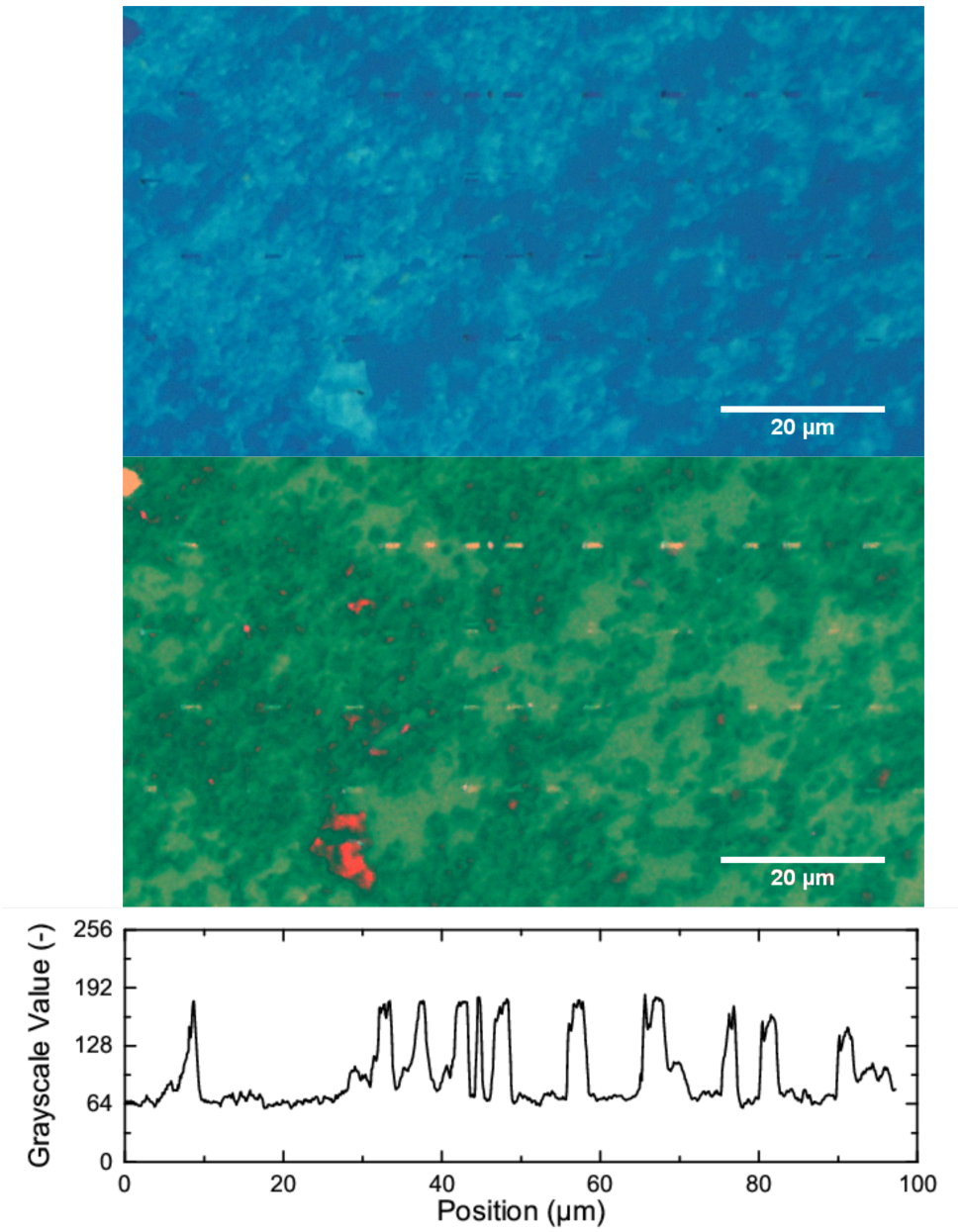

Figure 6.6: Top: Micrograph of MoS_2 sample after engaging a straight probe several times on the surface. The dark marks are areas where the probe has damaged the sample. These marks form four horizontal dashed lines. Mid: To enhance the contrast between the marks and the material, the green and blue channels have been inverted, and the signal of the red channel have been increased. Bottom: Line plot of the grayscale value of a line going through the top most of the four dashed lines form by the engagement marks. To make the grayscale value the picture with enhanced contrast (mid) have been used.

7 | Characterization of MoS_2

In this chapter measurements performed on MoS_2 will be presented. Samples were received from, the Technical Univeristy of Eindhoven, IMEC and DTU. The samples from both Eindhoven and IMEC were stored in a box with a nitrogen atmosphere, to avoid oxidation of the samples. Despite this, it was not possible to get any useful measurements on these samples. Of the samples from DTU, it was possible to measure on two of them. The first of which was measured at the start of the project (Sample A), while the other was measured towards the end of the project (Sample B). The second sample were an old sample that had been lying around in an office for at least two years.

7.1 The MoS_2 samples

The samples that were measured on, with success, in this project came from Tim Booth's group at DTU Nanotech (now DTU Physics) and were made by Abhay Shivayogimath. The process of which is described in his paper [41]. After synthesis of the material it is transfered to a silicon die, that consists of highly doped silicon with a 300nm layer of thermal oxide and then a lithographic gold structure on top. The structure is used to contact the MoS_2 using conventional macroscopic four-point measurement techniques. A sketch of how the sample is prepared is shown in Figure 7.1 (left) and a picture of a piece of MoS_2 is shown in Figure 7.1 (right).

Figure 7.1: (Left) Sketch of the process used to prepare the MoS_2 samples. (Right) microscope picture of a piece of MoS_2.

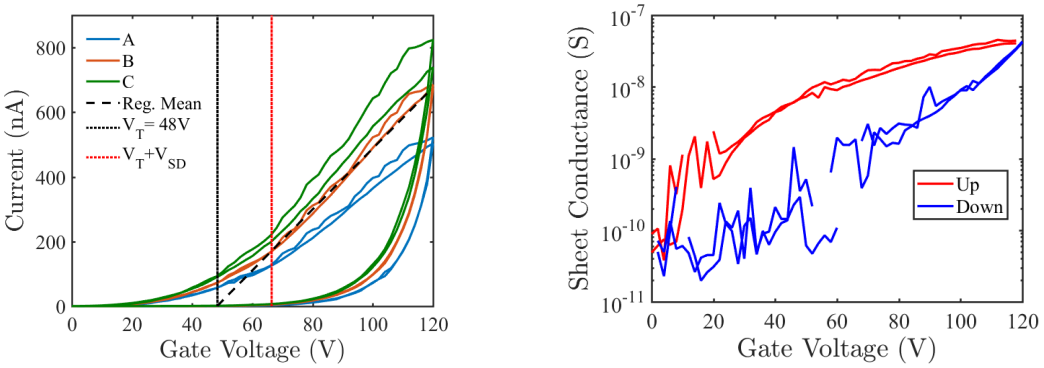

Figure 7.2: Measurement on Sample B. (Left) Plot of the supplied current as a function of the gate voltage, the source voltage was 18V. The black dotted line shows the threshold voltage calculated from the linear regime (see Equation (2.16)). The red line shows an approximation for the start of the linear regime. (Right) The sheet conductance as a function of the gate voltage in a semi-logarithmic plot.

7.2 The Measurements

Before each measurement series the probe and setup was tested by measuring on a small piece of conductive material, this was often either the gold leads on the sample itself or a piece of ITO. The goal of these measurements, was to test that all electrodes were working and to breakdown any native oxide that might have formed on the tip, analogous to a punch through (high transient current to create a good electrical contact [8]) in a regular M4PP measurement. In essence it was more important to pass a current than it was to get usable measurement. A high source current was used, that often caused the system to reach compliance.

Immediately after, measurements were performed by landing the M4PP on top of the MoS_2 and connecting the backside of the sample to a gate voltage. The connection to the gate was made by mounting the sample on a microscope slide using conductive graphite glue (see Figure A.2 for photo) and then connected to the sourcemeter using a wire.

Since all the regular electronics of the microRSP-M200 tool had been circumvented, access to the strain gauge on the M4PP was gone. This meant that all engages had to e made manually, using a microscope to see when the probe was engaged. Consequently the engagement depth could vary with around 500nm from engage to engage.

Current-Voltage curve and Threshold Voltage

An example of the I-V_G curve for a field effect measurement on MoS_2 is shown in Figure 7.2 (Left). On this plot the measured current in the A, B and C configurations for an applied potential of 18V is shown along with the extrapolated threshold voltage. The threshold voltage was found using the method for the linear regime (see Equation (2.16)). The plot shows two repeats of the same measurement, sweeping the gate voltage from 60V to 0V, up to 120V, back to 60V and then repeat the sweep. The current seem to rise linearly from about 68V up to 120V. While there are discrepancies between the repeats they are largely overlapping their previous run. The largest difference between runs are for the C-configuration and is 11.5%. There is also a clear hysteresis in the measurement, with the current being lower when the gate is swept down. Most likely this hysteresis is

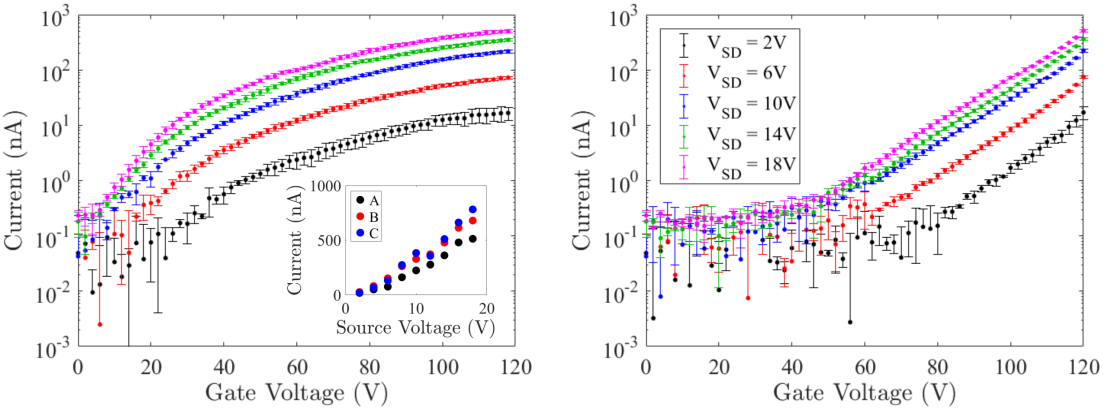

Figure 7.3: Measurement on Sample B. Plot of the supplied current for the A configuration as a function of gate voltage in a semilogarithmic plot. Each color corresponds to a different source potential. Each point is an average over two sweeps with two measurement points at each gate voltage. Legend for the sweeps only shown in right figure. (Left) Only the sweep up has been included. In the insert the current at $V_G = 120\,V$ is shown as a function of the source potential. (Right) Only the sweep down has been included.

caused by moisture trapped in the sample [62, 63].

The sheet conductance for the same measurement is shown in Figure 7.2 (right). This measurement looks quite noisy, which makes sense, considering the noise on the current measurements. It is still possible to see, that the ratio between the conductance in the on and off state, is around three orders of magnitude.

While it looks like the measurement shown in Figure 7.2 (Left) was done in the linear regime, it makes sense to check if that is actually the case. On the same sample the the supplied current was measured as a function of the gate voltage for different source potentials. By doing this it is possible to check if the material is truly operated in the linear regime. Semilogarithmic plots of the supplied current are shown in Figure 7.3. The left plot shows the current when the gate voltage is swept up, and on the right plot the current is shown when the gate voltage is swept down. In both cases each point is the mean taken over two sweeps of the gate voltage, where each measurement point was repeated twice.

On the plot for the sweep up (left), it seems that the vertical distance on the plot between any two curves is constant for all values of the gate voltage. On a semilogarithmic plot that translates into the same factor is needed to go from one curve to another. Or put another way, the influence of the source potential is independent on the gate voltage.

As an insert in the left plot, the supplied current at $V_G = 120$V is shown as a function of the source voltage. From this plot it can be concluded that the current is increasing linearly with the source voltage, i.e. the measurement was performed in the linear regime.

On the plot for the sweep down (Figure 7.3 (right)), five straight lines are shown going from 120V to ∼60V. From this it can be concluded that the current during the down sweep is exponentially decreasing. Looking at the downwards sweep of a measurement done on a different sample at a different rate (Figure 7.4), it turns out that this downwards sweep is also described by an exponential function. More surprising is that the rate in both exponential functions is 0.085V^{-1}. From this it may be inferred that the decay is not caused by a time depend process. Although the value is the same for two different

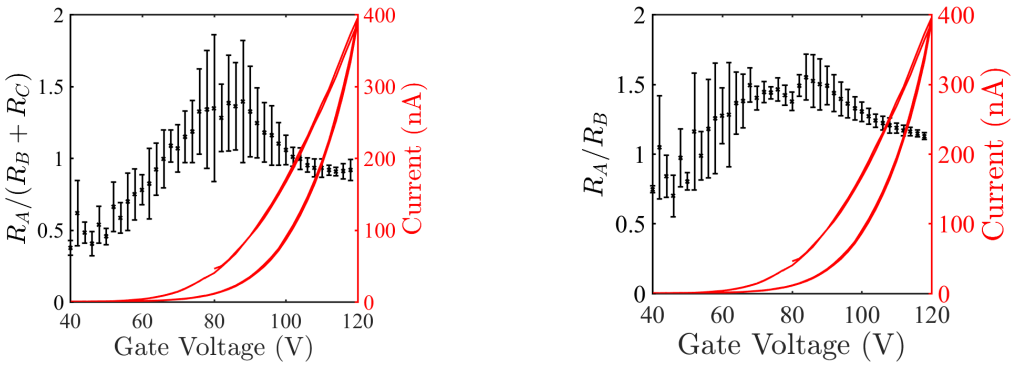

Figure 7.4: Measurement on Sample A. Field effect measurements on a piece of MoS_2. Measurements performed at an applied potential of 10V. (Left) $R_A/(R_B+R_C)$ relation as a function of gate voltage. (Right) plot of the R_A/R_B relation as a function of the gate voltage. Over both plots is the I-V_G curve for the A configuration.

samples (measured years apart), it seems unlikely that a material with so high variance for other parameters should give the precise same rate by themselves. It seems more likely that this is combination of some natural constants, that I am unaware of.

The relative measurement error of measurements shown in Figure 7.3, decreases to 10% or lower with gate voltages over 60V, for all source voltages except 2V. All the measurements in Figure 7.3 were performed within a single engagement across four hours. Each sweep taking 15 minutes to complete. Note that B and C configurations were also measured along with sweeps using a source voltage of 4, 8, 12 and 16V.

Resistance Relations and Current Flow

Taking the relation between the the resistances for the A configuration and the sum of the resistances for the B and C configuration, the result according to theory should give 1 (see Section 2.1). On Figure 7.4 (Left) this is shown for a measurement on sample A of MoS_2. The measurement was performed at a source voltage of 10V. For low gate voltages the MoS_2 is in the off-state and we are basically attempting to measure an insulator. Logically the ratio will differ from unity. At a gate voltage of around 70V to 90V the MoS_2 is transitioning between the off and on state. However, the measured current is still very low, at around 50nA, and the ratio is dominated by noise. Finally as the current increases and the signal, to noise ratio improves the $R_A/(R_B+R_C)$ tends towards 1 as expected.

As discussed in M. R. Lotz paper [64] the ratio R_A/R_B is dependent on the dimensionality of the current transport. Such that a ratio of $\ln(4)/\ln(3) \approx 1.262$ is indicative of a two dimensional transport in the material, i.e. the material is continuous. However, a ratio of 1 indicates a one dimensional current transport, e.g. current runs along boundary edges. The R_A/R_B ratio is plotted for a MoS_2 measurement in Figure 7.4 (Right). Like for the $R_A/(R_B+R_C)$ low and medium gate voltages is of little interest since the error is to large for any conclusions. At the high gate voltages the R_A/R_B seems to go from roughly 1.2 to 1.1 as the gate voltage increases. This might suggest that as the Fermi Energy for the MoS_2-flake is increased, the boundaries between crystals become more and more dominant.

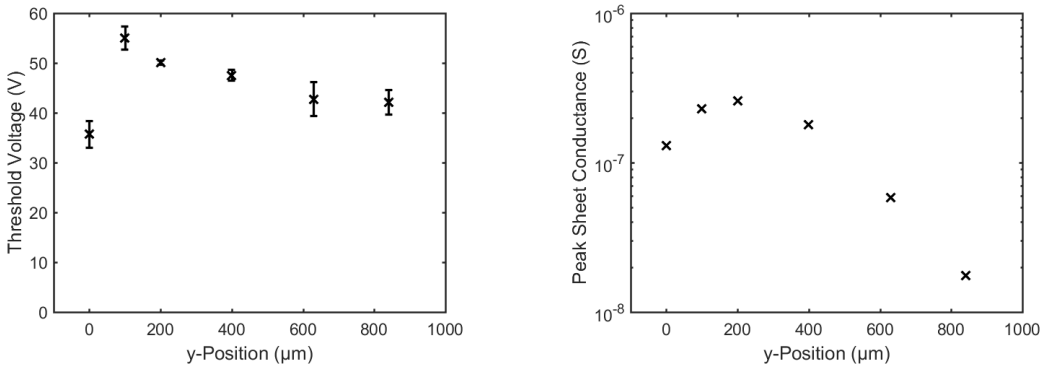

Figure 7.5: Measurement on Sample B. Line scan on a piece of MoS_2 using M4PP. (Left) Threshold voltage as a function of position on sample. (Right) Sheet conductance as a function of position on the sample.

Line Scan

As a proof of concept a line scan across a MoS_2 sample was performed consisting of seven points (eight if you include the point that landed in a hole in the sample). The measurements were done by landing on the sample and performing a gate sweep. After the sweep was done the probe was disengaged and moved to the next point. The line scan was started a couple of electrode pitches away from the edge. Far enough that the edge of the sample should not affect the measurement directly [65]. And, then proceeded to move across the center of the sample. Figure 7.5 shows the linear threshold voltage (left) and the highest measured sheet conductance (right). The threshold voltage has a jump at the beginning of the scan, but seems to gradually decrease along the scan from there. The sheet conductance on the other hand increased until about 200µm into the line scan, after which it decreases.

Without a proper test of the engage to engage precision it is impossible to conclude whether or not this is caused by sample variations or engage dependent measurement errors.

Field Effect Mobility

The field effect mobility was measured for an MoS_2 sample. The results from this measurement is shown in Figure 7.6. The measured field effect mobility is rather low compared to what was documented [41] for similar samples. Which had a mobility between 5 and 30 $cm^2/V/s$. However, those measurements were performed when the material was new. When the measurements shown here were performed the sample was already nearing three years old. It is quite likely that a MoS_2 sample stored in ambient conditions, would deteriorate in that time span. The measured field effect mobility is roughly two orders of magnitude lower than what was hoped for.

7.3 Common Problems During Measurements

In this section a list of some of the most common problems, that were experienced during measurements, is presented. The solutions or attempts there at, is also presented for each

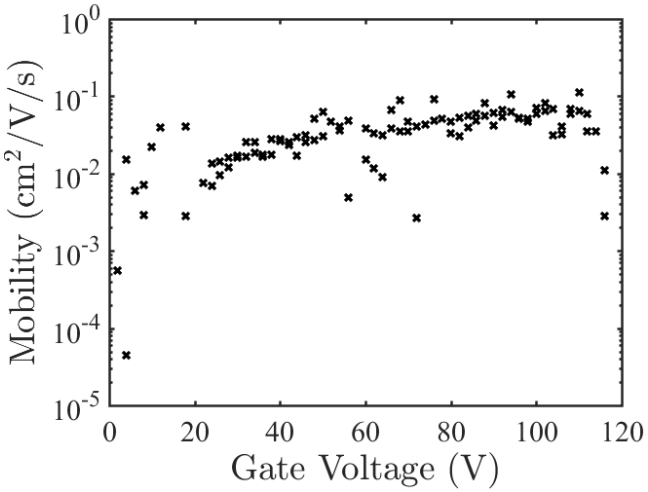

Figure 7.6: Measurement on Sample B. Plot of the field effect mobility in the linear regime, calculated using the van der Pauw corrected sheet resistance [41].

problem.

One or more dead electrodes

In the first few iterations of the setup, there were problems with electrodes not working either immediately or shortly after beginning to measure. Because of other problems at this stage it took awhile to realize that the electrodes in question was those used as ground. At this point the setup simply closed all channels for a measurement at the same time. Additionally, all switching between configurations were hot switching i.e. switching an array while the current is running. Most likely this caused a built up of charges between measurements and a rapid discharge. This transient current might very well have burned out the ground electrodes. To prevent this, the new opening and closing sequence seen in Section 6.2.1 was implemented. In this sequence it was ensured that there was always a ground electrode connected to the sample at all times. In the same series of updates to the software hot switching was replaced with cold switching. This was done for longer durability of the setup, as well as avoiding built-ups of charge during switching.

After the implementation of the new measurement sequence the number of dead electrodes became effectively zero. Note that this does not mean that all electrodes necessarily works for all engages. Just that no electrodes were permanently damaged.

Bad electrical contact to the sample

A bad electrical contact with a M4PP is something that can happen on all samples, even with a regular M4PP setup. Samples with higher resistivity being more difficult to contact. In a traditional M4PP setup this is typically mitigated by doing a punch through (as mentioned earlier). However, with measurements on MoS_2 it is not feasible. This can be realized by looking the two-point resistance measured at the start of the sweeps ($V_G = 80$V for sample A and $V_G = 60$V for sample B) shown in this chapter. The resistances are roughly $2 \times 10^8 \Omega$ in both cases. A typical punch through current is between 25µA and 100µA [8]. This means that in order to make a punch through the potential on

the electrodes has to be allowed to reach 5 to 20kV. Besides being more than the chosen sourcemeter can deliver, it would also cause a complete breakdown of the insulating layers in the probe as well as the BOX of the sample. In short, it cannot be done with the equipment and even if it could, it should not be done.

Since punch through is not possible directly on the sample, measurements on a conductive material was done before each measurement session. On a conductive material such as gold or ruthenium a punch-through like measurement is possible. With a two-point resistance in the hundreds of ohms instead of hundreds of megaohm, the potential only needs to be able to reach about 0.01 to 0.1V. Doing this has half of the benefit normally associated with a punch-through. It will breakdown any oxides on the cantilever that prevents a good electrical contact, but unlike a real punch-through it will not create a weak "welding" of the electrodes to the sample that needs to be measured (It will most likely create one with the conductive sample though). To facilitate these pseudo punch-throughs a mode for doing a non gate sweep measurement with a current source was implemented.

Implementing the use of a short measurement on conductive materials before real measurements, significantly improved the chance of getting a good contact. From roughly fifty-fifty to almost all having a good contact.

Leakage current running between source/drain and gate

For some samples a large leakage current was measured between either the source or drain and the gate terminal. The leakage was independent on the probes used, seemingly only dependent on the sample. Based on this the samples were deemed defective.

The problem seemed unrelated to the setup and caused by a short inside the sample.

Contracting or expanding conductive glue

The problem here is quite simple and easily fixable, but something that one needs to be aware of nonetheless. When adding an electrical contact to the backside of the sample using conductive glue. It is important to ensure that the glue is completely cured. Otherwise the sample may move during measurements. If a silicon die is glued to something impermeable such as a glass microscope slide (as used in this thesis). It takes a surprisingly long time for the glue to cure at the center of the silicon die. The glue used in this thesis, would cure at the edge of the silicon die within a minute, but sometimes would still be uncured at the center after several hours.

The solution to this problem is simply to wait for a couple of hours, until the glue is either completely cured, or cured to the point were it wont change on the timescale of an hour, before measuring. Alternatively, the sample can be baked to speed up the curing process.

7.4 Conclusion to MoS_2 measurements

In this thesis it have been shown that it is possible to perform field effect measurements on MoS_2 using M4PP. From these measurements it has been possible to determine the threshold voltage and field effect mobility of the material. The method has reached a point, that with a good sample, most engages will have a useful two point measurement, and

many will also have useful four point measurements. This is a considerable improvement to the first iteration of the setup.

Due to the scarcity of good samples, it has not been possible to perform reproducibility studies, finding the engage to engage error. Additionally, while it is possible to look at the good measurements and calculate the variance of same engage measurements. It is hard to determine the sources of said variance.

8 | Conclusion and Outlook

8.1 Outlook: Field Effect Measurements with M4PP

The thesis has presented proof of concept measurements on MoS_2 using a Ψ-MOSFET like technique involving M4PP. The next step for this type of measurements is to do a more vigorous reproducibility study, that really tests the technique and maps out the errors and determines its precision, and if possible accuracy. This would naturally require samples that are more consistent in their electrical properties, as well as samples with special geometries.

The easiest way to do a reproducibility study, would be to make a ribbon of MoS_2 with two lithographic contacts at each end. In theory this would allow for a comparison between the measurements done using the lithographic contacts and a linescan along the ribbon done with the M4PP. The measurements from the M4PP gives a more detailed picture of the sheet resistances inside the ribbon, that should average to what was measured across the entire ribbon with the lithographic contacts. A sketch of the setup is shown in Figure 8.1. It is known from a previous study [15], that a sheet resistance on a ribbon will be sensitive to the materials roughly one electrode pitch away. By measuring only one electrode away from the last measurement, in the reproducibility study, the measurements of two neighbor engages will be correlated, thereby allowing for an extra sanity check, since every measurement should be explainable by its immediate neighbors.

A different route, could be to attempt to measure on fully depleted SOI wafers. These samples have notoriously low conductance, making it impossible to measure on them with regular M4PP techniques. The normal measurement technique for characterizing these samples is the Ψ-MOSFET technique, using large probes that are pressed very hard into

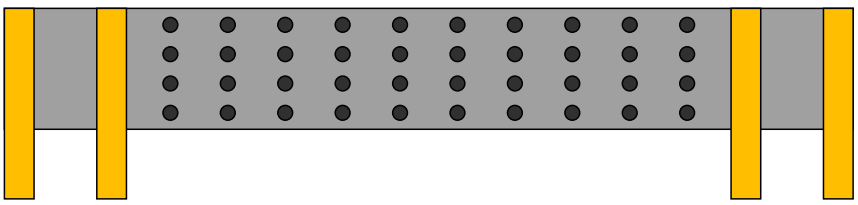

Figure 8.1: Sketch of a possible reproducibility study using a combination of lithographic contacts and M4PP measurements. The gray area is the MoS_2. Normal four point measurements are performed using the yellow contacts. The black dots indicates M4PP measurements along the the MoS_2 ribbon.

the surface. Similar to this technique, the method presented in this thesis, are based around the use of an electrical field to induce carriers in the sample. It stands to reason that this might allow for M4PP field effect measurements on fully depleted SOI. A very exciting possibility if doable.

8.2 Outlook: Design Optimization of Micro Electrodes

The study of cantilevers consisting of two beams connected at an arbitrary angle is at this point almost done. Besides looking at describing completely different designs of cantilevers, it would be interesting to study the cantilever tips path across the surface during an engage. This might ultimately help better understand and minimize off-line positioning errors.

8.3 Conclusion

The overarching goal of the thesis was to develop a theoretical framework for making new cantilever designs, as well as to build a measurement setup capable of doing field effect measurements on MoS_2 and test it.

As a part of the goal, to make a framework for designing new cantilevers in the future, an analytical expression for the compliance tensor of a cantilever with a arbitrary two beam design was introduced and compared with previous known solutions. To do this a "new" parameter η was introduced, describing the angle between the first and second beam. With $\eta = 0°$ being them forming a straight cantilever and $\eta = 90°$ being them forming an L-shaped cantilever. In this derivation both elongation and deflection was taken into account, making it precise at both low and high angles of η. With the solution being identical to straight and L-shaped cantilever at $\eta = 0°$ and $\eta = 90°$ respectively.

Numerical work, using finite element modeling, was done, that showed that a disagreement between the analytical model and numeric calculation was less than 5% for the engage stiffness and typically around 4% for the vibration tolerance, unless the vibration tolerance was very low. This disagreement contains both errors in the analytical expression, since certain simplifications was made in the calculations. But, also numerical errors in the finite element model. These could come from the chosen mesh, or the model geometry used for the cantilever. All in all, a 5% error is less than what can be expected from the uncertainty in the fabrication process.

Cantilever where also printed in a scale of 1:10000 in the material PLA [57]. When measuring the contact force as a function of engage depth excellent agreement with theory was observed. Where the compliance element C_{zz} and K_{zz} was recreated with a high level of precision. This confirmed the validity of both the stipulated contact models, but also the expression for the compliance tensor presented derived as part of this project.

In addition to the new compliance tensor, an expression for the vibration tolerance was also formalized. The vibration tolerance was defined as the minimum vibration, measured in units of the engagement depth, needed to make a cantilever slide on the surface. This expression was then tested against an experiment were two probes were used to measure the sheet resistance of either ITO or silicon, during which the vibrations were increased. When a measurement had failed five times in a row, it was deemed to have moved because of the vibrations [26].

By combining the new expression for the compliance tensor with the expression for the vibration tolerance, a cantilever used in a previous publication [14], was optimized in two ways. The first optimization was based on the desire to keep a constant electrode pitch, CD and engage stiffness, but still improving the vibration tolerance of cantilever. The optimization changed the height and lengths of the beams and the angle of the second beam. The new cantilever design saw an improvement of the vibration tolerance form 1.6% to 4.8% corresponding to a tripling. The second optimization was focused on changing the design to achieve an electrode pitch of 1.1µm without changing the CD. This optimization used that for any choice of widths, the vibration tolerance is always biggest at the highest possible angles. This way the optimization was run first over the width and height, and then over the lengths. The resulting designed had an electrode pitch of 1.1µm, while keeping the engage stiffness and increasing the vibration tolerance from 1.6% to 3.8%, or by a factor of 2.5. In short, a tool that can be used for designing new cantilevers have been presented and used to improve an existing design, to achieve markedly higher vibration tolerances.

The other part of the goal was to design and test a measurement setup that can be used to characterize TMDs. The setup was based on an existing setup at DTU Nanotech, combined with a semiautomatic microRSP-M200 tool at CAPRES. Changes were made to the facilitate the complete use of the M7PP, and to interface the new measurement equipment with the M200. To utilize the M7PP a complete rework of the multiplexing system was necessary. The new setup has since it initial creation undergone several updates and tweaks, improving the measurement sequence. The setup was tested by measuring on a gold film and a ruthenium covered silicon sample. Despite some irregularities in the magnitude of the A-configurations, the error was deemed low enough, not to be worth investigating, for now.

Doing M4PP based field effect measurements on materials with sheet resistances in the 10MΩ regime, is already extremely difficult. Due to it being hard to make a good electrical contact. In addition to this, there were only two samples throughout the course of the project, that was of a high enough electrical quality that they could be somewhat reliably contacted with a M4PP. Unfortunately that meant it was difficult to make the reproducibility studies necessary to find the precision of the system. On a positive note, the two samples that worked with the M4PP allowed for some nice proof of concept measurements, showing that it is possible to measure on these materials. And, that from these measurements the sheet resistance, threshold voltage, field effect mobility and the R_A/R_B relation can be calculated. The repeatability on the measured current within one measurement sequence was found to be around 10% or better. Thereby partially achieving the goal of a precision of around 10%, since the engage to engage precision is still unknown.

Bibliography

[1] G. E. Moore. Cramming more components onto integrated circuits, reprinted from electronics, volume 38, number 8, april 19, 1965, pp.114 ff. *IEEE Solid-State Circuits Society Newsletter*, 11(3):33–35, Sep. 2006.

[2] Mark L. Schattenburg and Henry I. Smith. The critical role of metrology in nanotechnology. In Martin C. Peckerar and Michael T. Postek Jr., editors, *Nanostructure Science, Metrology, and Technology*, volume 4608, pages 116 – 124. International Society for Optics and Photonics, SPIE, 2002.

[3] I Miccoli, F Edler, H Pfnür, and C Tegenkamp. The 100th anniversary of the four-point probe technique: the role of probe geometries in isotropic and anisotropic systems. *Journal of Physics: Condensed Matter*, 27(22):223201, may 2015.

[4] F. M. Smits. Measurement of sheet resistivities with the four-point probe. *The Bell System Technical Journal*, 37(3):711–718, May 1958.

[5] C. L. Petersen, F. Grey, I. Shiraki, and S. Hasegawa. Microfour-point probe for studying electronic transport through surface states. *Applied Physics Letters*, 77(23):3782–3784, 2000.

[6] C.L Petersen, T.M Hansen, P Bøggild, A Boisen, O Hansen, T Hassenkam, and F Grey. Scanning microscopic four-point conductivity probes. *Sensors and Actuators A: Physical*, 96(1):53 – 58, 2002.

[7] Trudo Clarysse, A. Moussa, Frederik Leys, Roger Loo, Wilfried Vandervorst, M. C. Benjamin, Robert J. Hillard, Vladimir Faifer, Michael I. Current, Rong Lin, and Dirch Hjorth Petersen. Accurate sheet resistance measurement on ultra-shallow profiles. 2006.

[8] Steven Folkersma, Janusz Bogdanowicz, Andreas Schulze, Paola Favia, Dirch H. Petersen, Ole Hansen, Henrik H. Henrichsen, Peter F. Nielsen, Lior Shiv, and Wilfried Vandervorst. Electrical characterization of single nanometer-wide si fins in dense arrays. *Beilstein Journal of Nanotechnology*, 9:1863–1867, 2018.

[9] J K Kim, Y S Choi, and D W Lee. Surface-adaptable all-metal micro-four-point probe with unique configuration. *Journal of Micromechanics and Microengineering*, 25(7):075023, jun 2015.

[10] S. Keller, S. Mouaziz, G. Boero, and J. Brugger. Microscopic four-point probe based on su-8 cantilevers. *Review of Scientific Instruments*, 76(12):125102, 2005.

[11] D Kjær, L Gammelgaard, P Bøggild, O Hansen, P R E Petersen, and J E Hansen. Flexible SiO2 cantilevers for torsional self-aligning micro scale four-point probes. *Journal of Micromechanics and Microengineering*, 17(9):1910–1915, aug 2007.

[12] Snorre B Kjeldby, Otto M Evenstad, Simon P Cooil, and Justin W Wells. Probing dimensionality using a simplified 4-probe method. *Journal of Physics: Condensed Matter*, 29(39):394008, aug 2017.

[13] Dirch H. Petersen, Ole Hansen, Rong Lin, and Peter F. Nielsen. Micro-four-point probe hall effect measurement method. *Journal of Applied Physics*, 104(1):013710, 2008.

[14] Alberto Cagliani, Frederik W. Østerberg, Ole Hansen, Lior Shiv, Peter F. Nielsen, and Dirch H. Petersen. Breakthrough in current-in-plane tunneling measurement precision by application of multi-variable fitting algorithm. *Review of Scientific Instruments*, 88(9):095005, 2017.

[15] Dirch H. Petersen, Ole Hansen, Torben M. Hansen, Peter Bøggild, Rong Lin, Daniel Kjær, Peter F. Nielsen, Trudo Clarysse, Wilfried Vandervorst, Erik Rosseel, Nick S. Bennett, and Nick E. B. Cowern. Review of electrical characterization of ultra-shallow junctions with micro four-point probes. *Journal of Vacuum Science & Technology B*, 28(1):C1C27–C1C33, 2010.

[16] T. Clarysse, J. Bogdanowicz, J. Goossens, A. Moussa, E. Rosseel, W. Vandervorst, D.H. Petersen, R. Lin, P.F. Nielsen, Ole Hansen, G. Merklin, N.S. Bennett, and N.E.B. Cowern. On the analysis of the activation mechanisms of sub-melt laser anneals. *Materials Science and Engineering: B*, 154-155:24 – 30, 2008. Front-End Junction and Contact Formation in Future Silicon/Germanium Based Devices.

[17] Frederik Westergaard Østerberg, Maria-Louise Witthøft, Shibesh Dutta, Johan Meersschaut, Christoph Adelmann, Peter Folmer Nielsen, Ole Hansen, and Dirch Hjorth Petersen. Hall effect measurement for precise sheet resistance and thickness evaluation of ruthenium thin films using non-equidistant four-point probes. *AIP Advances*, 8(5):055206, 2018.

[18] Sune Thorsteinsson, Fei Wang, Dirch H. Petersen, Torben Mikael Hansen, Daniel Kjær, Rong Lin, Jang-Yong Kim, Peter F. Nielsen, and Ole Hansen. Accurate microfour-point probe sheet resistance measurements on small samples. *Review of Scientific Instruments*, 80(5):053902, 2009.

[19] D. C. Worledge and P. L. Trouilloud. Magnetoresistance measurement of unpatterned magnetic tunnel junction wafers by current-in-plane tunneling. *Applied Physics Letters*, 83(1):84–86, 2003.

[20] Maria-Louise Witthøft, Frederik W. Østerberg, Janusz Bogdanowicz, Rong Lin, Henrik H. Henrichsen, Ole Hansen, and Dirch H. Petersen. A variable probe pitch microhall effect method. *Beilstein Journal of Nanotechnology*, 9:2032–2039, 2018.

[21] Daniel Kjaer, Ole Hansen, Frederik Westergaard Østerberg, Henrik Hartmann Henrichsen, Christian Markvardsen, Peter Folmer Nielsen, and Dirch Hjorth Petersen. Characterization of positional errors and their influence on micro four-point probe measurements on a 100 nm ru film. *Measurement Science and Technology*, 26(9):095005, jul 2015.

[22] D. C. Worledge. Reduction of positional errors in a four-point probe resistance measurement. *Applied Physics Letters*, 84(10):1695–1697, 2004.

[23] Dirch H. Petersen, Ole Hansen, Torben M. Hansen, Peter R.E. Petersen, and Peter Bøggild. Static contact micro four-point probes with <11nm positioning repeatability. *Microelectronic Engineering*, 85(5):1092 – 1095, 2008. Proceedings of the Micro- and Nano-Engineering 2007 Conference.

[24] Fei Wang, Dirch H Petersen, Helle V Jensen, Christian Hansen, Dennis Mortensen, Lars Friis, and Ole Hansen. Three-way flexible cantilever probes for static contact. *Journal of Micromechanics and Microengineering*, 21(8):085003, jun 2011.

[25] Dirch Hjorth Petersen. *Micro Four-Point Probe and Micro Hall Effect: Methods for Reliable Electrical Characterization of Ultra-Shallow Junctions*. PhD thesis, 2009.

[26] Kristoffer G Kalhauge, Henrik H Henrichsen, Fei Wang, Ole Hansen, and Dirch H Petersen. Vibration tolerance of micro-electrodes. *Journal of Micromechanics and Microengineering*, 28(9):095010, jun 2018.

[27] P. R. Wallace. The band theory of graphite. *Phys. Rev.*, 71:622–634, May 1947.

[28] K. S. Novoselov, A. K. Geim, S. V. Morozov, D. Jiang, Y. Zhang, S. V. Dubonos, I. V. Grigorieva, and A. A. Firsov. Electric field effect in atomically thin carbon films. *Science*, 306(5696):666–669, 2004.

[29] K. S. Novoselov, D. Jiang, F. Schedin, T. J. Booth, V. V. Khotkevich, S. V. Morozov, and A. K. Geim. Two-dimensional atomic crystals. *Proceedings of the National Academy of Sciences*, 102(30):10451–10453, 2005.

[30] Sheneve Z. Butler, Shawna M. Hollen, Linyou Cao, Yi Cui, Jay A. Gupta, Humberto R. Gutiérrez, Tony F. Heinz, Seung Sae Hong, Jiaxing Huang, Ariel F. Ismach, Ezekiel Johnston-Halperin, Masaru Kuno, Vladimir V. Plashnitsa, Richard D. Robinson, Rodney S. Ruoff, Sayeef Salahuddin, Jie Shan, Li Shi, Michael G. Spencer, Mauricio Terrones, Wolfgang Windl, and Joshua E. Goldberger. Progress, challenges, and opportunities in two-dimensional materials beyond graphene. *ACS Nano*, 7(4):2898–2926, 2013. PMID: 23464873.

[31] Deep Jariwala, Vinod K. Sangwan, Lincoln J. Lauhon, Tobin J. Marks, and Mark C. Hersam. Emerging device applications for semiconducting two-dimensional transition metal dichalcogenides. *ACS Nano*, 8(2):1102–1120, 2014. PMID: 24476095.

[32] Wonbong Choi, Nitin Choudhary, Gang Hee Han, Juhong Park, Deji Akinwande, and Young Hee Lee. Recent development of two-dimensional transition metal dichalcogenides and their applications. *Materials Today*, 20(3):116 – 130, 2017.

[33] Nanjundan Ashok Kumar, Mushtaq Ahmad Dar, Rukhsana Gul, and Jong-Beom Baek. Graphene and molybdenum disulfide hybrids: synthesis and applications. *Materials Today*, 18(5):286 – 298, 2015.

[34] Xiao Huang, Zhiyuan Zeng, and Hua Zhang. Metal dichalcogenide nanosheets: preparation, properties and applications. *Chem. Soc. Rev.*, 42:1934–1946, 2013.

[35] B. Radisavljevic, A. Radenovic, J. Brivio, V. Giacometti, and A. Kis. Single-layer mos2 transistors. *Nature Nanotechnology*, 6(3):147–150, 2011.

[36] Shisheng Lin, Xiaoqiang Li, Peng Wang, Zhijuan Xu, Shengjiao Zhang, Huikai Zhong, Zhiqian Wu, Wenli Xu, and Hongsheng Chen. Interface designed mos2/gaas heterostructure solar cell with sandwich stacked hexagonal boron nitride. *Scientific Reports*, 5:15103 EP –, Oct 2015. Article.

[37] Wenzhuo Wu, Lei Wang, Yilei Li, Fan Zhang, Long Lin, Simiao Niu, Daniel Chenet, Xian Zhang, Yufeng Hao, Tony F. Heinz, James Hone, and Zhong Lin Wang. Piezoelectricity of single-atomic-layer mos2 for energy conversion and piezotronics. *Nature*, 514:470 EP –, Oct 2014.

[38] Nitin Choudhary, Mumukshu Patel, Yee-Hsien Ho, Narendra B. Dahotre, Wonki Lee, Jun Yeon Hwang, and Wonbong Choi. Directly deposited mos2 thin film electrodes for high performance supercapacitors. *J. Mater. Chem. A*, 3:24049–24054, 2015.

[39] Gwan-Hyoung Lee, Young-Jun Yu, Xu Cui, Nicholas Petrone, Chul-Ho Lee, Min Sup Choi, Dae-Yeong Lee, Changgu Lee, Won Jong Yoo, Kenji Watanabe, Takashi Taniguchi, Colin Nuckolls, Philip Kim, and James Hone. Flexible and transparent mos2 field-effect transistors on hexagonal boron nitride-graphene heterostructures. *ACS Nano*, 7(9):7931–7936, 2013. PMID: 23924287.

[40] Deblina Sarkar, Wei Liu, Xuejun Xie, Aaron C. Anselmo, Samir Mitragotri, and Kaustav Banerjee. Mos2 field-effect transistor for next-generation label-free biosensors. *ACS Nano*, 8(4):3992–4003, 2014. PMID: 24588742.

[41] Abhay Shivayogimath, Joachim Dahl Thomsen, David M. A. Mackenzie, Mathias Geisler, Raluca-Maria Stan, Ann Julie Holt, Marco Bianchi, Andrea Crovetto, Patrick R. Whelan, Alexandra Carvalho, Antonio H. Castro Neto, Philip Hofmann, Nicolas Stenger, Peter Bøggild, and Timothy J. Booth. A universal approach for the synthesis of two-dimensional binary compounds. *Nature Communications*, 10(1):2957, 2019.

[42] Yumeng Shi, Henan Li, and Lain-Jong Li. Recent advances in controlled synthesis of two-dimensional transition metal dichalcogenides via vapour deposition techniques. *Chem. Soc. Rev.*, 44:2744–2756, 2015.

[43] Dominik Lembke, Simone Bertolazzi, and Andras Kis. Single-layer mos2 electronics. *Accounts of Chemical Research*, 48(1):100–110, 2015. PMID: 25555202.

[44] S. Cristoloveanu and S. Williams. Point-contact pseudo-mosfet for in-situ characterization of as-grown silicon-on-insulator wafers. *IEEE Electron Device Letters*, 13(2):102–104, Feb 1992.

[45] Sorin Cristoloveanu, Maryline Bawedin, and Irina Ionica. A review of electrical characterization techniques for ultrathin fdsoi materials and devices. *Solid-State Electronics*, 117:10 – 36, 2016. PLANAR FULLY-DEPLETED SOI TECHNOLOGY.

[46] K. Komiya, N. Bresson, S. Sato, S. Cristoloveanu, and Y. Omura. Detailed investigation of geometrical factor for pseudo-mos transistor technique. In *2004 IEEE International SOI Conference (IEEE Cat. No.04CH37573)*, pages 75–76, Oct 2004.

[47] S. Cristoloveanu, D. Munteanu, and M. S. T. Liu. A review of the pseudo-mos transistor in soi wafers: operation, parameter extraction, and applications. *IEEE Transactions on Electron Devices*, 47(5):1018–1027, May 2000.

[48] ICCT. European vehicle market statistics - pocketbook 2018/19. `https://theicct.org/sites/default/files/publications/ICCT_Pocketbook_2018_Final_20181205.pdf`, 10 2019.

[49] R Rymaszewski. Relationship between the correction factor of the four-point probe value and the selection of potential and current electrodes. *Journal of Physics E: Scientific Instruments*, 2(2):170–174, feb 1969.

[50] E. D. Jones. *Control of Semiconductor Conductivity by Doping*, pages 155–171. Springer US, Boston, MA, 1991.

[51] Alain C. Diebold. *Handbook of Silicon Semiconductor Metrology*. Marcel Dekker, New York, NY, 1 edition, 2001.

[52] Michael Shur. *Physics of Semiconductor Devices*. Prentice Hall, Eaglewood Cliffs, N.J., 1 edition, 1990.

[53] Stephen D. Senturia. *Microsystem Design*. Springer, New York, NY, 1 edition, 2001.

[54] J. M. Gere. *Mechanics of Materials*. Thomson Learning Inc., Belmont, Ca, 6 edition, 2004.

[55] S. Salsa. *Partial Differential Equations in Action - From Modelling to Theory*. Springer, New York, NY, 3 edition, 2016.

[56] S. Timoshenko and J. N. Goodier. *Theory of Elasticity*. McGraw-Hill Book Company, Inc., New York, NY, 2 edition, 1951.

[57] K. G. Kalhauge, A. K. Pedersen, J. Y. Pan, N. A. Michaelsen, O. Hansen, and D. H. Petersen. Vibration tolerant two-beam cantilevers for small pitch micro-electrodes. *Manuscript to be submitted for publication in Journal of Micromechanics and Microengineering*, 2019.

[58] Ultimaker. Techinical data sheet pla. `https://ultimaker.com/download/74599/UM180821%20TDS%20PLA%20RB%20V10.pdf`, 11 2019.

[59] Kuentz. Additive manufacturing and characterization of polylactic acid (pla) composites containing metal reinforcements. `https://ntrs.nasa.gov/archive/nasa/casi.ntrs.nasa.gov/20160010284.pdf`, 11 2019.

[60] CAPRES. Capres homepage. `http://capres.com/`, 10 2019.

[61] Tektronix. Model 7709 - user's guide - pa-771 rev. b / 8-03. `https://www.tek.com/default-accessory-series-manual-22`, 10 2019.

[62] Dattatray J. Late, Bin Liu, H. S. S. Ramakrishna Matte, Vinayak P. Dravid, and C. N. R. Rao. Hysteresis in single-layer mos2 field effect transistors. *ACS Nano*, 6(6):5635–5641, 2012. PMID: 22577885.

[63] Naveen Kaushik, David M. A. Mackenzie, Kartikey Thakar, Natasha Goyal, Bablu Mukherjee, Peter Boggild, Dirch Hjorth Petersen, and Saurabh Lodha. Reversible hysteresis inversion in mos2 field effect transistors. *npj 2D Materials and Applications*, 1(1):34, 2017.

[64] Mikkel R. Lotz, Mads Boll, Frederik W. Østerberg, Ole Hansen, and Dirch H. Petersen. Mesoscopic current transport in two-dimensional materials with grain boundaries: Four-point probe resistance and hall effect. *Journal of Applied Physics*, 120(13):134303, 2016.

[65] Fei Wang, Dirch H. Petersen, Torben M. Hansen, Toke R. Henriksen, Peter Bøggild, and Ole Hansen. Sensitivity study of micro four-point probe measurements on small samples. *Journal of Vacuum Science & Technology B*, 28(1):C1C34–C1C40, 2010.

A | Appendix

A.1 Rotation Matrix Code

```
%% RotMaker
% [Rot] = RotMaker(Th,Ph)
% Calculates the rotation matrices for a vector of theta values and a
% single Phi value
function [Rot] = RotMaker(Th,Ph)

[NN,~] = size(Th);
Rot = zeros(NN,3,3);

for i = 1:NN
    Rot(i,:,:) =    [cos(Th(i))*cos(Ph),-sin(Th(i)),-cos(Th(i))*sin(Ph);
                     sin(Th(i))*cos(Ph), cos(Th(i)),-sin(Th(i))*sin(Ph);
                     sin(Ph),            0,          cos(Ph)];
end
end
```

A.2 Compliance and Stiffness Tensor Code

```
%% Vibration Tolerant Cantilevers - Compliance and Spring Matrix Calculator
% Calculates the compliance and spring matrix for designs that it is given.
%
% [C,K] = AnVec(Vdata,Rot,Enu)
%
% Vdata: Vector of designs that is going to be calculated. Dimensions (N,9)
% Vdata = N * [-, -, L1, L2, W1, W2, theta, H, eta]
% Vdata has a line for each design.
%
% Rot: Rotation matricies for the given designs. Dimensions (N,3,3)
% Rot = N * [ 3 -X- 3 ]
%
% Enu: Vector containing the Young's Modulus and Poisson's Ration for the
% material calculated on. Dimensions (2,1)
% Enu = [Young's Modulus; Poisson's Ration]
%
% The output has the dimensions (N,3,3)
function [Cr,Kr] = AnVec(Vdata,Rot,Enu)

%% Constants
%% Math Constants
[NN, ~] = size(Vdata);
a   = Vdata(:,3)./Vdata(:,4);
b   = Vdata(:,8)./Vdata(:,5);
g   = Vdata(:,8)./Vdata(:,6);
eta = Vdata(:,9);
Rot = permute(Rot,[2,3,1]);

```

```
29 %% Material Constants
30 E   = Enu(1); % Young's Modulus [Pa]
31 nu  = Enu(2); % Poisson's Ratio [-]
32
33 %% Moments of inertia
34 % Iz1 = h * b1^3 / 12;            % m^4
35 % Iz2 = h * b2^3 / 12;            % m^4
36 % Iy1 = h^3 * b1 / 12;            % m^4
37 % Ix2 = h^3 * b2 / 12;            % m^4
38
39 %% Torsion Constant
40 KappaP = 1/3*ones(NN,1);
41 for k = 1:2:100
42     KappaP = KappaP - 64./(pi^5.*b) .* (1/k^5) .* tanh(k*pi*b/2);
43 end
44 Kappa = (1+nu)/2*KappaP.^(-1);
45 clear KappaP
46
47 % Other Constants
48 kon1 = 4 * Vdata(:,3).^3 ./ (E * Vdata(:,8).^4);
49 kon2 = Vdata(:,3) ./ (E * Vdata(:,8).^2);
50
51 %% Terms in the Compliance matrix
52 C = zeros(3,3,NN);
53 % As a result of Fx
54
55 C(1,1,:) = kon1 .* (g.^3./a.^3 + 3*b.^3./a.^2).* sin(eta).^2 ...
56     + kon2 .* (b + g./a .* cos(eta).^2) ;
57
58 C(2,1,:) = - kon1 .* (g.^3./a.^3 + 3*b.^3./a.^2).*cos(eta).*sin(eta)...
59     - kon1 .* 3/2.*b.^3./a .* sin(eta)...
60     + kon2 .* g./a .* cos(eta) .* sin(eta);
61
62 % As a result of Fy
63
64 C(1,2,:) = C(2,1,:);
65
66 C(2,2,:) = kon1 .* (b.^3 ...
67     + g.^3./a.^3 .* cos(eta).^2 ...
68     + 3*b.^3./a .* cos(eta) ...
69     + 3*b.^3./a.^2 .* cos(eta).^2 )...
70     + kon2 .* g./a .* sin(eta).^2;
71
72 % As a result of Fz
73
74 C(3,3,:) = kon1 .* ( b...
75     + g./a.^3 ...
76     + 3*b./a.*cos(eta) ...
77     + 3*b./a.^2.*cos(eta).^2 ...
78     + b.^3./a.^2.*Kappa.*sin(eta).^2);
79
80 %% Spring Matrix
81 Cr = zeros(NN,3,3);
82 Kr = zeros(NN,3,3);
83
84 % for i = 1:NN
85 %     Roti = pinv(Rot(:,:,i));
86 %     K    = pinv(C(:,:,i));
87 %     Cr(i,:,:) = Roti * C(:,:,i)  * Rot(:,:,i);
88 %     Kr(i,:,:) = Roti * K * Rot(:,:,i);
89 % end
90
91
92 for i = 1:NN
93     Cr(i,:,:) = Rot(:,:,i) \      C(:,:,i)  * Rot(:,:,i);
94     Kr(i,:,:) = Rot(:,:,i) \ ( C(:,:,i) \ Rot(:,:,i));
95 end
96
97 end
```

A.3 Vibration Tolerance Code

```
%% Vibration Tolerance
% Gamma = VibTol(psi,VC,VK,mu)
% Calculates the vibration tolerance for at a specific angle psi
% mu is the friction coefficient.
function Gamma = VibTol(psi,VC,VK,mu)

Fx =  VK(:,1,1).*cos(psi)...
    + VK(:,1,2).*sin(psi);

Fy =  VK(:,2,1).*cos(psi) ...
    + VK(:,2,2).*sin(psi);

Fz =  VK(:,3,1).*cos(psi) ...
    + VK(:,3,2).*sin(psi);

P  =  mu * VC(:,3,3).^(-1);

Gamma = P ./ ( sqrt( Fx.^2 + Fy.^2 ) - mu * Fz );

end
```

A.4 Vibration Tolerance Minimizer Code

```
%% Vibration Tolerance Calculator
% [Gamma,S] = VibVecPsi(Vdata,VC,VK,psi,mu)
% Finds the angle at which the vibration tolerance is lowest
function [Gamma,S] = VibVecPsi(Vdata,VC,VK,psi,mu)

[NN,~] = size(Vdata);
m = psi(2);
S = ones(NN,1)*psi(1);

for k = 1:4
    So = zeros(NN,1); % The
    a = VibTol(S+m,VC,VK,mu) - VibTol(S,VC,VK,mu); % The slope +psi direction
    b = VibTol(S-m,VC,VK,mu) - VibTol(S,VC,VK,mu); % The slope -psi direction
    lo = ones(NN,1)-(a>0).*(b>0); % if both are + it
    % doesn't move until next iteration, where the step size is smaller
        a = a.*lo;
        b = b.*lo;

    n = sign(b-a);       % The direction with the biggest slope is chosen
        n = n + (n==0); % In the case of similar slopes, positive is chosen

    while sum(sum(sum(sum(So-S)))) ~= 0 % As long as there are
        So = S;
        S = S + n * m .*(VibTol(S,VC,VK,mu) > VibTol(S+n*m,VC,VK,mu));
    end
    m = m/10;
end
Gamma = VibTol(S,VC,VK,mu);

end
```

A.5 Multiple Design Calculator Code

```
clearvars -except H W1 CanDes Design Loop
% close all
% clc

%% Constants
LT      = Design(10);  % Total length (um)
CD      = 0.5e-6;      % Critical Dimension (um)
```

```
W2      = CD;           % Width 2 (um)
Ph      = pi/6;         % Phi (rad);
Enu(1)  = 70e9;         % Young's Modulus (Pa)
Enu(2)  = 0.17;         % Poisson's Ratio (-)
Psi1    = pi;           % Psi 1 (rad)
Psi2    = 0.01;         % Psi 2 (rad) approx zero
psim    = pi/10;        % psi steps
mu      = 0.2;          % friction coefficient


%% Variables
% theta
thn = 91;
Th = linspace(0,pi/4,thn);
% eta
etan = 91;
% lambda
lamn = 91;
lamb = linspace(1,5,lamn);

%% Design Matrix
NN = thn*etan*lamn;
datamat = zeros(NN,14);
% Rot     = zeros(NN,3,3);

n = 0;
for i1 = 1:thn
    eta = linspace(Th(i1),Th(i1)+pi/3,etan);
    for i2 = 1:lamn
        for i3 = 1:etan
            n = n + 1;
            L2 = (LT)/(lamb(i2)*cos(Th(i1))+cos(eta(i3)-Th(i1)));
            L1 = lamb(i2)*L2;
            datamat(n,[3:10,13]) = ...
                    [L1,L2,W1,W2,Th(i1),H,eta(i3),LT,CD];
        end
    end
end
%% Rotation Matrix and Compliance and Stiffness tensor
Rot = RotMaker(datamat(:,7),Ph);
[CT,KT] = AnVec(datamat,Rot,Enu);
datamat(:,2)    = CT(:,3,3).^(-1);
datamat(:,11)   = CT(:,2,2).^(-1);

%% Vibration Tolerance
[Gam1,ang1] = VibVecPsi(datamat,CT,KT,[Psi1,psim],mu);
[Gam2,ang2] = VibVecPsi(datamat,CT,KT,[Psi2,psim],mu);
ANG = [ang1,ang2];

[datamat(:,1), In] = min([Gam1,Gam2],[],2);
Index = (1:length(In))' + (In-1).*length(In);
datamat(:,14) = ANG(Index);



%% Reshape variables
GAMMAT = datamat(:,1);
GAMMAT = permute(reshape(GAMMAT,[etan,lamn,thn]),[1,3,2]);

CZZMAT = permute(reshape(datamat(:,2),[etan,lamn,thn]),[1,3,2]);

thetaX = unique(datamat(:,7));
etaY = unique(round(datamat(:,9)-datamat(:,7),5));
lamvec = round(datamat(:,3)./datamat(:,4),5);
lambdaZ = unique(lamvec);

[X, Y, Z] = meshgrid(thetaX,etaY,lambdaZ);
```

A.6 Surface Plotting Code

```
% close all
% Create figure
At  = CanDes(7)*180/pi;
Aet = (CanDes(9)-CanDes(7))*180/pi;
Al  = CanDes(11);
Dt  = Design(7)*180/pi;
Det = (Design(9)-Design(7))*180/pi;
Dl  = Design(11);

lt = ["-","--","-.",":","-","--","-.",":","-"];
lc = [1.01 1.05 1.2 1.3 1.4 1.5 1.7 2.0 Design(12)*1e6];
co = [0 0 0; 0 0 0; 0 0 0; 0 0 0; 1 0 0; 1 0 0; 1 0 0; 1 0 0; 1 0 1];

[cX,cY] = meshgrid(thetaX*180/pi,etaY*180/pi);
cZ(:,:,1) = (datamat(1,5)*1e6 + 0.5)./cosd(cX);
cZ(:,:,2) = (datamat(1,6)*1e6 + 0.5)./cosd(cY);
cZ = max(cZ,[],3);

%%
figure1 = figure('PaperSize',[40 50]);
axes1 = axes('Parent',figure1,'FontName','Times New Roman','FontSize',14);
gv = [0.01 0.02 0.03 0.05];

X1 = X*180/pi;
Y1 = Y*180/pi;

hold on;
p = patch(isosurface(X1,Y1,Z,GAMMAT,gv(1)));
isonormals(X1,Y1,Z,GAMMAT,p)
set(p,'FaceColor','red','EdgeColor','none',...
    'DisplayName',['\Gamma = ' num2str(gv(1))]);
p = patch(isosurface(X1,Y1,Z,GAMMAT,gv(2)));
isonormals(X1,Y1,Z,GAMMAT,p)
set(p,'FaceColor','green','FaceAlpha',0.8,'EdgeColor','none',...
    'DisplayName',['\Gamma = ' num2str(gv(2))]);
p = patch(isosurface(X1,Y1,Z,GAMMAT,gv(3)));
isonormals(X1,Y1,Z,GAMMAT,p)
set(p,'FaceColor','magenta','FaceAlpha',0.7,'EdgeColor','none',...
    'DisplayName',['\Gamma = ' num2str(gv(3))]);
p = patch(isosurface(X1,Y1,Z,GAMMAT,gv(4)));
isonormals(X1,Y1,Z,GAMMAT,p)
set(p,'FaceColor','cyan','FaceAlpha',0.6,'EdgeColor','none',...
    'DisplayName',['\Gamma = ' num2str(gv(4))]);
grid on
xlim([0 45])
ylim([0 60])
zlim([1 5])
ylabel('$\eta-\theta$','Interpreter','latex','FontSize',16,...
    'FontName','Times New Roman')
xlabel('$\theta$','Interpreter','latex','FontSize',16,...
    'FontName','Times New Roman')
zlabel('$\lambda$','Interpreter','latex','FontSize',16,...
    'FontName','Times New Roman')
view(-145,35)
legend1 = legend(axes1,'show');
set(legend1,'Position',[0.75 0.65 0.1915 0.1998]);
% Create light

light('Parent',axes1,'Position',[0 0 10],'Style','local')

% Contour lines and design specifiers
for i = 1:9
    [CC,HH]= contour(cX,cY,cZ,[lc(i), lc(i)],...
        'ShowText','off','linecolor',co(i,:),'linestyle',lt{i},...
        'linewidth',2,'HandleVisibility','off');
    HH.ContourZLevel = 1;
end
```

```
68  title(['$H = ' num2str(round(datamat(1,8)*1e9)) '$nm $W_a = ' ...
69      num2str(datamat(1,5)*1e9) '$nm'],...
70      'Interpreter','latex','FontSize',18,...
71      'FontName','Times New Roman')
72  plot3(At,Aet,Al,'r.','markersize',20,'HandleVisibility','off')
73  plot3(Dt,Det,Dl,'b.','markersize',20,'HandleVisibility','off')
74  plot3([At At],[Aet Aet],[1 Al],'r-','linewidth',2,'HandleVisibility','off')
75  plot3([Dt Dt],[Det Det],[1 Dl],'b-','linewidth',2,'HandleVisibility','off')
76  plot3([At Dt],[Aet Det],[Al Dl],'y-','linewidth',1.2,'HandleVisibility','off')
77
78  name=['fig/Gam/OptiS_Gam_H=' num2str(round(datamat(1,8)*1e9))...
79      'W1=' num2str(datamat(1,5)*1e9) '.png'];
80  saveas(gcf, name);
81
82
83  %% Create figure
84  figure2 = figure('PaperSize',[40 50]);
85  axes2 = axes('Parent',figure2,'FontName','Times New Roman','FontSize',14);
86  cv = [7 10 13 15];
87
88  X1 = X*180/pi;
89  Y1 = Y*180/pi;
90
91  hold on;
92  p = patch(isosurface(X1,Y1,Z,CZZMAT,cv(1)));
93  isonormals(X1,Y1,Z,CZZMAT,p)
94  set(p,'FaceColor','red','EdgeColor','none',...
95      'DisplayName',['C_{zz}^{-1} = ' num2str(cv(1)) ' N/m']);
96  p = patch(isosurface(X1,Y1,Z,CZZMAT,cv(2)));
97  isonormals(X1,Y1,Z,CZZMAT,p)
98  set(p,'FaceColor','green','FaceAlpha',0.8,'EdgeColor','none',...
99      'DisplayName',['C_{zz}^{-1} = ' num2str(cv(2)) ' N/m']);
100 p = patch(isosurface(X1,Y1,Z,CZZMAT,cv(3)));
101 isonormals(X1,Y1,Z,CZZMAT,p)
102 set(p,'FaceColor','magenta','FaceAlpha',0.7,'EdgeColor','none',...
103     'DisplayName',['C_{zz}^{-1} = ' num2str(cv(3)) ' N/m']);
104 p = patch(isosurface(X1,Y1,Z,CZZMAT,cv(4)));
105 isonormals(X1,Y1,Z,CZZMAT,p)
106 set(p,'FaceColor','cyan','FaceAlpha',0.6,'EdgeColor','none',...
107     'DisplayName',['C_{zz}^{-1} = ' num2str(cv(4)) ' N/m']);
108 grid on
109 xlim([0 45])
110 ylim([0 60])
111 zlim([1 5])
112 ylabel('$\eta-\theta$','Interpreter','latex','FontSize',16,...
113     'FontName','Times New Roman')
114 xlabel('$\theta$','Interpreter','latex','FontSize',16,...
115     'FontName','Times New Roman')
116 zlabel('$\lambda$','Interpreter','latex','FontSize',16,...
117     'FontName','Times New Roman')
118 view(-145,35)
119 legend2 = legend(axes2,'show');
120 set(legend2,'Position',[0.75 0.65 0.1915 0.1998]);
121
122 % Create light
123 light('Parent',axes2,'Position',[0 0 -1],'Style','local')
124
125 % Contour lines and design specifiers
126 for i = 1:9
127     [CC,HH]= contour(cX,cY,cZ,[lc(i), lc(i)],...
128         'ShowText','off','linecolor',co(i,:),'linestyle',lt{i},...
129         'linewidth',2,'HandleVisibility','off');
130     HH.ContourZLevel = 1;
131 end
132 title(['$H = ' num2str(round(datamat(1,8)*1e9)) '$nm $W_a = ' ...
133     num2str(datamat(1,5)*1e9) '$nm'],...
134     'Interpreter','latex','FontSize',18,...
135     'FontName','Times New Roman')
136 plot3(At,Aet,Al,'r.','markersize',20,'HandleVisibility','off')
137 plot3(Dt,Det,Dl,'b.','markersize',20,'HandleVisibility','off')
```

```
plot3([At At],[Aet Aet],[1 Al],'r-','linewidth',2,'HandleVisibility','off')
plot3([Dt Dt],[Det Det],[1 Dl],'b-','linewidth',2,'HandleVisibility','off')
plot3([At Dt],[Aet Det],[Al Dl],'y-','linewidth',1.2,'HandleVisibility','off')

name=['fig/Czz/OptiS_Czz_H=' num2str(round(datamat(1,8)*1e9))...
    'Wl=' num2str(datamat(1,5)*1e9) '.png'];
saveas(gcf, name);
```

A.7 Optimization for same pitch

```
clear
close all
%% Define material constants
Enu = [70e9 0.17]; % SiO2
psi = [0.01 pi/18];
Ph = pi/6;
%% Define Original Cantilever
CanDes = zeros(1,10);
CanDes(3:9) = [8.7e-6 4.3e-6 0.91e-6 0.5e-6 20*pi/180 1.11e-6 40*pi/180];

% Creates rotation matrix for initial design
CanRot = RotMaker(CanDes(1,7),Ph);

% Calculates s t i f f n e s s and compliance tensor for initial design
[Cc,Kc] = AnVec(CanDes,CanRot,Enu);
TargetStiffness = Cc(1,3,3).^(-1);
CanDes(1,2) = TargetStiffness;

% Calculates the vibration tolerance for the initial design
[TargetTolerance,~] = VibVecPsi(CanDes,Cc,Kc,psi,0.2);
CanDes(1,1) = TargetTolerance;
% Calculates the total length L_T for the initial design
CanDes(1,10) = CanDes(1,3)*cos(CanDes(1,7)) +...
    CanDes(1,4)*cos(CanDes(1,9)-CanDes(1,7));
% Calculates lambda for the initial design
CanDes(1,11) = CanDes(1,3)/CanDes(1,4);

%% Max angles
S = (CanDes(1,5)+0.5e-6 )/cos(CanDes(1,7));
ETA = acos((CanDes(1,6)+0.5e-6)/S) + CanDes(1,7);

%% Optimization of design over Lambda and H
% creates the seed design ( i.e. original design ).
Seed = CanDes;
Seed(1,9) = ETA;
% calculates lambda and H vectors
Lambda  = linspace(1,5,101);
Ln      = length(Lambda);
H       = linspace(1,3,101)*1e-6;
Hn      = length(H);
% Defines the new designs
OptiMat = repmat(Seed,[Ln*Hn,1]);
n = 0;
for h = 1:Hn
    for l = 1:Ln
        n = n + 1;
        L2 = Seed(10)/(Lambda(l)*cos(Seed(7))+cos(Seed(9)-Seed(7))); % L2
        L1 = Lambda(l)*L2; % L1
        OptiMat(n,3:4) = [L1, L2];
        OptiMat(n,8) = H(h);
    end
end

% Rotation matrix
OptiRot = RotMaker(OptiMat(:,7),Ph);
% compliance and stiffness tensor
[OptiC,OptiK] = AnVec(OptiMat,OptiRot,Enu);
OptiMat(:,2) = OptiC(:,3,3).^(-1);
% vibration tolerance
```

```
[OptiMat(:,1),~] = VibVecPsi(OptiMat,OptiC,OptiK,psi,0.2);
% reshape vector to matrix
MatDes = reshape(OptiMat,[Ln,Hn,11]);
CZZ_opt = MatDes(:,:,2);
GAM_opt = MatDes(:,:,1);
[XH,YL] = meshgrid(H,Lambda);

%% Czz plot and interpolation
figureA = figure('PaperSize',[40 50]);
axesA = axes('Parent',figureA,'FontName','Times New Roman','FontSize',14);
hold on
surf(XH,YL,CZZ_opt,'linewidth',0.1,'edgealpha',0.5)
xlabel('$H$ (m)','Interpreter','latex','FontSize',16,...
    'FontName','Times New Roman')
xlim([H(1) H(end)])
ylabel('$\lambda$','Interpreter','latex','FontSize',16,...
    'FontName','Times New Roman')
ylim([Lambda(1) Lambda(end)])
zlabel('$C_{zz}^{-1}$ (N/m)','Interpreter','latex','FontSize',16,...
    'FontName','Times New Roman')
% Finds contour line for Czz that has the same value as the original design
[CC,HH]= contour(XH,YL,CZZ_opt,[TargetStiffness TargetStiffness],...
        'ShowText','off','linecolor','red','linestyle','-',...
        'linewidth',2,'HandleVisibility','off');
    HH.ContourZLevel = TargetStiffness;
view(3)
grid on
saveas(gcf, 'fig/Alberto_Optimization_Czz.png');


% Interpolate along the contour line to get the other values
H_interp = CC(1,2:end);
L_interp = CC(2,2:end);
Gam_interp = interp2(XH,YL,GAM_opt,H_interp,L_interp);
[mG, In] = max(Gam_interp);
mH = H_interp(In);
mLam = L_interp(In);




%% Gamma plot and maximum
figureB = figure('PaperSize',[40 50]);
axesB = axes('Parent',figureB,'FontName','Times New Roman','FontSize',14);
hold on
surf(XH,YL,GAM_opt,'linewidth',0.1,'edgealpha',0.5)
xlabel('$H$ (m)','Interpreter','latex','FontSize',16,...
    'FontName','Times New Roman')
xlim([H(1) H(end)])
ylabel('$\lambda$','Interpreter','latex','FontSize',16,...
    'FontName','Times New Roman')
ylim([Lambda(1) Lambda(end)])
zlabel('$\Gamma$','Interpreter','latex','FontSize',16,...
    'FontName','Times New Roman')

plot3(H_interp,L_interp,Gam_interp,'r-','linewidth',2)
plot3(mH,mLam,mG,'g.','markersize',20)
view(3)
grid on
saveas(gcf, 'fig/Alberto_Optimization_Gam.png');


%% New Best Point
% Writes down new design
L2 = Seed(10)/(mLam*cos(Seed(7))+cos(Seed(9)-Seed(7)));
L1 = mLam * L2;
Design = Seed;
Design(3:4) = [L1 L2];
Design(8) = mH;
Design(10) = L1*cos(Seed(7)) + L2*cos(Seed(9)-Seed(7));
```

```
Design(11) = mLam;
RR = RotMaker(Design(7),Ph);

[DC,DK] = AnVec(Design,RR,Enu);
Design(2) = DC(1,3,3).^(-1);

[DG,~] = VibVecPsi(Design,DC,DK,psi,0.2);
Design(1) = DG;

% prints relevant values
fprintf('Czz Alberto: %0.4f, New: %0.4f\n',TargetStiffness,Design(2))
fprintf('Gam Alberto: %0.4f, New: %0.4f\n',TargetTolerance,DG)
fprintf('Lam Alberto: %0.4f, New: %0.4f\n',CanDes(11),Design(11))
fprintf('H   Alberto: %0.4f, New: %0.4f\n',CanDes(8)*1e6,Design(8)*1e6)

clearvars -except AlbertoDesign Design
```

A.8 Optimize for better pitch, and best possible vibration tolerance

```
clear
close all
%% Define material constants and Phi
Enu = [70e9 0.17]; % SiO2
psi = [0.01 pi/18];
Ph = pi/6;
%% Define original Cantilever

CanDes = zeros(1,10);
CanDes(3:9) = [8.7e-6 4.3e-6 0.91e-6 0.5e-6 20*pi/180 1.11e-6 40*pi/180];

% Creates rotation matrix for initial design
CanRot = RotMaker(CanDes(1,7),Ph);

% Calculates stiffness and compliance tensor for initial design
[Cc,Kc] = AnVec(CanDes,CanRot,Enu);
TargetStiffness = Cc(1,3,3).^(-1);
CanDes(1,2) = TargetStiffness;

% Calculates the vibration tolerance for the initial design
[TargetTolerance,~] = VibVecPsi(CanDes,Cc,Kc,psi,0.2);
CanDes(1,1) = TargetTolerance;

% Calculates the total length L_T of the initial design
CanDes(1,10) = CanDes(1,3)*cos(CanDes(1,7)) +...
    CanDes(1,4)*cos(CanDes(1,9)-CanDes(1,7));

% Calculates Lambda for the initial design
CanDes(1,11) = CanDes(1,3)/CanDes(1,4);

% Finds smallest possible pitch that can sustain the initial cantilever
Salb(1) = (CanDes(5)+0.5e-6)/cos(CanDes(7));
Salb(2) = (CanDes(6)+0.5e-6)/cos(CanDes(9)-CanDes(7));
CanDes(1,12) = max(Salb);


%% Target
TargetPitch = 1.1e-6;

%% Optimization of design over W1 and H

% creates the seed design (i.e. original design).
Seed = CanDes;
% calculates W1 and H vectors
W1max = TargetPitch - 0.5e-6;
W1    = linspace(0.5e-6,W1max,61);
W1n   = length(W1);
H     = linspace(1,3,101)*1e-6;
```

```
Hn        = length(H);

% Defines the new designs
OptiMat = repmat(Seed,[W1n*Hn,1]);
n = 0;
for h = 1:Hn
    for w = 1:W1n
        n = n + 1;
        Th = acos(( W1(w) + 0.5e-6 )/ TargetPitch); % Calculates theta
        Et = acos(( Seed(6) + 0.5e-6)/TargetPitch) + Th; % Calculates eta
        OptiMat(n,4) = Seed(10)/(Seed(11)*cos(Th)+cos(Et-Th)); % L2
        OptiMat(n,3) = Seed(11)*OptiMat(n,4); % L1
        OptiMat(n,7) = Th;
        OptiMat(n,9) = Et;
        OptiMat(n,5) = W1(w);
        OptiMat(n,8) = H(h);
    end
end
OptiRot = RotMaker(OptiMat(:,7),Ph); % Calculates rotation matricies
[OptiC,OptiK] = AnVec(OptiMat,OptiRot,Enu); % Calculates Stiffness and
% compliance tensors
OptiMat(:,2) = OptiC(:,3,3).^(-1);
[OptiMat(:,1),~] = VibVecPsi(OptiMat,OptiC,OptiK,psi,0.2); % Calculates
% Vibration tolerance

MatDes = reshape(OptiMat,[W1n,Hn,12]); % Reshapes from vector to matrix
CZZ_opt = MatDes(:,:,2);
GAM_opt = MatDes(:,:,1);
[XH,YW] = meshgrid(H,W1);

%% Czz plot and interpolation
figureA = figure('PaperSize',[40 50]);
axesA = axes('Parent',figureA,'FontName','Times New Roman','FontSize',14);
hold on
surf(XH,YW,CZZ_opt,'linewidth',0.1,'edgealpha',0.5)
xlabel('$H$ (m)','Interpreter','latex','FontSize',16,...
    'FontName','Times New Roman')
xlim([H(1) H(end)])
ylabel('$W_1$ (m)','Interpreter','latex','FontSize',16,...
    'FontName','Times New Roman')
ylim([W1(1) W1(end)])
zlabel('$C_{zz}^{-1}$ (N/m)','Interpreter','latex','FontSize',16,...
    'FontName','Times New Roman')

% Finds contour line for Czz that has the same value as the original design
[CC,HH]= contour(XH,YW,CZZ_opt,[TargetStiffness TargetStiffness],...
        'ShowText','off','linecolor','red','linestyle','-',...
        'linewidth',2,'HandleVisibility','off');
    HH.ContourZLevel = TargetStiffness;
view(3)
grid on
saveas(gcf, 'fig/Alberto_Optimization_CzzS2.png');


% Interpolate along the contour line to get the other values
H_interp = CC(1,2:end);
W_interp = CC(2,2:end);
Gam_interp = interp2(XH,YW,GAM_opt,H_interp,W_interp);
Th_interp = interp2(XH,YW,MatDes(:,:,7),H_interp,W_interp);
Et_interp = interp2(XH,YW,MatDes(:,:,9),H_interp,W_interp);
[mG, In] = max(Gam_interp);
mH = H_interp(In);
mW = W_interp(In);
mT = Th_interp(In);
mE = Et_interp(In);



%% Gamma plot and maximum
figureB = figure('PaperSize',[40 50]);
```

```
119 axesB = axes('Parent',figureB,'FontName','Times New Roman','FontSize',14);
120 hold on
121 surf(XH,YW,GAM_opt,'linewidth',0.1,'edgealpha',0.5)
122 xlabel('$H$ (m)','Interpreter','latex','FontSize',16,...
123     'FontName','Times New Roman')
124 xlim([H(1) H(end)])
125 ylabel('$W_1$ (m)','Interpreter','latex','FontSize',16,...
126     'FontName','Times New Roman')
127 ylim([W1(1) W1(end)])
128 zlabel('$\Gamma$','Interpreter','latex','FontSize',16,...
129     'FontName','Times New Roman')
130
131 plot3(H_interp,W_interp,Gam_interp,'r-','linewidth',2)
132 plot3(mH,mW,mG,'g.','markersize',20)
133 view(3)
134 grid on
135 saveas(gcf, 'fig/Alberto_Optimization_GamS2.png');
136
137
138 %% New Best Point
139
140 % Writes down new design
141 Design = Seed;
142 Design(4) = Design(10) / (Design(11)*cos(mT) + cos(mE-mT));
143 Design(3) = Design(4)*Design(11);
144 Design(5) = mW;
145 Design(7) = mT;
146 Design(8) = mH;
147 Design(9) = mE;
148 Design(12) = TargetPitch;
149
150 RR = RotMaker(Design(7),Ph);
151 [DC,DK] = AnVec(Design,RR,Enu);
152 Design(2) = DC(1,3,3).^(-1);
153 [DG,~] = VibVecPsi(Design,DC,DK,psi,0.2);
154 Design(1) = DG;
155
156 % prints relevant values
157 fprintf('Czz Alberto: %0.4f, New: %0.4f\n',TargetStiffness,Design(2))
158 fprintf('Gam Alberto: %0.4f, New: %0.4f\n',TargetTolerance,DG)
159 fprintf('Lam Alberto: %0.4f, New: %0.4f\n',CanDes(11),Design(11))
160 fprintf('H   Alberto: %0.4f, New: %0.4f\n',CanDes(8)*1e6,Design(8)*1e6)
161 fprintf('S   Alberto: %0.4f, New: %0.4f\n',CanDes(12)*1e6,Design(12)*1e6)
162 fprintf('The Alberto: %0.4f, New: %0.4f\n',...
163     CanDes(7)*180/pi,Design(7)*180/pi)
164 fprintf('Eta Alberto: %0.4f, New: %0.4f\n',...
165     CanDes(9)*180/pi,Design(9)*180/pi)
166
167 clearvars -except AlbertoDesign Design
```

A.9 Finite Element Model

The finite element model used in this thesis, consists of two beams connected at the center of their end points. In order to avoid discontinuities, both beams a fitted with a semicircle at the joint. A force of 10 µN is applied at the tip of the cantilever in the x-, y- and z-directions, and the corresponding deflection is read out.

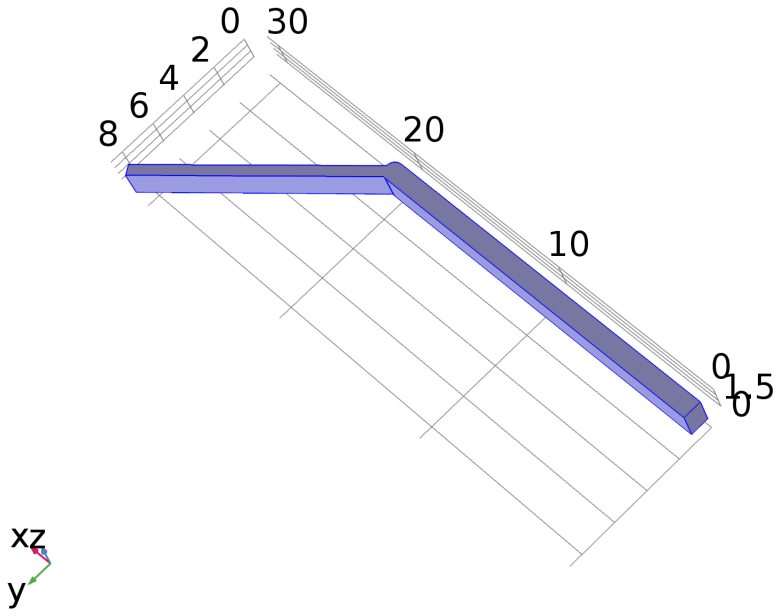

Figure A.1: Picture of the model used for the finite element model of the cantilevers.

A.10 Mounted Probe

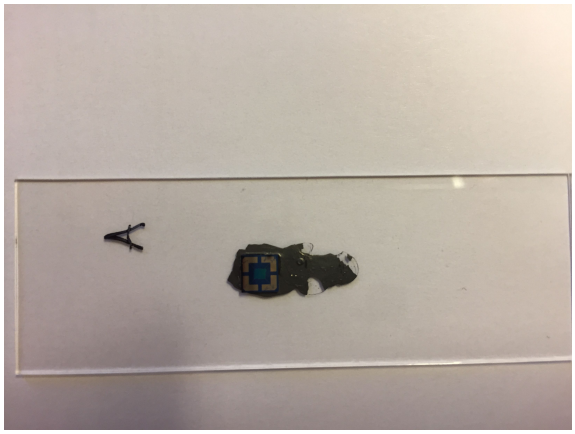

Figure A.2: Photograph of a MoS_2 sample mounted on a microscope slide using graphite glue.

A.11 Probe Engage Damage

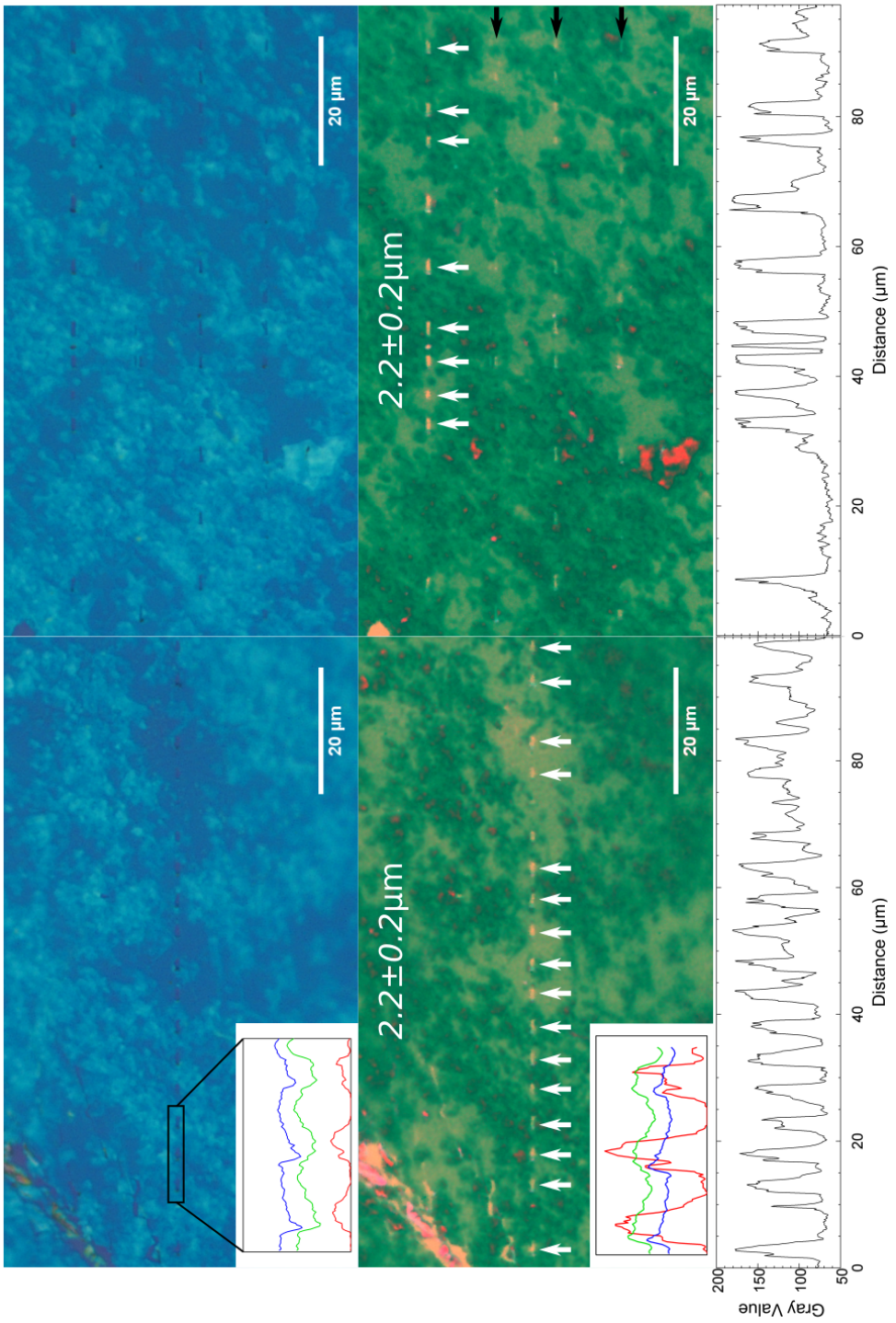

Figure A.3: Side by side comparison of the damage done by a straight probe and an L-shaped probe. The L-shaped probe is to the left and the straight to the right. The only mark for the L-shaped probe was made by the strain gauge, where all four cantilevers damaged the surface for the straight cantilever. The green pictures are the same as the blue, but with the green and blue signal inverted and the red signal enhanced.

Paper 1

J. Micromech. Microeng. **28** (2018) 095010

PhD Student Contribution: Theory, calculations, graphics and main writter.
Experiments designed and performed by Henrik Henrichsen.

IOP Publishing Journal of Micromechanics and Microengineering
J. Micromech. Microeng. **28** (2018) 095010 (6pp) https://doi.org/10.1088/1361-6439/aac58e

Vibration tolerance of micro-electrodes

Kristoffer G Kalhauge[1], Henrik H Henrichsen[2], Fei Wang[3], Ole Hansen[1] and Dirch H Petersen[1]

[1] Department of Micro and Nanotechnology, Technical University of Denmark, DTU Ørsteds Plads Building 345C, DK-2800 Kgs Lyngby, Denmark
[2] CAPRES A/S, Scion-DTU, Building 373, DK-2800 Kgs Lyngby, Denmark
[3] Department of Electrical and Electronic Engineering, Southern University of Science and Technology (SUSTech), Shenzhen 518055, People's Republic of China

E-mail: kgka@nanotech.dtu.dk

Received 16 February 2018, revised 9 May 2018
Accepted for publication 17 May 2018
Published 6 June 2018

Abstract

Micro four-point probe measurements can be used for extremely accurate electrical characterization of advanced electronic materials. The measurements are, however, sensitive to environmental vibrations which may compromise measurement quality severely. We have experimentally measured the vibration tolerance of two different micro-electrode designs (straight and three-way flexible) on two different samples (indium-tin-oxide and highly doped silicon). We show that three-way flexible electrodes are significantly more vibration tolerant (at least 50 times) compared to their straight counterparts. We have theoretically analyzed the vibration tolerance of the electrode designs and show excellent agreement between theory and experiment; as a result the theoretical framework may be used to predict vibration tolerance of any micro-electrode.

Keywords: micro four-point probe, electrical metrology, mechanical vibration, micro-electrodes

(Some figures may appear in colour only in the online journal)

1. Introduction

For more than a century the four-point probe (4PP) has been a preferred method for precise electrical characterization of materials [1–3]. However, the size of the probes and the contact force during engagement have limited its use for measurements on ultra thin materials [4, 5].

Miniaturization obtained by use of microfabrication technologies has had a strong impact on micromanipulator performance [6] and also improved the performance of 4PP with the introduction of the micro four-point probe (M4PP) as an alternative to conventional 4PP [7]. During the past decade, M4PP measurements have become the most reliable method for electrical characterization of ultra-thin semiconducting layers [8]. Today, fully automatic systems can perform sheet resistance [9] and micro Hall effect [10, 11] measurements in scribe-line test pads using lock-in technique and configuration switching combined with advanced data treatment algorithms [12] for state-of-the-art reliability [4, 5, 13].

An M4PP typically comprises (at least) four cantilever electrodes extending from a silicon probe body. The cantilever electrodes are silicon or silicon dioxide beams coated with metal (e.g. Ni). During measurements the contact force of each electrode is around 10–100 μN, i.e. around five orders of magnitude lower than that of a conventional 4PP [8]. M4PPs can be made of metal coated polymer [14, 15], or alternatively measurements may be done with independently movable probes [16].

M4PP measurements rely on a static contact between the micro-electrodes and the test sample during the full duration of the data acquisition which lasts for several seconds. However, fully automatic metrology systems are most often placed in production environments with significant ambient vibrational noise, which could result in unintended motion of the contact points. If a static contact is not maintained during a measurement sequence, the result is discarded due to stringent measurement requirements imposed by the need for high reproducibility [12, 17–20].

 © 2018 IOP Publishing Ltd Printed in the UK

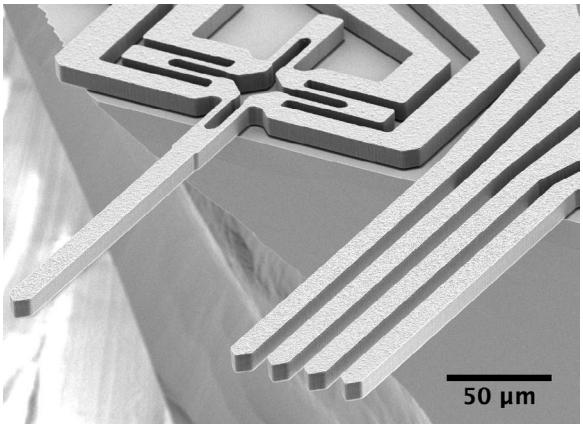

(a)

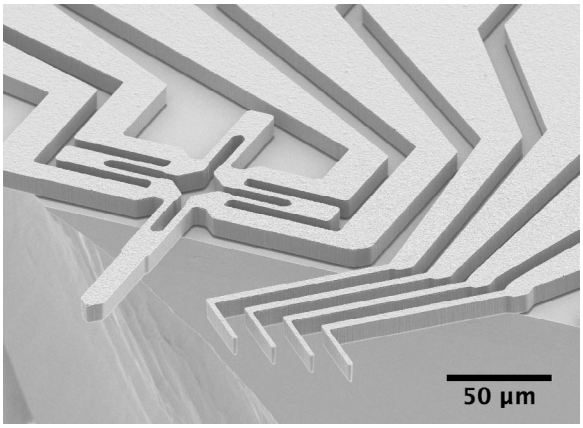

(b)

Figure 1. SEM images of micro four-point probes. (a) I-beam probes with straight electrodes. (b) L-beam probes with more flexible electrode beams. The images also show Wheatstone bridge strain-gauges (for surface detection) on both probes.

The original M4PP electrodes were simple straight cantilevers (I-beams) [7] as shown in figure 1(a). Later, high aspect ratio, three-way flexible cantilever electrodes (L-beams, figure 1(b)) were proposed for reducing abrasive wear of the electrode tips by forming a static contact [21, 22].

Here we experimentally determine the vibration tolerance of I-beam and L-beam cantilevers on two different sample surfaces as a function of engagement depth (i.e. contact force). We show experimentally that the L-beam has a higher vibration tolerance than that of the traditional I-beam. We also develop a theoretical model for the vibration tolerance of any cantilever with a known compliance tensor. We continue to calculate the vibration tolerance of the I-beam and L-beam cantilevers, and show that the model predictions are in excellent agreement with the experimental results.

2. Theory

In a typical measurement instrument, the electrodes are engaged with the sample at a tilt angle ϕ (e.g. $\phi = 30°$) and an engagement depth δ_z (e.g. $\delta_z = 500$ nm) to provide sufficient contact force F_N for reliable electrical contact. The

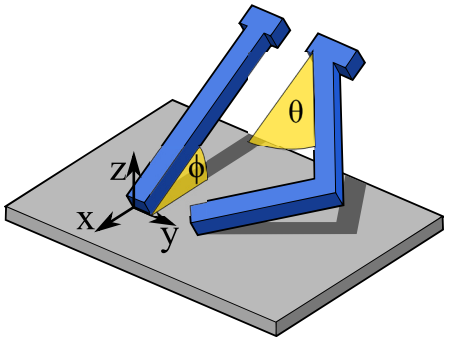

(a)

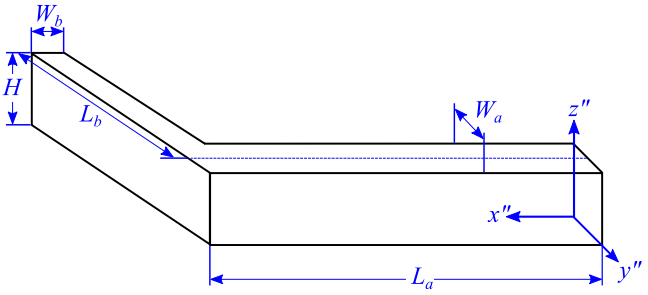

(b)

Figure 2. (a) Sketch of the electrode-sample geometry in the sample coordinate system. Both the I-beam and the L-beam electrodes are engaged with the sample at the tilt angle ϕ. The L-beam is attached to the probe body with the hinge angle θ. (b) Sketch of the L-beam electrode in the cantilever coordinate system illustrating the definition of geometry symbols.

electrode-sample geometry is illustrated in figure 2(a) for both I-beam and L-beam electrodes. Figure 2(a) also illustrates the sample based Cartesian coordinate system (x, y, z) we shall use for analysis of vibration tolerance, while figure 2(b) shows the cantilever based coordinate system (x'', y'', z'') which we shall use for analysis of the elastic behavior of the beams. Figure 2(b) also defines the geometry of the L-beam, which is attached to the probe body at the hinge angle θ as illustrated in figure 2(a). The analysis of vibration tolerance is simplified significantly if the electrode-sample contact is assumed to be point like such that the contact point can support forces, but not torques. Then the relation between the deflection vector $\boldsymbol{\delta}$ and force $\mathbf{F}$ on the electrode-tip is characterized by a stiffness $[\mathbf{K}]$ or compliance tensor $[\mathbf{C}] = [\mathbf{K}]^{-1}$, i.e. $\mathbf{F} = [\mathbf{K}]\boldsymbol{\delta}$ and $\boldsymbol{\delta} = [\mathbf{C}]\mathbf{F}$ as discussed by Wang *et al* [22].

During electrode-sample engage two extreme cases may occur: Either static contact is obtained, i.e. $\boldsymbol{\delta} = \delta_z\hat{\mathbf{z}}$ where $\hat{\mathbf{z}}$ is the unit vector normal to the surface of the sample. Or the cantilever slides on the surface until forces tangential to the surface vanish, i.e. $\mathbf{F} = F_N\hat{\mathbf{z}} = C_{zz}^{-1}\delta_z\hat{\mathbf{z}}$. In the analysis we shall assume sliding contact. During measurements, when the sample and probe are in contact, the sample may move relative to the probe body due to environmental noise vibrations, and then the contact point may or may not move on the sample depending on the vibration amplitude and properties of the contact and the electrode. We shall assume that the contact is maintained if the magnitude of the tangential force F_T is less than the total normal force $F_{N,tot}$ times the friction coefficient

μ, i.e. $|F_T| \leqslant \mu F_{N,tot}$, otherwise the contact point will slide on the surface and compromise measurement quality.

Consider now in-plane sample-body vibrations $\tilde{\boldsymbol{\delta}}(t)$ with the amplitude A at an arbitrary polar angle ψ to the x-axis

$$\tilde{\boldsymbol{\delta}}(t) = A\sin(\omega t)\begin{bmatrix}\cos\psi\\ \sin\psi\\ 0\end{bmatrix}, \tag{1}$$

where ω is the angular vibration frequency and t is time. The resulting force due to engagement with sliding contact and added vibration is $\mathbf{F} = F_N\hat{\mathbf{z}} + [\mathbf{K}]\tilde{\boldsymbol{\delta}}(t)$ and thus the total normal force $F_{N,tot}$ and tangential force F_T become

$$F_{N,tot} = C_{zz}^{-1}\delta_z + K_N(\psi)A\sin(\omega t), \tag{2}$$

$$F_T = K_T(\psi)A\sin(\omega t), \tag{3}$$

where $K_N(\psi)$ and $K_T(\psi)$ are effective normal and transverse spring constants, respectively. In terms of the stiffness tensor elements the spring constants are

$$K_N(\psi) = K_{zx}\cos\psi + K_{zy}\sin\psi, \tag{4}$$

$$K_T(\psi) = \sqrt{(K_{xx}\cos\psi + K_{xy}\sin\psi)^2 + (K_{yx}\cos\psi + K_{yy}\sin\psi)^2}. \tag{5}$$

The worst case scenario occurs when $|\sin(\omega t)| = 1$, and since $K_T(\psi)$ is always positive the vibration amplitude must fulfill

$$\frac{A}{\delta_z} \leqslant \frac{\mu C_{zz}^{-1}}{K_T(\psi) + \mu\,|K_N(\psi)|} \equiv \Gamma(\psi) \tag{6}$$

to avoid a sliding contact point according to the criterion $|F_T| \leqslant \mu F_{N,tot}$ discussed above. The vibration tolerance, in units of the engagement depth, for a vibration in the direction ψ is thus $\Gamma(\psi)$.

Depending on the design of the electrodes two simplified cases can be identified, i.e. in case $K_T(\psi) \gg \mu\,|K_N(\psi)|$ the vibration tolerance $\Gamma(\psi) \simeq \mu/[C_{zz}K_T(\psi)]$ is proportional to the friction coefficient, and in case $K_T(\psi) \ll \mu\,|K_N(\psi)|$ the vibration tolerance $\Gamma(\psi) \simeq 1/[C_{zz}\,|K_N(\psi)|]$ is independent on the friction coefficient.

The vibration tolerance for the I-beam is minimum at polar angles $\psi = 0 \pm \pi$ and maximum at $\psi = \pm\frac{\pi}{2}$, and the same is roughly the case for the L-beam, albeit with a negligible offset. At the minimum and maximum the vibration tolerance becomes

$$\Gamma(0) = \frac{\mu C_{zz}^{-1}}{\sqrt{{K_{xx}}^2 + {K_{yx}}^2} + \mu\,|K_{zx}|}, \tag{7}$$

$$\Gamma\left(\frac{\pi}{2}\right) = \frac{\mu C_{zz}^{-1}}{\sqrt{{K_{xy}}^2 + {K_{yy}}^2} + \mu\,|K_{zy}|}, \tag{8}$$

respectively.

2.1. Compliance tensors

To proceed further, the compliance tensors of the cantilevers must be calculated and here we use Euler's beam equation [23] and the double-primed cantilever coordinate system of figure 2(b).

The calculation of the compliance tensor describing the I-beam, which is a prismatic beam of length L_I, thickness H_I and width W_I, proceeds by assuming that one end is rigidly clamped to the probe body. The resulting I-beam compliance tensor $[\mathbf{C}_I'']$ in the cantilever coordinate system is

$$[\mathbf{C}_I''] = \begin{bmatrix}\frac{L_I}{EW_IH_I} & 0 & 0\\ 0 & \frac{4L_I^3}{EW_I^3H_I} & 0\\ 0 & 0 & \frac{4L_I^3}{EW_IH_I^3}\end{bmatrix} \tag{9}$$

where $E = 170$ GPa is Young's modulus of the beam material. Note, the element $C''_{I,xx}$ is a low compliance element which is controlled by longitudinal deformation. In the remaining non-zero elements the effect of longitudinal deformation is insignificant and thus ignored.

The L-beam consists of two prismatic beams, the first beam (length L_a, width W_a, and height H) is clamped to the probe body, while the second beam (length L_b, width W_b, and height H) is connected to the first beam at a 90° degree elbow. The compliance tensor $[\mathbf{C}_L'']$ for the L-beam cantilever was calculated by Wang *et al* [22]

$$[\mathbf{C}_L''] = \frac{1}{E}\begin{bmatrix}\frac{12L_aL_b^2}{W_a^3H} + \frac{4L_b^3}{W_b^3H} & -\frac{6L_a^2L_b}{W_a^3H} & 0\\ -\frac{6L_aL_b}{W_a^3H} & \frac{4L_a^3}{W_a^3H} & 0\\ 0 & 0 & \frac{4L_a^3}{W_aH^3} + \frac{4L_b^3}{W_bH^3} + \frac{EL_b^2}{k_\tau}\end{bmatrix}, \tag{10}$$

where k_τ is the torsion constant of the first prismatic bar of the L-beam [24]

$$k_\tau = \frac{EW_a^3H}{2(1+\nu)L_a}\left(\frac{1}{3} - \frac{64W_a}{\pi^5H}\beta\right), \tag{11}$$

where ν is Poisson's ratio and

$$\beta = \sum_{n=1}^{\infty}\frac{1}{(2n-1)^5}\tanh\frac{(2n-1)\pi H}{2W_a}. \tag{12}$$

These compliance tensors describe the deflection of the cantilever tips relative to the probe body in response to an applied force. However, the probe body may not be perfectly rigidly attached to the bulk of the instrument, and thus it is necessary to include also a system compliance $[\mathbf{C}_\varepsilon'']$ to fully describe the electrode-sample interaction. Since the impact of system compliance is significant only in low compliance directions of the cantilevers a system compliance tensor with only a single non-zero element is sufficient, i.e.

Table 1. Dimensions of the two cantilever designs used as defined in figure 2. The electrode pitch of both probes is 20 μm.

L-beam		I-beam	
Symbol	Value (μm)	Symbol	Value (μm)
H	9.7	H_{I}	9.9
L_{a}	92.1	L_{I}	201.0
L_{b}	36.9		
W_{a}	4.8	W_{I}	12.0
W_{b}	2.3		
θ	45°	θ_{I}	0°
ϕ	30°	ϕ_{I}	30°

$$[\mathbf{C}''_{\varepsilon}] = \begin{bmatrix} \varepsilon & 0 & 0 \\ 0 & 0 & 0 \\ 0 & 0 & 0 \end{bmatrix}, \tag{13}$$

with the non-zero element assigned the value $\varepsilon = 0.2$ mm N^{-1}, which is an insignificant compliance compared to all compliance elements except $C''_{\mathrm{L},xx}$, which is an order of magnitude smaller than ε. As a result the total compliance tensors are $[\mathbf{C}''_{\mathrm{I}_\varepsilon}] = [\mathbf{C}''_{\mathrm{I}}] + [\mathbf{C}''_{\varepsilon}]$ and $[\mathbf{C}''_{\mathrm{L}_\varepsilon}] \simeq [\mathbf{C}''_{\mathrm{L}}]$ for the I-beam and L-beam, respectively. The method used for determining the magnitude of ε is described in section 4.

For vibration tolerance calculations in the sample coordinate-system the compliance tensors are then rotated using the rotation matrix [22]

$$[\mathbf{T}] = \begin{bmatrix} \cos\theta\cos\phi & -\sin\theta & -\cos\theta\sin\phi \\ \sin\theta\cos\phi & \cos\theta & -\sin\theta\sin\phi \\ \sin\phi & 0 & \cos\phi \end{bmatrix}. \tag{14}$$

Table 1 shows the dimensions of the I-beam and L-beam cantilevers used in vibration tolerance calculations. The dimensions reported in table 1 were measured on SEM images of the beams. For the calculations the elastic parameters, Young's modulus $E = 170$ GPa and Poisson's ratio $\nu = 0.22$, were used [25].

Figure 3 shows the calculated vibration tolerances for I-beam (black) and L-beam (red) electrodes as a function of the polar angle ψ for two different values ($\mu = 0.2$ full lines and $\mu = 0.6$ dashed lines) of the electrode-sample friction coefficient. The curves labelled I$_\varepsilon$-beam (blue) results when the system compliance is included; the system compliance has a major effect on the calculated vibration tolerance for the I-beam as seen. The calculated vibration tolerance of the L-beam is roughly a factor of 50 higher than that of the I$_\varepsilon$-beam.

3. Experiment

The vibration tolerance of the cantilever probes (I$_\varepsilon$-beam and L-beam) shown in figure 1 was characterized experimentally by intentional vibration of the sample during dual configuration sheet resistance measurements. The sample to be measured was placed on a calibrated piezoelectric element, which was driven at a frequency of 100 Hz and with the vibration amplitude A steadily increased during a measurement

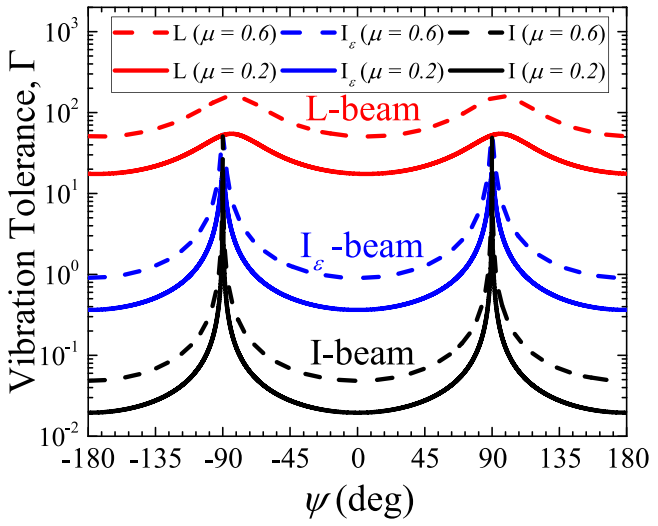

Figure 3. Calculated normalized vibration tolerance Γ for I-beam (black) and L-beam (red) cantilevers as a function of the polar angle ψ assuming friction coefficients $\mu = 0.2$ (full) and 0.6 (dashed). The curves in blue, labeled I$_\varepsilon$-beam, are calculated by taking into account the system compliance.

series. The direction of the sample vibration was aligned to the direction of minimum vibration tolerance for the cantilevers, i.e. $\psi \simeq 0$. Measurements were done on two different samples, i.e. on a silicon sample (Si) with a highly doped p-type shallow junction and on an indium-tin-oxide (ITO) sample with sheet resistances of 380 Ω and 90 Ω, respectively. Sheet resistance measurements were done using an M200 tool from CAPRES A/S, and performed according to industry standards with a 1% median filter on the dual configuration sheet resistance measurements [26].

Measurement failure is interpreted as caused by motion of the cantilever contact points on the sample surface. Thus, the absolute vibration tolerance $\Gamma\delta_z$ was experimentally defined as the minimum vibration amplitude A where the dual configuration sheet resistance measurement failed five times in a row (note in clarification: at larger amplitudes resistance measurements almost always fail, while smaller amplitudes result in less frequent measurement failures.). In this fashion the vibration tolerance was measured as a function of the engagement depth δ_z, which was varied in the range from 500 to 3000 nm, with an estimated error of 200 nm, as controlled by the probe stage on the M200. The engagement depth is measured as the set travel of the probe stage beyond detection of the surface. Representative measurements of the vibration tolerances of the I$_\varepsilon$-beams and the L-beams on the two samples are reported in figure 4.

4. Results and discussion

The experimental vibration tolerance data in figure 4 show that, indeed, the absolute vibration tolerance increases approximately linearly with increased engagement depth δ_z for each combination of probe (I-beam or L-beam) and sample (Si or ITO) as expected. The vibration tolerance of the L-beam is much larger than that of the I$_\varepsilon$-beam, and is, within measurement error,

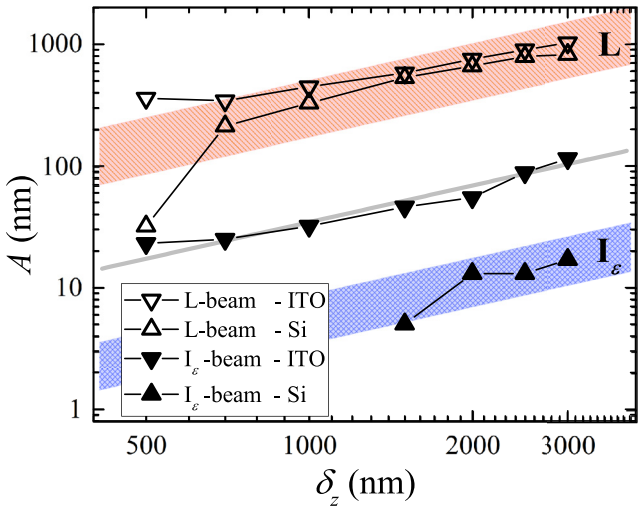

Figure 4. Experimental absolute vibration tolerance A as function of engagement depth δ_z for I_ε-beam and L-beam electrodes on Si and ITO samples. Theoretical predictions of the vibration amplitude for I_ε-beam and L-beam electrodes are shown as the blue and red bands respectively, for friction coefficients in the range $\mu = 0.2$ –0.6. The full grey line is the theoretical prediction for the I_ε-beam with an artificially large friction coefficient ($\mu \to \infty$), which agrees well with I_ε-beam measurements on ITO.

independent of the properties of the sample. This behavior is in stark contrast to the vibration tolerance of the I_ε-beam, which is strongly dependent of the properties of the sample, i.e. the vibration tolerance on Si is an order of magnitude lower than that on ITO. This sample dependence of the vibration tolerance can be understood by inspecting post-measurement SEM images (not shown) of the sample surfaces, which show rather deep indentations from the I_ε-beam on the ITO sample, but not on the Si sample. The indentations on the ITO sample effectively prevents the normal sliding motion on the surface; thereby the vibration tolerance is increased significantly.

In figure 4 error bars are not reported, but there are sources of error on both axes. The larger error is that of the engagement depth, which is determined based on a threshold signal from the built-in strain gauge on the probes (figure 1) and the motion of the calibrated probe stage of the M200 tool beyond this threshold. The threshold detection is expected to give a systematic error of at most 200 nm. The probe stage has a resolution of 2.5 nm and a position stability of 10 nm peak-to-peak; thus it contributes with a random error of at most 5.6 nm. The vibration amplitude is much more accurately determined, and here the main source of error is environmental vibration noise (a few nm) during the measurements. This noise affected the measurements for the I_ε-beam on Si where data could not be obtained at low engagement depths (below 1500 nm).

The experimental vibration tolerance of the L-beam is in very good agreement with the calculated vibration tolerance as illustrated by the red band (top) in figure 4, which shows calculated vibration tolerance for friction coefficients in the range from $\mu = 0.2$ to 0.6; i.e. almost all measurement points for both samples are within this band. The blue band (bottom) in figure 4 illustrates a similar calculation for the I_ε-beam assuming a system compliance $\varepsilon = 0.2$ mm N^{-1}, and again the agreement between experiment and theory is very good and essentially all measurement points on Si are within the band defined by the friction coefficient range (0.2–0.6).

The vibration tolerance of the I_ε-beam on ITO is an order of magnitude higher than that on Si and the theoretical prediction (blue band in figure 4), but as mentioned above the indentation of the electrode in the sample prevents the usual sliding motion on the surface. We may model this behavior by allowing an artificially high friction coefficient (i.e. $\mu \to \infty$) and then the normalized vibration tolerance becomes $\Gamma(0) \simeq 1/(C_{zz}\,|K_{zx}|)$, which is independent on μ. By fitting this simplified expression to the measurement data for the I_ε-beam on ITO using the system compliance ε as the fitting parameter produces the full grey line in figure 4 for $\varepsilon = 0.2$ mm N^{-1}, and the agreement with measurements is excellent. Thus, this experiment essentially measures the system compliance, and the resulting system compliance was also used to explain the data for the I_ε-beam on Si experiments in the previous paragraph.

5. Conclusion

We have measured the vibration tolerance of I-beam and L-beam electrodes on ITO and Si samples. The measurements show that L-beam electrodes are at least 50 times more vibration tolerant than I-beam electrodes. We have explained this behavior theoretically and the model of vibration tolerance we have developed is in excellent agreement with the experiments. Our theoretical framework may thus serve as a valuable tool for future micro-electrode design focusing on improved vibration tolerance.

Acknowledgments

The authors are thankful for financial support from H2020 European Project Nos. 692527 and 688225. We would further like to thank Lior Shiv from Capres A/S for fruitful discussions on cantilever design.

ORCID iDs

Kristoffer G Kalhauge https://orcid.org/0000-0002-9896-6289
Fei Wang https://orcid.org/0000-0003-1871-1022
Ole Hansen https://orcid.org/0000-0002-6090-8323
Dirch H Petersen https://orcid.org/0000-0002-9309-4186

References

[1] Valdes L B 1954 Resistivity measurements on germanium for transistors *Proc. IRE* **42** 420–7
[2] Smits F M 1958 Measurement of sheet resistivities with the four-point probe *Bell Syst. Tech. J.* **37** 711–8
[3] Miccoli I, Edler F, Pfnür H and Tegenkamp C 2015 The 100th anniversary of the four-point probe technique: the role of the probe geometries in isotropic and anisotropic systems *J. Phys.: Condens. Matter* **27** 223201
[4] Clarysse T H *et al* 2006 Accurate sheet resistance measurement on ultra-shallow profiles *MRS Proc.* **912** C05–7

[5] Clarysse T *et al* 2010 Photovoltage versus microprobe sheet resistance measurements on ultrashallow structures *J. Vac. Sci. Technol.* B **28** C1C8–14
[6] Mekid S, Bashmal S and Ouakad H M 2016 Nanoscale manipulators: review of conceptual designs through recent patents *Recent Pat. Nanotechnol.* **10** 44–58
[7] Petersen C L, Hansen T M, Bøggild P, Boisen A, Hansen O, Hassenkam T and Grey F 2002 Scanning microscopic four-point conductivity probes *Sensors Actuators* A **96** 53–8
[8] Petersen D H *et al* 2010 Review of electrical characterization of ultra-shallow junctions with micro four-point probes *J. Vac. Sci. Technol.* B **28** C1C27–33
[9] Thorsteinsson S, Wang F, Petersen D H, Hansen T M, Kjær D, Lin R, Kim J Y, Nielsen P F and Hansen O 2009 Accurate microfour-point probe sheet resistance measurements on small samples *Rev. Sci. Instrum.* **80** 053902
[10] Petersen D H, Hansen O, Lin R and Nielsen P F 2008 Micro-four-point probe Hall effect measurement method *J. Appl. Phys.* **104** 013710
[11] Worledge D C and Trouilloud P L 2003 Magnetoresistance measurement of unpatterned magnetic tunnel junction wafers by current-in-plane tunneling *Appl. Phys. Lett.* **83** 84–6
[12] Petersen D H 2009 Micro four-point probe and micro Hall effect: methods for reliable electrical characterization of ultra-shallow junctions *Phd Thesis* Technical University of Denmark
[13] Clarysse T *et al* 2008 On the analysis of the activation mechanisms of sub-melt laser anneals *Mater. Sci. Eng.* B **154–5** 24–30
[14] Kim J K, Choi Y S and Lee D W 2015 Surface-adaptable all-metal micro-four-point probe with unique configuration *J. Micromech. Microeng.* **25** 075023
[15] Keller S, Mouaziz S, Boero G and Brugger J 2005 Microscopic four-point probe based on SU-8 cantilevers *Rev. Sci. Instrum.* **76** 125102
[16] Kjeldby S B, Evenstad O M, Cooli S P and Wells J W 2017 Probing the dimensionality using a simplified 4-probe method *J. Phys.: Condens. Matter* **29** 394008
[17] Henrichsen H H, Hansen O, Kjaer D, Nielsen P F, Wang F and Petersen D H 2014 Precision of single-engage micro Hall effect measurements *Int. Workshop on Junction Technology* pp 55–8
[18] Worledge D C 2004 Reduction of positional errors in a four-point probe resistance measurement *Appl. Phys. Lett.* **84** 1695–7
[19] Kjaer D, Hansen O, Østerberg F W, Henrichsen H H, Markvardsen C, Nielsen P F and Petersen D H 2015 Characterization of positional errors and their influence on micro four-point probe measurements on a 100 nm Ru film *Meas. Sci. Technol.* **26** 095005
[20] Cagliani A, Østerberg F W, Hansen O, Shiv L, Nielsen P F and Petersen D H 2017 Breakthrough in current-in-plane tunneling measurement precision by application of multi-variable fitting algorithm *Rev. Sci. Instrum.* **88** 095005
[21] Petersen D H, Hansen O, Hansen T M, Petersen P R E and Bøggild P 2008 Static contact micro four-point probes with $<$11 nm positioning repeatability *Microelectron. Eng.* **85** 1092–5
[22] Wang F, Petersen D H, Jensen H V, Hansen C, Mortensen D, Friis L and Hansen O 2011 Three-way flexible cantilever probes for static contact *J. Micromech. Microeng.* **21** 085003
[23] Gere J M 2004 *Mechanics of Materials* 6th edn (Belmont, CA: Brooks/Cole–Thomson Learning)
[24] Timoshenko S and Goodier J N 1970 *Theory of Elasticity* 3rd edn (New York: McGraw-Hill)
[25] Sharpe W N, Yuan B, Vaidyanathan R and Edwards R L 1997 Measurements of Young's modulus, Poisson's ratio, and tensile strength of polysilicon *Proc. of the 10th IEEE Int. Workshop on Microelectromechanical Systems* pp 424–9
[26] CAPRES A/S homepage http://capres.com/ (Accessed: 28 May 2018)

Paper 2

Extended abstract for FCMN 2019 conference - accepted.

PhD Student Contribution: Writing and measurements.

Micro Four-Point Probe Electrical Characterization of MoS_2

Kristoffer G. Kalhauge[1], Abhay Shivayogimath[1,2], David M. A. Mackenzie[3], Henrik H. Henrichsen[4], Ole Hansen[1], Timothy J. Booth[1,2] and Dirch H. Petersen[1]

[1]*Department of Micro- and Nanotechnology, Technical University of Denmark, DTU Nanotech Building 345C, Kgs. Lyngby, DK-2800, Denmark*
[2]*Centre of Nanostructured Graphene (CNG), Technical University of Denmark, Ørsteds Plads 345C, Kgs. Lyngby, DK-2800, Denmark*
[3]*Department of Electronics and Nanoengineering, Aalto University, Micronova, Tietotie 3, 02150 Espoo, Finland*
[4]*CAPRES A/S, Scion-DTU, Building 373, Kgs Lyngby, DK-2800, Denmark*
Email: kgka@nanotech.dtu.dk

INTRODUCTION

Two dimensional (2D) materials have the possibility of becoming more widely used materials in the semiconductor industry, however for this to happen the industry must be able to produce consistently high-quality materials. To fulfill this requirement, metrology needs to be developed that can quickly and easily characterize the materials. At the moment the choice for electrical characterization of 2D materials is typically a combination of van der Pauw and Hall effect measurements [1] or building complete devices for characterization [2]. All of which involves one or more lithography steps increasing the risk of contamination as well as the possibility of changing or damaging the material. Here we present the use of micro four-point probes to characterize 2D materials as an alternative or complementary method. Micro four-point probes allow the user to skip disturbing lithography steps and measure directly on the raw material [3]. It also opens for the possibility of doing uniformity studies that are not possible with a fixed structure characterization method [4].

Micro Four-Point Probe Measurements

Similar to van der Pauw a micro four-point probe measurement is performed by sourcing either current or voltage through two electrodes while measuring the potential drop across two other electrodes. The difference is that while van der Pauw measurements are performed using fixed electrodes a micro four-point probe measurement is performed using a small probe (pin pitches on the micrometer scale) with all electrodes on a line, that can easily be moved around on the sample. A picture of a micro seven-point probe (from which a four-point sub probe can be chosen) is shown in Figure 1 (Left).

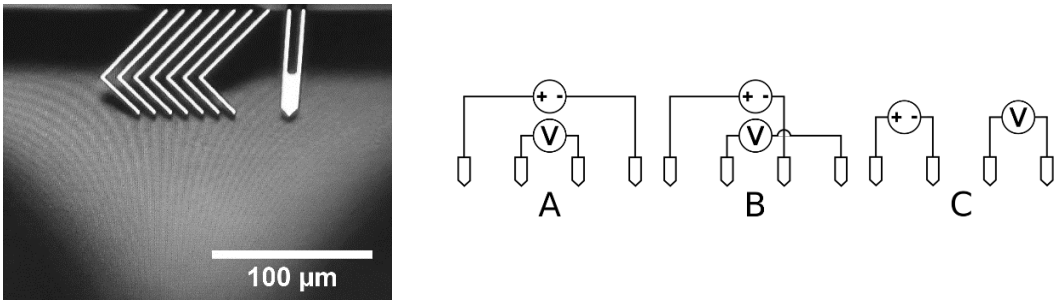

FIGURE 1. (Left) A microscope picture of a micro seven-point probe a few micrometers above an MoS_2 sample. (Right) Sketch of the three unique configurations of source-drain and sensing pins possible with a micro four-point probe.

There are three unique configurations of the source-drain and sensing pins, the configurations are shown in Figure 1 (Right). All other configurations will correspond to different permutations of the plus minus pins for the source-drain and sensing pins or switching the source-drain and sensing pins. At most these permutations should change the sign of the measured four-point voltage. The most important check of consistency for a four-point measurement, is the reciprocity theorem that states that the four-point resistance in the A-configuration must equal the sum of the four-point resistance in the B and C configuration i.e. $R_A = R_B + R_C$. As long as the material that is measured on is ohmic and nothing other than the configuration changes between measuring the configurations [5].

The Samples

The sample of interest is 1-2 layers of MoS_2 on a 300 nm SiO_2 layer on a highly doped Si wafer. The MoS_2 was grown in a CVD process using a gold catalyst on a sapphire substrate and transferred to the silicon substrate. The sample was characterized using Raman, photoluminescence and electron microscopy. The samples were also characterized electrically using a fixed array of electrodes [6].

FIELD EFFECT MEASUREMENTS USING MICRO FOUR-POINT PROBES

In this study we look at field effect measurements on MoS_2 using a micro four-point probe. A MicroRSP-M200 tool from CAPRES A/S was used as the mechanical platform to engage the micro four-point probe on the sample fixed in a customized sample holder as illustrated in Figure 2 (Left). DC voltage was then sourced between two probes using a Keithley 2400 and the corresponding current was measured using the same Keithley. The four-point voltage across the two other pins was measured using a Keithley 2700 that also switched between the configurations. In order to mechanically stabilize the sample and to ease the interface to the gate (i.e., the silicon substrate), the sample was glued to a microscope slide using electrically conductive graphite glue. Using a wire, the gate was connected to a voltage supply. A probe contacted to an MoS_2 sample is shown in Figure 2 (Left).

A full measurement cycle consists of a series of measurements at different gate voltages. At each voltage step all unique configurations are measured before changing to the next gate voltage. By performing the experiment in this way, (instead of sweeping the gate voltage for each configuration sequentially), it ensures that all configurations which are measured at the same gate voltage value, are close to each other temporally. This minimizes the impact of long time-scale drift.

This setup has been used to measure the sheet conductance of several pieces of MoS_2. Data from two of these are shown in Figure 2 (Right). The figure shows that the sheet conductance measured in A and B configurations are comparable within the same sample as expected. The differences can be explained by local inhomogeneities [7]. Both samples were measured in ambient air without any annealing. Below the threshold voltage the measurements become very noisy, which is to be expected since the device is in the off-state. Resulting in the current being of the same order of magnitude or lower than the noise floor.

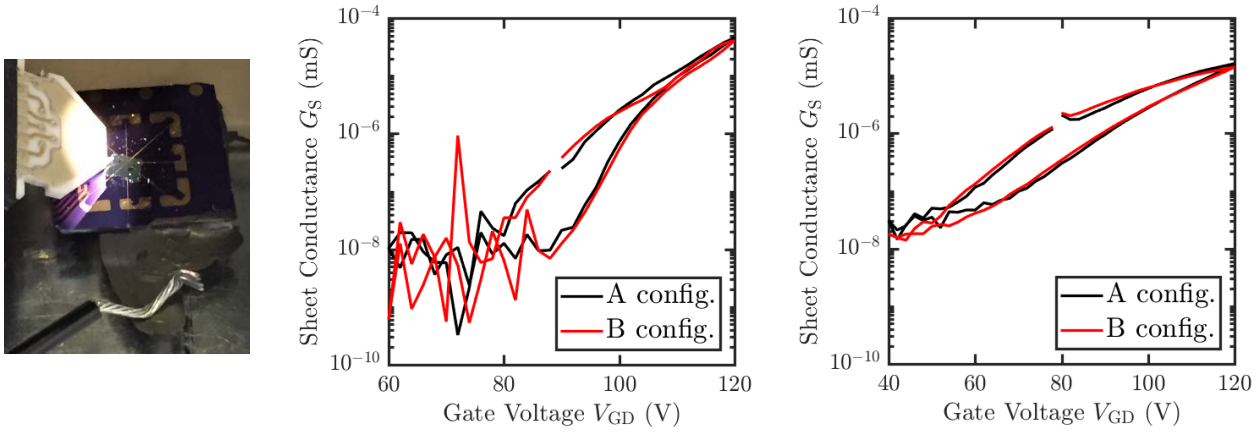

FIGURE 2. (Left) Picture of the micro four-point probe contacted to a sample of MoS_2. The wire shown is connecting to the back gate. (Right) Plot of the sheet conductance of two pieces of MoS_2, measured using micro four-point probes.

CONCLUSION

We show here that micro four-point probes can be used to characterize MoS_2 and can prove a viable alternative to van der Pauw measurements for device characterization, with the added feature of being a lithography free method. From these field effect measurements important parameters, such as the threshold voltage and the field effect mobility, can be determined at multiple points on the sample. Allowing the user to study the sample uniformity.

ACKNOWLEDGEMENTS

This project has received funding from the European Union's Horizon 2020 research and innovation program under grant agreements Nos. 692527 and 688225.

REFERENCES

1. K. F. Mak, K. L. McGill, J. Park and P. L. McEuen, *Science*, Vol. 344, Issue 6191 (2014), pp. 1489-1492
2. D. J. Late, B. Liu, H. S. S. R. Matte, V. P. Dravid, and C. N. R. Rao, *ACS Nano* 6, 6 (2012), 5635-5641
3. P. R. Whelan, V. Panchal, D. H. Petersen et al., *Appl. Mater. Interfaces*, 2018, 10 (37), pp 31641–31647
4. D.M.A. Mackenzie, J.D. Buron, P.R. Whelan et al., *Nano Res.* (2017) 10: 3596.
5. D. H. Petersen, O. Hansen, R. Lin and P. F. Nielsen, *J. Appl. Phys.*, 104 (2008), pp. 013710
6. A. Shivayogimath, J. D. Thomsen, D. M. A Mackenzie et al., *Cornell University Library*, (2018), arXiv:1805.08002
7. D. W. Koon, F. Wang, D. H. Petersen, *J. Appl. Phys*. 114 (2013), 163710

KEYWORDS

Micro four-point probe, 2D-materials, Field effect, Electrical characterization, MoS_2

]

Paper 3

Submitted to Nanotechnology

PhD Student Contribution: Data analysis of M4PP data together with David Mackenzie. Experiments performed by David Mackenzie and main writer David Mackenzie.

Wafer-scale quality assessment of graphene using micro four-point probe mapping

David M. A. Mackenzie[1,2,*], Kristoffer G. Kalhauge[1,3], Patrick Whelan[1,3], Frederik W. Østergaard[4], Iwona Pasternak[5], Wlodek Strupinski[5], Peter Bøggild[1,3], Peter U. Jepsen[6], Dirch H. Petersen[1,3]

[1]Center for Nanostructured Graphene (CNG), Technical University of Denmark, DK-2800, Kgs. Lyngby, Denmark
[2]Department of Electronics and Nanoengineering, Aalto University, P.O. Box 13500, FI-00076 Aalto, Finland
[3]Department of Physics, Technical University of Denmark, DK-2800, Kgs.
Lyngby, Denmark
[4]Capres A/S, Diplomvej 373, DK-2800 Kongens Lyngby, Denmark
[5]Faculty of Physics, Warsaw University of Technology, Koszykowa 75, 00-662 Warsaw, Poland
[6]Department of Photonic Engineering, Technical University of Denmark, DK-2800, Kgs.Lyngby, Denmark

*david.mackenzie@aalto.fi

Abstract
Micro four-point probes (M4PP) provide rapid and automated lithography-free transport properties of planar surfaces including two-dimensional materials. We perform sheet conductance wafer maps of graphene directly grown on a 100 mm SiC wafer using a multiplexed seven-point probe with minor additional measurement time compared to a four-point probe. Comparing the results of three subprobes we find that compared to a single-probe result, our measurement yield increases from 72-84% to 97%. The additional data allowed for uniformity analysis and subprobe variations revealed wafer homogeneity properties hidden by single-probe maps. Seven-point-probe maps tracked sheet conductance change over several weeks. Terahertz time-domain spectroscopy conductivity maps both before and after M4PP mapping showed no significant change due to M4PP measurement, with both methods showing the same qualitative changes over time.

Keywords: Graphene, SiC, Conductance, Micro four-point probe, Terahertz spectroscopy, Metrology, Mapping

Introduction

Graphene is an atomically-thin two-dimensional material [1]–[3] which has properties suitable for a large number of practical technologies from corrosion protection[4]–[6] to OLEDS[7]–[9] to sensors [10]–[12]. Now that the capability of large-scale growth[13]–[15], transfer [16]–[18], and lithography techniques [19], [20] of graphene are well established, methods for assessing the quality[21], [22] and homogeneity of wafer-scale graphene are required if the lab-proven graphene-based technologies will transition to commercial products. Ideally, these methods should not require any wafer dicing (so the characterized wafer can be further processed), or contact with liquids or polymers so to not change the properties of the material [23]. One automated electrical characterization method that meets these requirements are micro four-point probes (M4PP).

Methods

Graphene was grown on a four-inch silicon carbide wafer as described previously [24]. Electrical measurements were performed with a CAPRES microRSP-M300 using lock-in technique at 12 Hz, and with a current of 250 µA. In this work we have used a probe with seven nickel-coated electrodes as shown in Fig. 1 a. The right-hand-side of Fig. 1 a shows a strain gauge, which is used to control the contact force when the probe is engaged on the surface [25]. A low contact force and three-way

flexible electrodes [26], [27] are used to prevent unnecessary damage to the probe and surface. During a single engage of the probe to the surface, electrical measurements were performed in A-configuration, and then B-configuration as defined in Fig. 1 b-c, respectively. With seven electrodes available, we can select four electrodes of the seven to create a *subprobe*. The three subprobes used in this paper are shown in Fig. 1 e-g, where subprobes 1 and 2 have 10 µm electrode pitch and subprobe 3 has 20 µm electrode pitch. Subprobes 1 and 2 were chosen since they are the smallest possible subprobes with the least overlap. Subprobe 3 is the largest possible subprobe.

During each engage a total of 24 resistance measurements were performed (8 for each subprobe). These multiplexed measurements enabled a variety of error-checking measures to increase result accuracy as previously described [28]. Firstly, because the measurements were performed with lock-in technique, the phase of each individual measurement was assessed, and individual resistance measurements rejected if outside a set tolerance. The sheet resistance (R_S) is determined from the modified van der Pauw equation [29], [30] using resistance values measured in A configuration (R_A) and B configuration (R_B)

$$e^{\frac{2\pi R_A}{R_S}} - e^{\frac{2\pi R_B}{R_S}} = 1$$

All accepted sheet resistance values were then subjected to a median filter and the mean of the remaining sheet resistance values $\langle R_S \rangle$ which pass the filter gave a single sheet conductance $G_S = \langle R_S \rangle^{-1}$ value for the subprobe. If no $\langle R_S \rangle$ values pass the filters with the set tolerances, then we define the sheet conductance $G_S = 0$ in subsequent analysis and mapping. Probes were replaced automatically every 2000 engages. When subprobes are combined an additional median filter is applied. In this work our phase tolerance was 1°, and both median filter tolerances were 2%.

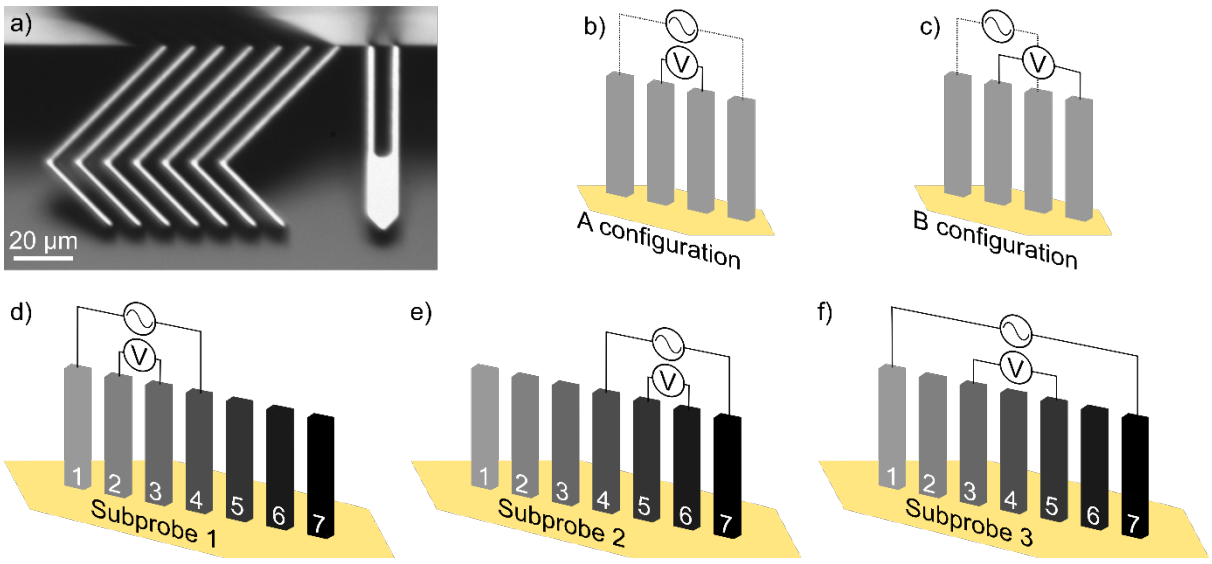

Fig 1. M4PP configurations and subprobes. a) Optical microscope image of the l-shaped cantilever-based seven-point-probe used for measurements equipped with strain gauge. b-c) Measurement configurations A and B. d) Subprobe 1 with 10 µm pitch. e) Subprobe 2 with 10 µm pitch. f) Subprobe 3 with 20 µm pitch.

Results and discussion

A wafer-scale G_S map performed with each of the three subprobes are shown in Fig. 2 (a-c) with a map combining the data from all three subprobes is shown in Fig. 2d. Previously, M4PP data from this wafer was compared with a THz-TDS conductance map [24]. Here, we compare G_S results obtained from different subprobes during the same probe engage. For a perfectly uniform material using multiple subprobes provides a redundancy in the measurement, in case of subprobe failure or localized sample defects. In either case, a measurement from of the other subprobes may be successful. For a non-uniform sample, multiple subprobe analysis can reveal the spatial and quantitative information about the extent of inhomogeneities.

Qualitatively, all the subprobe maps in Fig 2 a-c are similar, each having different regions where no G_S values passed the filters described in the methods section. The most prominent of these features appear as annulus sectors (circular ring sectors) and are attributed to subprobe failure as it matches the spiral-like measurement order. Thus, there is no reason to attribute these measurement failures to the local thin-film properties.

When G_S from the three subprobes are combined (Fig 2 d) all the null-G_S annulus sectors disappear. We then find that for this combined map only 385 out of 11,310 engages did not return an accepted G_S value (10,925 accepted, 97%). In contrast, the successful measurements for individual subprobes was 9528 (84% accepted), 9135 (81% accepted) and 8163 (72% accepted), for subprobe 1, subprobe 2, subprobe 3, respectively. For our measurements choosing more than one subprobe offered a level of measurement redundancy, with significant higher measurement yield from 72-84% to 97%.

Although some regions of the wafer have over an order of magnitude lower G_S, by studying the R_A/R_B ratio of the measurements (Fig S1), it can be concluded that this graphene does not exhibit any significant quasi 1D electrical behaviour.

Increasing the number of subprobes also increases the total measurement time. The time to measure one subprobe, disengage, move and reengage took approximately five seconds. Measurement time was increased by one second per additional subprobe. Three subprobes were chosen as a good compromise between measurement yield and measurement time.

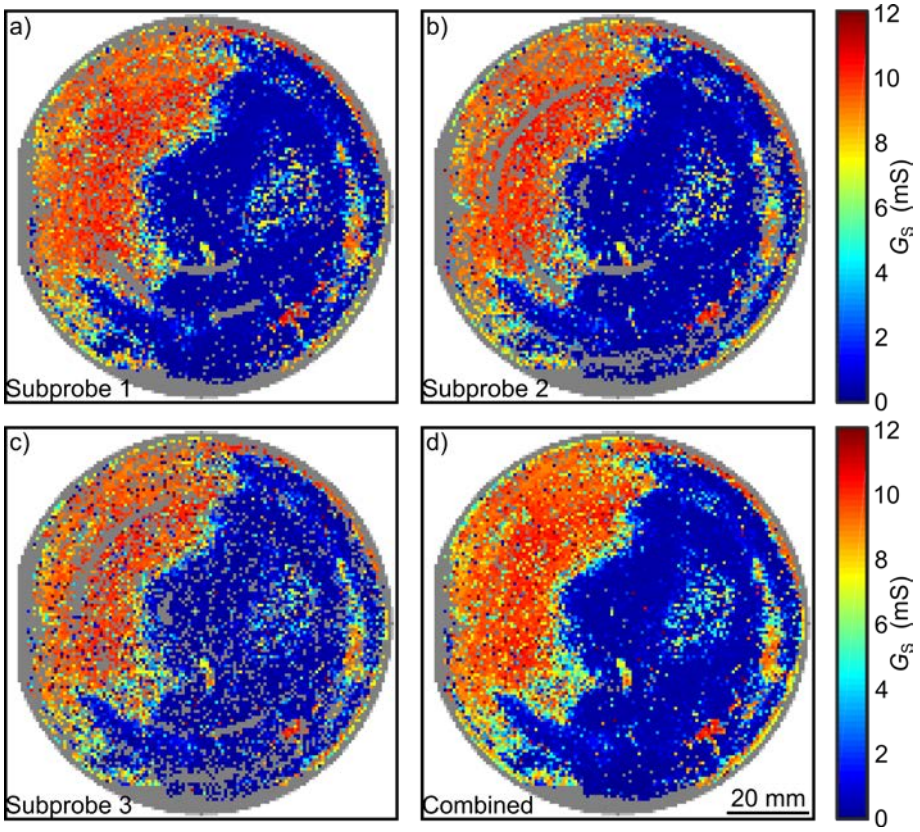

Figure 2. Conductance maps measured with M4PP. a) Subprobe 1 (10 µm pitch). b) Subprobe 2 (10 µm pitch). c) Subprobe 3 (20 µm pitch). d) Combination of data from subprobes from (a-c). Dead pixels/wafer outline shown in grey.

Multi-subprobe G_S maps can be a useful metrology tool for evaluating the variation in graphene quality across a wafer. With a wafer map of G_S enough data is available to perform analysis that would otherwise be impossible or imprecise with a linescan, reduced-area map, or single probe scan. For example, a comparison between G_S values for different subprobes can be compared to give an insight into homogeneity on the order of the probe length. Figure 3a shows a uniformity map of Fig 2d, which was calculated using the relative standard deviation of each pixel and its 15 nearest neighbours (uniformity maps for different number of nearest neighbours are shown in Fig S2). The single-subprobe uniformity maps for data from Fig 2 a-c are shown in Fig S3 a-c., where the lack of data coverage conceals many uniformity features. Homogeneity is known to be important for two-dimensional device performance[31], [32], so it is important to know if the entire wafer, or certain areas are suitable for device processing.

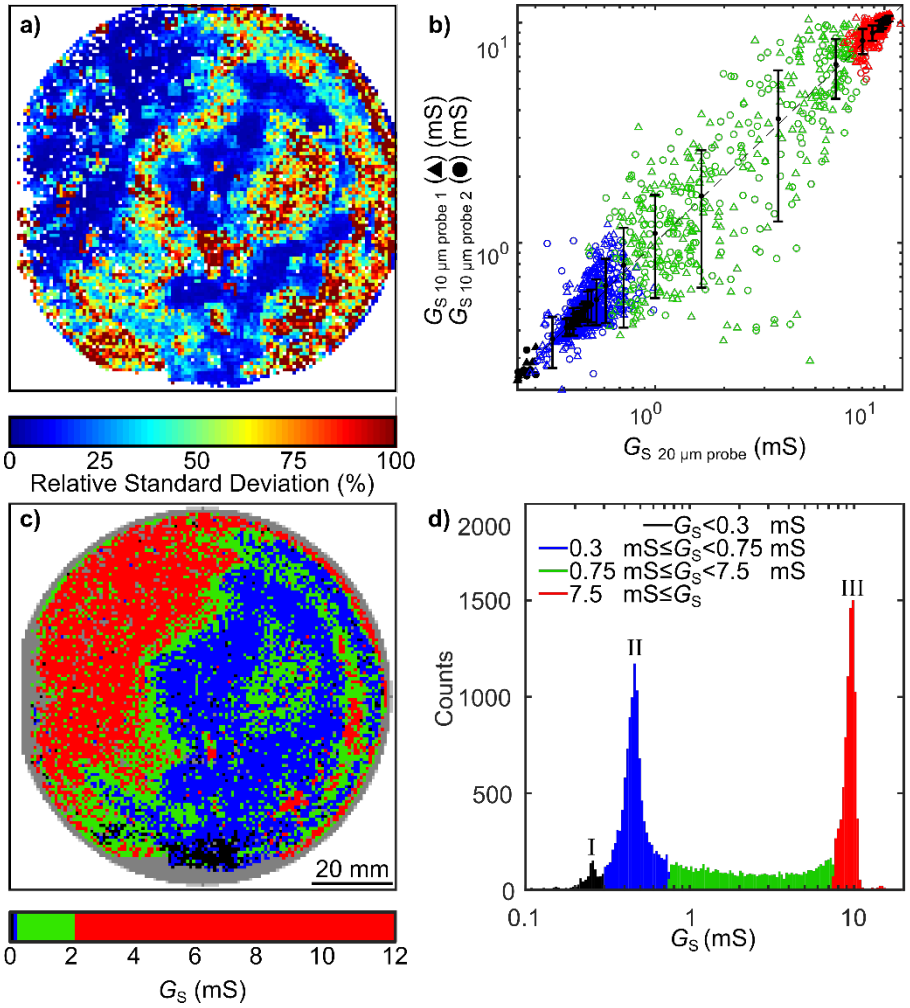

Figure 3. a) Uniformity map of data from Fig 2d showing the relative standard deviation of 15 nearest neighbours. b) Subprobe-to-subprobe correlation comparing subprobe 3 with subprobe 1 (triangles) and subprobe 2 (circiles). Four regions of G_S are defined by G_S < 0.3 mS (black region), 0.3 mS ≤ G_S<0.75 mS (blue region), 0.75 mS ≤ G_S<7.5 (green region), 7.5 mS ≤G_S (red region). c) Fig 2d

replotted in colourscale from Fig 3b. d) Histogram of the conductance as measured by all three subprobes with three peaks in the data I-III.

The subprobe-to-subprobe conductance correlation is shown in Fig 3b, where four regions are defined: G_S < 0.3 mS (black region), 0.3 mS ≤ G_S<0.75 mS (blue region), 0.75 mS ≤ G_S<7.5 (green region), 7.5 mS ≤G_S (red region). We observe good subprobe-to-subprobe agreement for high and low values of G_S, the blue and red regions, but poorer agreement in the green region. The fact the subprobe-to-subprobe error decreases again for the red region shows the subprobe-subprobe error is not simply proportional to the magnitude of G_S, and is likely an indication the green region has variations on the order of the probe length. When Fig 2b is replotted using the colourscale from Fig. 3b, we in fact do observe most of the green pixels as a transition area separating the regions of high and low values of G_S. Because the width of the transition areas are significantly larger than the size of the probe, it can be concluded this data represents a true variation in the sample G_S.

When the G_S data for all subprobes is plotted as a histogram three distinct peaks emerge, as shown in Fig. 3c, where the peaks are labelled I through III, and in addition between peak II and peak III a plateau in the data where the counts are roughly constant. Measurements representing the three peaks all originate from connected regions of graphene. The plateau between the second and third peak originates from measurements made in the transition area. Representing the data as a histogram allows for easy comparison of changes to the wafer over time.

G_S was also mapped at different times over several weeks using THz-TDS and M4PP, expanding on the work from [24]. After the maps shown above, a THz-TDS map of the wafer was performed, followed by an additional M4PP map, and then by a second THz-TDS map. Histogram analysis of the results are shown in Fig S4 and show that the two THz-TDS maps are almost identical, heavily suggesting that the intervening M4PP map has not made significant changes the sample. Overall, observe slightly higher G_S values in the M4PP map in comparison to both THz-TDS results, which is attributed to the fact that M4PP analyses G_S over micron-sized areas whereas THz-TDS at 1 THz probes over tens of nanometres [33]. We also note that peak I and II observed in Fig 3d have now combined as part of the change in G_S over time. The progression of wafer changes over nine weeks are shown in Fig. S5. The changes over time are quantitatively similar for both for both M4PP and THz-TDS showing that either method has the resolution required to track changes in graphene over time.

We have the following recommendations when mapping 2D materials with M4PP. Choosing to use a M4PP with greater than four probes allows for additional subprobe measurements while adding with negligible additional measurement time, allows a level of measurement redundancy for failed measurements, and allows insightful additional analysis. We have shown in Fig. 2 that a higher accuracy G_S, with less dead pixels was achieved by combining the data from subprobes into a single map. In addition, the combined map can be used *via* both uniformity assessment (e.g. Fig 3a) and subprobe-correlational assessment of G_S to determine spatial quality. The technique is sensitive enough to track changes in the graphene over time.

Conclusion

In summary, we have investigated wafer conductance maps of graphene using multiple subprobe M4PPs. Combining subprobes increased measurement yield from under 85% to 97% without adding significant measurement time. G_S varied across the wafer by over an order of magnitude, leading to local regions with different G_S landscapes. Producing wafer-scale analysis can be used to determine

overall growth quality, identify graphene areas which are suitable for further device processing, or to reject/accept an entire wafer. The M4PP map was compared to THz-TDS which showed qualitatively similar maps, even when the wafer changed over many weeks, further suggesting that M4PP produces accurate G_S data. THz-TDS conductivity maps performed before and after the M4PP mapping showed no decrease in conductivity attributable to the M4PP process.

Acknowledgements

The work has received funding from the European Union's Horizon 2020 research and innovation programme under grant agreement GrapheneCore2 785219 number. Centre for Nanostructured Graphene was supported by Danish National Research Foundation (project DNRF103 CNG) as well as H2020 European Project No. 692527.

Supplementary information:

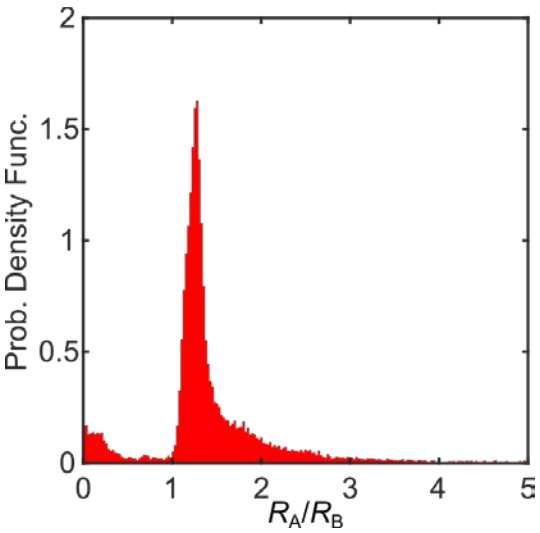

Figure S1. Histogram of the R_A/R_B ratio for the M4PP map shown in Fig 2d. The requirement for quasi 1D electrical behaviour is either a ratio of 0 or 1, which only a very small number of pixels have.

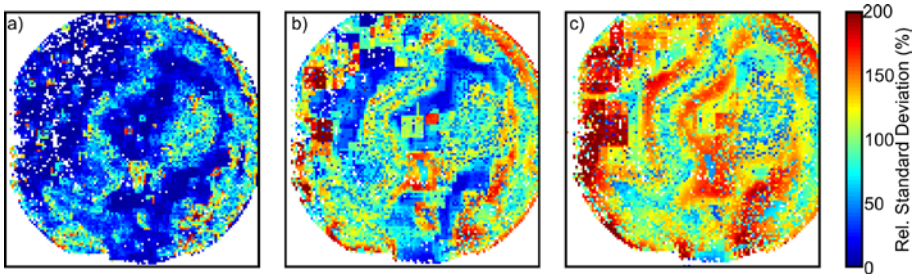

Figure S2. Uniformity maps showing relative standard deviation of local areas for regions for the combined map from Fig 2 d. a) 4 × 4 pixels. b) 10 × 10 pixels. c) 20 × 20 pixels.

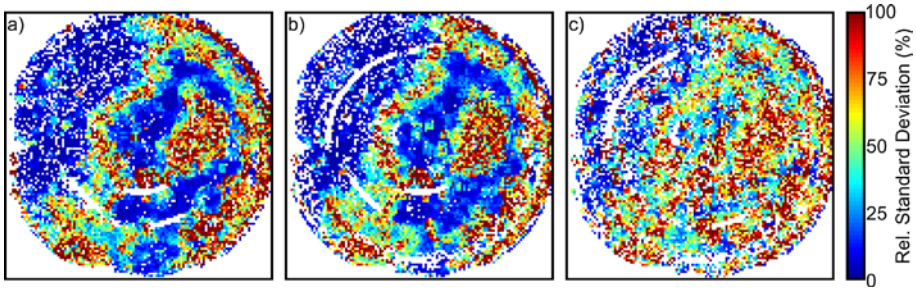

Figure S3: Uniformity Maps for 5 x 5 pixels for a) subprobes 1 (Fig 2a), b) subprobe 2 (Fig 2b), and c) subprobe 3 (Fig 2a).

Terahertz time-domain spectroscopy (THz-TDS) was performed using a Picometrix T-ray 4000 [34]. The spot size was ≈350 µm at 1 THz [35] and THz-TDS conductivity maps were acquired with a step size of 400 µm. The DC sheet conductance, σ_{THz}, was extracted by fitting the frequency-dependent sheet conductivity in the 0.4 - 1.1 THz range to the Drude model [35]–[37].

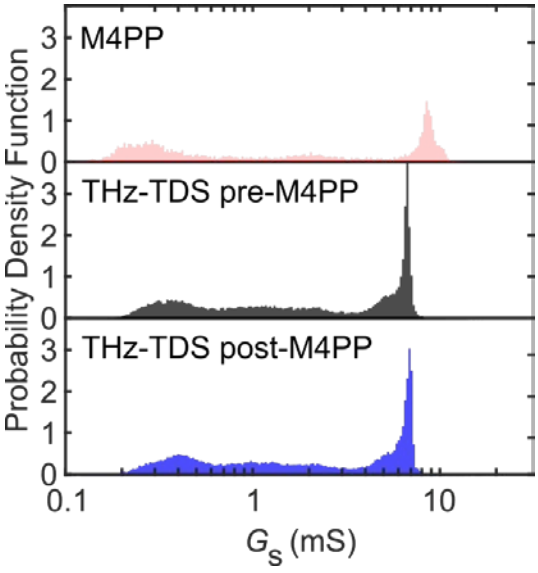

Figure S4. Histogram of three maps of the graphene wafer spaced with a week between each. The two THz-TDS maps, taken before and after the M4PP map, are almost identical.

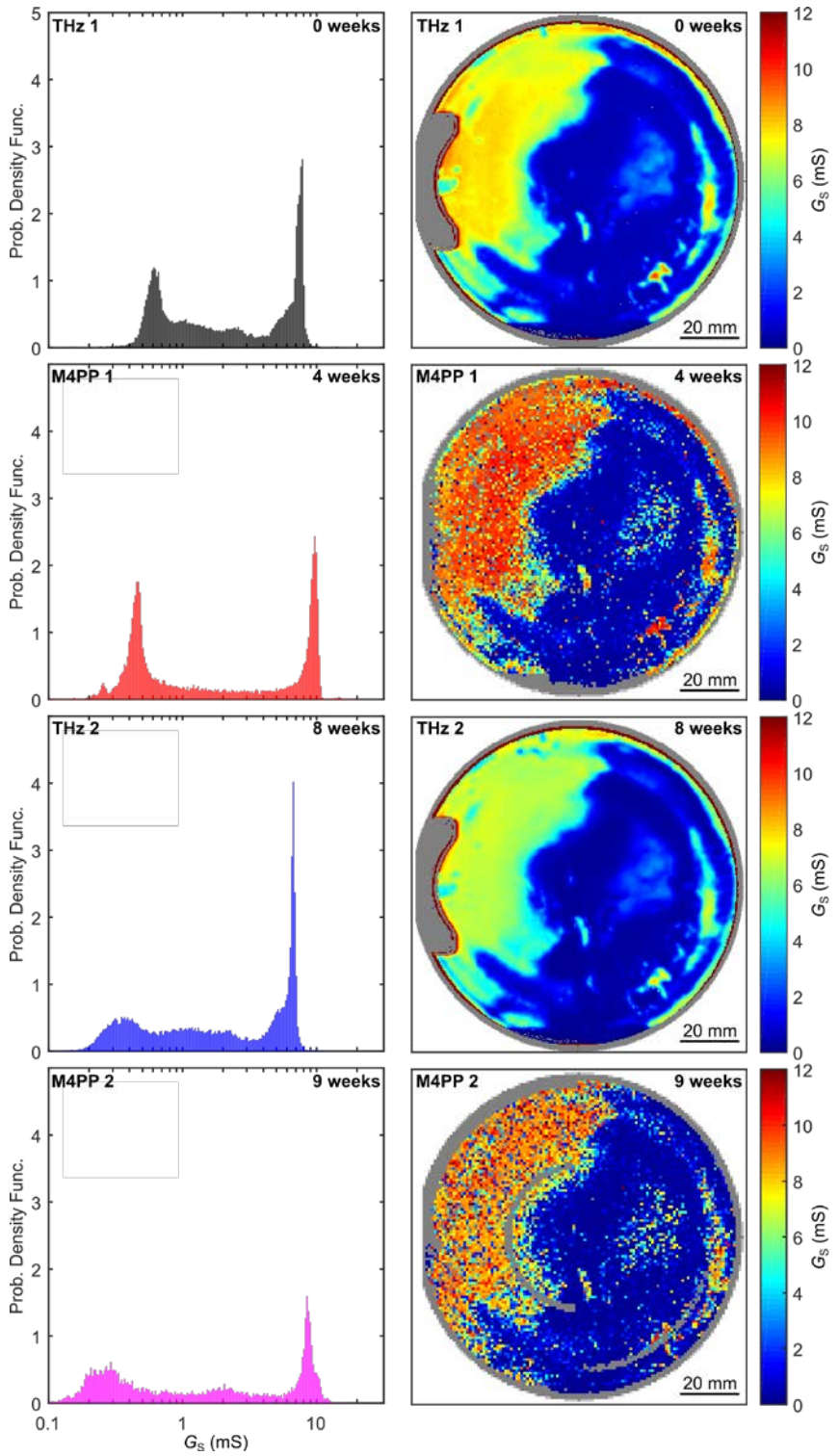

Figure S5. Showing the change in sheet conductance for the sample, measured with THz-TDS and M4PP. The measurements are ordered chronologically as they were measured. Each measurement has a time stamp indicating when they were measured compared to the first. Next to each histogram there is a spatial map of the conductance.

References

[1] K. S. Novoselov *et al.*, "Two-dimensional gas of massless Dirac fermions in graphene," *Nature*, vol. 438, no. 7065, pp. 197–200, 2005.

[2] K. S. Novoselov, “Nobel Lecture: Graphene: Materials in the Flatland,” *Rev. Mod. Phys.*, vol. 83, no. 3, pp. 837–849, 2011.

[3] P. Blake *et al.*, “Making graphene visible,” *Appl. Phys. Lett.*, vol. 91, no. 6, 2007.

[4] F. Yu *et al.*, “Complete long-term corrosion protection with chemical vapor deposited graphene,” *Carbon N. Y.*, vol. 132, pp. 78–84, 2018.

[5] N. T. Kirkland, T. Schiller, N. Medhekar, and N. Birbilis, “Exploring graphene as a corrosion protection barrier,” *Corros. Sci.*, vol. 56, pp. 1–4, 2012.

[6] M. Galbiati, A. C. Stoot, D. M. A. Mackenzie, P. Bøggild, and L. Camilli, “Real-time oxide evolution of copper protected by graphene and boron nitride barriers,” *Sci. Rep.*, vol. 7, no. 2, pp. 1–7, 2017.

[7] T.-H. Han *et al.*, “Extremely efficient flexible organic light-emitting diodes with modified graphene anode,” *Nat. Photonics*, vol. 6, no. 2, pp. 105–110, 2012.

[8] J. Wu *et al.*, “Organic Light-Emitting Diodes on Solution-Processed Graphene Transparent Electrodes,” *ACS Nano*, vol. 4, no. 1, pp. 43–48, 2010.

[9] T. Sun *et al.*, “Multilayered graphene used as anode of organic light emitting devices,” *Appl. Phys. Lett.*, vol. 96, no. 13, pp. 2008–2011, 2010.

[10] A. Cagliani, D. M. A. Mackenzie, L. K. Tschammer, F. Pizzocchero, K. Almdal, and P. Bøggild, “Large-area nanopatterned graphene for ultrasensitive gas sensing,” *Nano Res.*, vol. 7, no. 5, pp. 743–754, 2014.

[11] H. J. Yoon, D. H. Jun, J. H. Yang, Z. Zhou, S. S. Yang, and M. M. C. Cheng, “Carbon dioxide gas sensor using a graphene sheet,” *Sensors Actuators, B Chem.*, vol. 157, no. 1, pp. 310–313, 2011.

[12] K. K. Gopalan *et al.*, “Scalable and Tunable Periodic Graphene Nanohole Arrays for Mid-Infrared Plasmonics,” 2018.

[13] B. Luo *et al.*, “Sputtering an exterior metal coating on copper enclosure for large-scale growth of single-crystalline graphene,” *2D Mater.*, vol. 4, no. 4, p. 045017, 2017.

[14] V. Miseikis *et al.*, “Rapid CVD growth of millimetre-sized single crystal graphene using a cold-wall reactor,” *2D Mater.*, vol. 2, no. 1, 2015.

[15] K. S. Kim *et al.*, “Large-scale pattern growth of graphene films for stretchable transparent electrodes,” *Nature*, vol. 457, no. 7230, pp. 706–710, 2009.

[16] A. Shivayogimath *et al.*, “Do-It-Yourself Transfer of Large-Area Graphene Using an Offi ce Laminator and Water,” *Chem. Mater.*, vol. 31, no. 7, pp. 2328–2336, 2019.

[17] P. R. Whelan *et al.*, “Raman spectral indicators of catalyst decoupling for transfer of CVD grown 2D materials,” *Carbon N. Y.*, vol. 117, pp. 75–81, 2017.

[18] A. Shivayogimath *et al.*, “Atomic Layer Deposition Alumina-Mediated Graphene Transfer for Reduced Process Contamination,” *Phys. status solidi – Rapid Res. Lett.*, vol. 1900424, p. 1900424, 2019.

[19] D. M. A. Mackenzie *et al.*, “Batch fabrication of nanopatterned graphene devices via nanoimprint lithography,” *Appl. Phys. Lett.*, vol. 111, no. 193103, 2017.

[20] D. M. A. Mackenzie *et al.*, “Fabrication of CVD graphene-based devices via laser ablation for wafer-scale characterization,” *2D Mater.*, vol. 2, no. 4, 2015.

[21] P. Bøggild *et al.*, “Mapping the electrical properties of large-area graphene,” *2D Mater.*, vol. 4, no. 4, p. 042003, 2017.

[22] B. S. Jessen *et al.*, “Quantitative optical mapping of two-dimensional materials,” pp. 1–23.

[23] L. Gammelgaard *et al.*, “Graphene transport properties upon exposure to PMMA processing and heat treatments,” *2D Mater.*, vol. 1, no. 3, 2014.

[24] P. R. Whelan *et al.*, “Electrical homogeneity mapping of epitaxial graphene on silicon carbide,” *ACS Appl. Mater. Interfaces*, p. acsami.8b11428, 2018.

[25] D. H. Petersen *et al.*, “Review of electrical characterization of ultra-shallow junctions with micro four-point probes,” *J. Vac. Sci. Technol. B, Nanotechnol. Microelectron. Mater. Process. Meas. Phenom.*, vol. 28, no. 1, p. C1C27-C1C33, Jan. 2010.

[26] K. G. Kalhauge, H. H. Henrichsen, and F. Wang, “Vibration tolerance of micro-electrodes,” 2018.

[27] F. Wang *et al.*, “Three-way flexible cantilever probes for static contact,” *J. Micromechanics Microengineering*, vol. 21, no. 8, 2011.

[28] D. H. Petersen, “Micro Four-Point Probe and Micro Hall Effect - Methods for Reliable Electrical Characterization of Ultra-Shallow Junctions,” 2009.

[29] R. Rymaszewski, “Relationship between the correction factor of the four-point probe value and the selection of potential and current electrodes,” *J. Phys. E.*, vol. 2, no. 2, pp. 170–174, 1969.

[30] S. Thorsteinsson *et al.*, “Accurate microfour-point probe sheet resistance measurements on small samples,” *Rev. Sci. Instrum.*, vol. 80, no. 5, 2009.

[31] D. M. A. Mackenzie *et al.*, “Quality assessment of graphene: Continuity, uniformity, and accuracy of mobility measurements,” *Nano Res.*, vol. 10, no. 10, pp. 3596–3605, 2017.

[32] N. Kaushik *et al.*, “Reversible hysteresis inversion in MoS2 field effect transistors,” *npj 2D Mater. Appl.*, vol. 1, no. 1, p. 34, 2017.

[33] P. Bøggild *et al.*, “Mapping the electrical properties of large-area graphene,” *2D Mater.*, vol. 4, no. 4, 2017.

[34] J. D. Buron *et al.*, “Graphene conductance uniformity mapping,” *Nano Lett.*, vol. 12, no. 10, pp. 5074–5081, 2012.

[35] J. D. Buron *et al.*, “Terahertz wafer-scale mobility mapping of graphene on insulating substrates without a gate,” *Opt. Express*, vol. 23, no. 24, p. 30721, 2015.

[36] P. R. Whelan *et al.*, “Conductivity mapping of graphene on polymeric films by terahertz time-domain spectroscopy,” *Opt. Express*, vol. 26, no. 14, pp. 17748–17754, 2018.

[37] P. R. Whelan *et al.*, “Electrical Homogeneity Mapping of Epitaxial Graphene on Silicon Carbide,” 2018.

Paper 4

To be submitted to J. Micromech. Microeng.

PhD Student Contribution: Theory, calculations, graphics and main writter.
Experiments performed by Asger K. Pedersen.

Vibration Tolerant Two-Beam Cantilevers for Small Pitch Micro-Electrodes

Kristoffer G. Kalhauge[1], Asger K. Pedersen[1], Jesper Y. Pan[2], Nicolai A. Michaelsen[3], Ole Hansen[2] and Dirch H. Petersen[1]

[1] Department of Physics, Technical University of Denmark, Fysikvej Building 311, DK-2800 Kgs Lyngby, Denmark

[2] DTU Nanolab, National Centre for Nano Fabrication and Characterization, Technical University of Denmark, Oersteds Plads Building 347, DK-2800 Kgs Lyngby, Denmark

[3] CAPRES, Scion-DTU, Building 373, DK-2800 Kgs Lyngby, Denmark

Abstract

Micro four-point measurements on advanced materials are often dependent on the electrode pitch of the micro four-point probe used. In some cases the electrode pitch can determine if it is possible to measure the sample at all. Reasons ranging from loss of confinement of the current, to the probe being too large to land on the sample itself. Thus, a small absolute value of the probe pitch is often necessary; unfortunately, probes with small pitch are very sensitive to dynamic position errors. To counteract the high sensitivity to dynamic position errors, probes with built-in vibration tolerance can significantly reduce the frequency of dynamic position error incidents. Here we discuss a method for optimizing probe design for maximum vibration tolerance in the case where the electrodes on the probe consist of two rectangular beams connected at an arbitrary angle. We used the method to study the effect of design variations on the vibration tolerance. We show that there are two effective design schemes; one for probes with a pitch below $2\sqrt{2}$ times the minimum feature size, and another one for probes with larger pitch.

1 Introduction

Four-point probe (4PP) measurements were first described more than a century ago [1], and has since become a preferred method for characterization of electronic material properties [2–4]. In the semiconductor industry, where material dimensions continuously decrease [5], the size of the traditional 4PP with millimeter electrode pitch has become a problem which has been solved by application of micro four-point probes (M4PP) with micron sized electrode pitch [6–10]. The M4PP was first introduced to achieve high surface sensitivity [11] and high spatial resolution [12]. The individual electrodes were straight cantilevers typically consisting of silicon dioxide [12], polysilicon [13] or polymer cantilevers [14] with a thin conductive metal coating (e.g., Au or Ni). The cantilevers may also be made completely out of metal [15].

M4PP measurements have now developed into a fully automated process. Using configuration switching and lock-in amplification, sheet resistance [16] and Hall effect [17,18] can be measured on micron-scale scribe-line test pads. Combining M4PP measurements with advanced data treatment algorithms [19,20] have made M4PP the most reliable method for electrical characterization of ultra-thin materials during the last decade [9, 10, 21, 22].

In order to achieve high precision results with M4PP, the electrode contacts must remain stationary during a complete measurement. Depending on the measurement type this may be a few seconds [23]. Movement of the electrodes during a measurement will lead to dynamic position errors which affects the measurement precision through incorrect application of geometrical correction algorithms [19, 24–26]. As a result, vibration tolerant electrode designs [27] have been introduced based on three-way flexible electrodes [13, 28]. These electrodes consist of two beams connected at a right angle [13,28]. While being highly vibrational tolerant [27], this design limits the minimum possible electrode pitch.

In this article, we look at hybrid electrode designs that combine the small electrode pitch of the straight cantilever with the vibration tolerance of three-way flexible electrodes. This type of cantilever have been presented before [19] but the mechanical behaviour has not been described. We look for the best possible vibration tolerances as function of electrode pitch. In order to do this, a theoretical expression is derived for the compliance tensor of a cantilever consisting of two beams joint at an arbitrary angle.

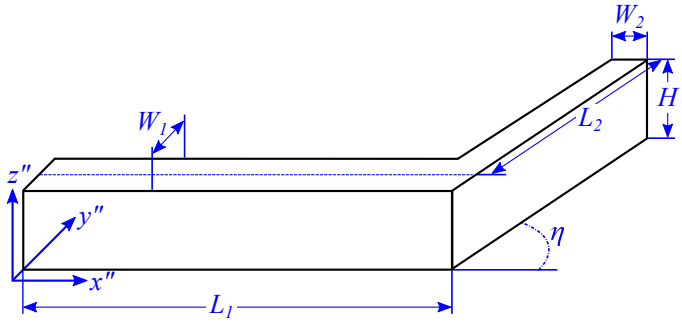

Figure 1: Sketch of the dimensions of a two beam cantilever. Basis for cantilever coordinate system is shown on the left side of the cantilever.

2 Theory

The cantilevers considered in this paper consist of two rectangular beams connected at an angle η. Here they will be referred to as two-beam cantilevers. The beams have lengths L_1 and L_2 and widths W_1 and W_2 for the first and second beam respectively. Both beams have the same height of H. The first beam is clamped at one end and connected to the second beam at the other. The second beam has one end connected to the first beam and the other end is free. A sketch of a two-beam cantilever is shown in Figure 1.

The mechanical behaviour of the cantilevers can be described using Hooke's law generalized to three dimensions. So that the deflection vector, $\boldsymbol{\delta}$, of a cantilever can be described as the compliance tensor, $[\mathbf{C}]$, multiplied with the force vector, $\mathbf{F}$, $\boldsymbol{\delta} = [\mathbf{C}]\mathbf{F}$. The inverse relation can also be defined using the stiffness tensor $[\mathbf{K}] = [\mathbf{C}]^{-1}$, $\mathbf{F} = [\mathbf{K}]\boldsymbol{\delta}$, as also discussed by Wang et al. [28].

To describe the cantilevers, two Cartesian coordinate systems are used. The cantilever coordinate system, $O - x''y''z''$, defined so that x'' points along the direction of the first beam, while y'' is in the plane in which the cantilever bends. The coordinate system is shown in Figure 1. The sample coordinate system, $O - xyz$, is rotated the angle ϕ around the y''-axis and θ around the z''-axis. These angles represent the angle with which the probe is tilted compared to the sample and the angle between the probe body and the first beam of the cantilever, respectively.

The rotation from cantilever coordinates $O - x''y''z''$ to sample coordinates $O - xyz$ can be described using the rotation matrix $[\mathbf{T}]$.

$$[\mathbf{T}] = \begin{bmatrix} \cos\theta\cos\phi & -\sin\theta\cos\phi & -\cos\theta\sin\phi \\ \sin\theta\cos\phi & \cos\theta & -\sin\theta\sin\phi \\ \sin\phi & 0 & \cos\phi \end{bmatrix} \tag{1}$$

So that $[\mathbf{C}] = [\mathbf{T}^{-1}][\mathbf{C}''][\mathbf{T}]$ [28].

2.1 Compliance Tensor

In the expression presented here it will be assumed that the cantilevers are made from an isotropic material with Young's modulus E and Poisson's ratio ν. Derivation of the compliance elements in the cantilever coordinates is in Appendix I.

Taking both bending and elongation of the cantilever into account, the compliance tensor elements for a two-beam cantilever become.

$$C''_{xx} = \frac{4L_1^3}{EH^4}\left(\frac{\gamma^3}{\alpha^3} + 3\frac{\beta^3}{\alpha^3}\right)\sin^2\eta + \frac{L_1}{EH^2}\left(\beta + \frac{\gamma}{\alpha}\cos^2\eta\right)$$

$$C''_{yy} = \frac{4L_1^3}{EH^4}\left(\beta^3 + 3\frac{\beta^3}{\alpha}\cos\eta + \left[3\frac{\beta^3}{\alpha^2} + \frac{\gamma^3}{\alpha^3}\right]\cos^2\eta\right) + \frac{L_1}{EH^2}\frac{\gamma}{\alpha}\sin^2\eta$$

$$C''_{zz} = \frac{4L_1^3}{EH^4}\left(\beta + 3\frac{\beta}{\alpha}\cos\eta + 3\frac{\beta}{\alpha^2}\cos^2\eta + \frac{\gamma}{\alpha^3} + \frac{\beta^3}{\alpha^2}\frac{1+\nu}{2k_\beta}\sin^2\eta\right)$$

$$C''_{xy} = -\frac{4L_1^3}{EH^4}\left(\frac{3}{2}\frac{\beta^3}{\alpha} + \left[3\frac{\beta^3}{\alpha^2} + \frac{\gamma^3}{\alpha^3}\right]\cos\eta\right)\sin\eta + \frac{L_1}{EH^2}\frac{\gamma}{\alpha}\cos\eta\sin\eta$$

$$C''_{yx} = C''_{xy}$$

$$C''_{xz} = C''_{zx} = 0$$

$$C''_{yz} = C''_{zy} = 0 \tag{2}$$

where $\alpha \equiv L_1/L_2$, $\beta \equiv H/W_1$ and $\gamma \equiv H/W_2$. k_β is a constant that describes the deflection from the torsion of the first beam, given by a sum over all odd natural numbers:

$$k_\beta = \frac{1}{3} - \frac{64}{\pi^5\beta}\sum_{n=1,3,5}^{\infty}\frac{1}{n^5}\tanh\frac{n\pi\beta}{2}, \tag{3}$$

which is valid as long as $\beta > 1$ [29].

2.2 Static and Sliding Contact

Two types of contact can be made between the cantilever tip and the sample, i.e. sliding and static contact.

Static contact is defined by the cantilever remaining stationary on the sample during engagement because the friction force exceeds the transverse forces. In this situation, of zero transverse displacement of the cantilever tip i.e. $\boldsymbol{\delta} = \delta_z\hat{z}$, the related force becomes

$$\mathbf{F} = \begin{bmatrix} K_{xz} \\ K_{yz} \\ K_{zz} \end{bmatrix}\delta_z. \tag{4}$$

Consequently the criterion to the static friction coefficient, to form a static contact, is given by [13]

$$\mu_S \geq \sqrt{\frac{K_{xz}^2 + K_{yz}^2}{K_{zz}^2}}, \tag{5}$$

where μ_S is the static friction coefficient.

Sliding contact represents the other extreme, where the cantilever tip during engagement slides over the surface until zero transverse force is achieved. Mathematically this scenario requires $\mathbf{F} = F_z\hat{z}$. The normal force is then related to engage depth by

$$F_z = C_{zz}^{-1}\delta_z. \tag{6}$$

2.3 Transition Between Static and Sliding Contact

Pure sliding contact only happens when the kinematic friction coefficient is zero, which is mostly unrealistic. However, sliding is a good assumption if either the kinematic friction coefficient is very low or if the angle η is small, equivalent to a straight cantilever. In both of these cases the cantilever tip will end very close to the zero transverse force point.

Most cantilevers will behave somewhere between static and sliding contact; during engagement, the cantilever tip slides across the surface until the friction exceeds the transverse forces. If the engage depth is increased further, the cantilever tip will remain stationary until the transverse forces exceeds the friction again, at which point it will jump to the next stable point and get stuck again. This type of contact is known as stick-slip.

In Appendix II an experiment using 3D-printed cantilevers is discussed; here the normal force during an engagement was measured as a function of engage depth. The experiment was performed with 3 cantilevers: a straight cantilever with sliding contact, a bent cantilever with static contact and a bent cantilever with a stick-slip contact.

Equation (7) describes the largest deflection that a static contact, after pure sliding, can maintain without moving. This equation shows that the necessary deflection is proportional with the engage depth. The deeper the engage is, the larger the necessary deflection has to be to move the cantilever tip [30]. This proportionality is also seen in the stick-slip experiment, where the "sawtooth" become longer when the engage depth is increased. The experiment indicates that a stick-slip contact will on average behave like a sliding contact.

2.4 Vibration tolerance

Due to friction between the cantilever tip and the sample, the cantilever tip will be able to withstand some vibrations before moving. The vibration tolerance describes the necessary lateral vibration magnitude in order to move the cantilever tip-sample contact point. A measure for the vibration tolerance, Γ, was derived in [27]

$$\frac{A}{\delta_z} \leq \frac{\mu C_{zz}^{-1}}{K_T(\psi) + \mu|K_N(\psi)|} \equiv \Gamma(\psi), \tag{7}$$

where ψ is the angle of attack for a vibration in the sample plane and A is the lateral vibration magnitude. Here $K_N(\psi)$ and $K_T(\psi)$ are the effective normal and transverse spring constants, given by

$$K_N(\psi) = K_{zx}\cos\psi + K_{zy}\sin\psi \tag{8}$$

$$K_T(\psi) = \Big[(K_{xx}\cos\psi + K_{xy}\sin\psi)^2 + (K_{yx}\cos\psi + K_{yy}\sin\psi)^2\Big]^{1/2} \tag{9}$$

To compare individual cantilever designs, the minimum vibration tolerance is used to represent a measure of the worst case vibration tolerance, i.e.,

$$\Gamma = \min_{\psi\in[-\pi,\pi]} \Gamma(\psi). \tag{10}$$

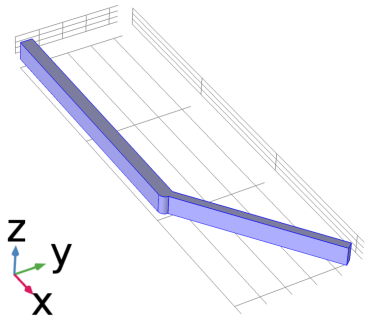

Figure 2: Model geometry used in finite element modelling using COMSOL 5.2a, to simulate the compliance tensor of the cantilever.

3 Simulation

In order to validate accuracy of the calculated compliance elements, finite element modelling of the cantilevers was done in COMSOL 5.2a [31] using the Solid Mechanics module.

The model geometry consists of two beams connected to each other at the centre points of their respective ends. In order to ensure that cantilever of arbitrary angles and dimensions can be simulated, a hinge between the two beams was introduced. The hinge consists of two semicircles each connected to the end of a beam with a diameter equal to the respective beam width. The model geometry of a cantilever with $\eta = 37°$ is shown in Figure 2. The model was clamped

in one end while a point force was applied at the tip of the cantilever.

Each compliance element was then found by applying a force in either $\hat{x}''$, $\hat{y}''$ or $\hat{z}''$ and extracting the resulting deflection in $\hat{x}''$, $\hat{y}''$ or $\hat{z}''$, e.g. element C''_{xy} is found by applying a force in the $\hat{y}''$ direction and extracting the deflection in the $\hat{x}''$ direction. The deflection is then divided by the magnitude of the force to get the compliance element. The model will be used to validate the results in Section 5.2.

4 Vibration Tolerance Vs. Electrode Pitch

This study, of the effect of the electrode pitch on the vibration tolerance, is based on the silicon dioxide cantilever design presented in Cagliani et al. [19], which is used as a base line for comparison. The new designs uses the total length ($L_T = 12.2$ µm), engage stiffness ($C_{zz}^{-1} = 13.1$ N/m) and minimum feature size ($d = 0.5$ µm) from the cantilever design in [19]. The total cantilever length is given by

$$L_T = L_1 \cos\theta + L_2 \cos(\eta - \theta). \tag{11}$$

Finally, the gap between two neighbouring cantilevers in a probe must be at least the minimum feature size, this condition can be expressed as

$$\begin{aligned} \sigma\cos\theta - W_1/d &\geq 1 \\ \sigma\cos(\eta-\theta) - W_2/d &\geq 1 \end{aligned} \tag{12}$$

where σ is the dimensionless electrode pitch, given by the electrode pitch divided by d.

To identify the optimal design at each value of the normalized electrode pitch, a brute force based optimization was used. This method is based on calculating all permutations of the design parameters and then choosing the best. However, some limits on the parameter space were introduced to improve calculation speed and precision, these are described in Appendix III.

Of the nine parameters (θ, η, ϕ, α, L_T, H, W_1, W_2 and C_{zz}^{-1}) necessary to describe the problem, three were kept constant (ϕ, L_T and C_{zz}^{-1}), one always resulted in the same value (W_2) while the remaining five (θ, η, α, H and W_1) were variable. The results will be evaluated in Section 5.2.

5 Results and Discussion

5.1 Generalized Observations

To form a general idea of how each geometric parameter affects the vibration tolerance of the cantilever, the vibration tolerance was plotted as a function of the three dimensionless parameters α, β and γ as well as the angles θ and η. The plots are shown in Figure 3. In the plots, a cantilever height of $H = 2$ µm was used. The length of the first beam, L_1, was adjusted for each data point to make the engage stiffness, C_{zz}^{-1}, constant at 10 ± 0.1 N/m. The cantilever is assumed to be tilted at an angle of $\phi = 30°$ and made of SiO_2, with a Young's modulus of $E = 69$ GPa and a Poisson's ratio of $\nu = 0.17$ [32].

Figure 3 shows that increasing γ (corresponding to decreasing W_2) increases the vibration tolerance. It appears as a general rule that minimizing W_2 always results in a larger vibration tolerance. The effect of changing β (corresponding to changing W_1) is less straightforward. Generally, increasing β increases the range of α-values that leads to a large vibration tolerance. A high value of β combined with a small value of γ results in a larger vibration tolerance compared to cases where both β and γ are small. However, when both β and γ are high the vibration tolerance is smaller than when β is small while γ is high. In other words the optimal value of β depends heavily on the choice of parameter values. From Figure 3 it is also evident that increasing the angles θ and η also increases the vibration tolerance. Except when the angles are allowed to be very large ($\theta \approx 60°$ and $\eta \approx 130°$).

5.2 Design Optimization

The normalized vibration tolerance of the optimized designs is shown in Figure 4 as function of the normalized electrode pitch σ. Since the electrode pitch needs to include both the gap between cantilevers and the width of the beams, it must be at least two minimum feature sizes. The dimensionless vibration tolerance is in percent of the engage depth. The results of simulating the same designs using finite element modelling is shown in the same plot. In general, the analytical and numerical results are in excellent agreement, with an average relative difference (Numerical/Analytical - 1) of 3%. The resulting angles for the optimized designs are shown in Figure 5.

For $\sigma \in [2, 2\sqrt{2}]$ the design freedom is severely limited by the gap between the cantilevers. The most efficient change to the cantilever design in this interval is to maximize the angles θ and η. Since L_T is kept constant and the angles are increasing, the individual lengths (L_1 and L_2) must necessarily increase. However, α (L_1/L_2) also increases, in this interval of σ, i.e. from $\alpha \in [1.5, 2.3]$. H/d, the height in units of minimum feature size, is increased linearly from 2.6 to 8.2 in order to maintain an engage stiffness of 13.1 N/m. At $\sigma = 2\sqrt{2}$ it is possible to make a cantilever with $\theta = 45°$ and $\eta = 90°$.

Beyond $\sigma = 2\sqrt{2}$, α and H is kept roughly constant while

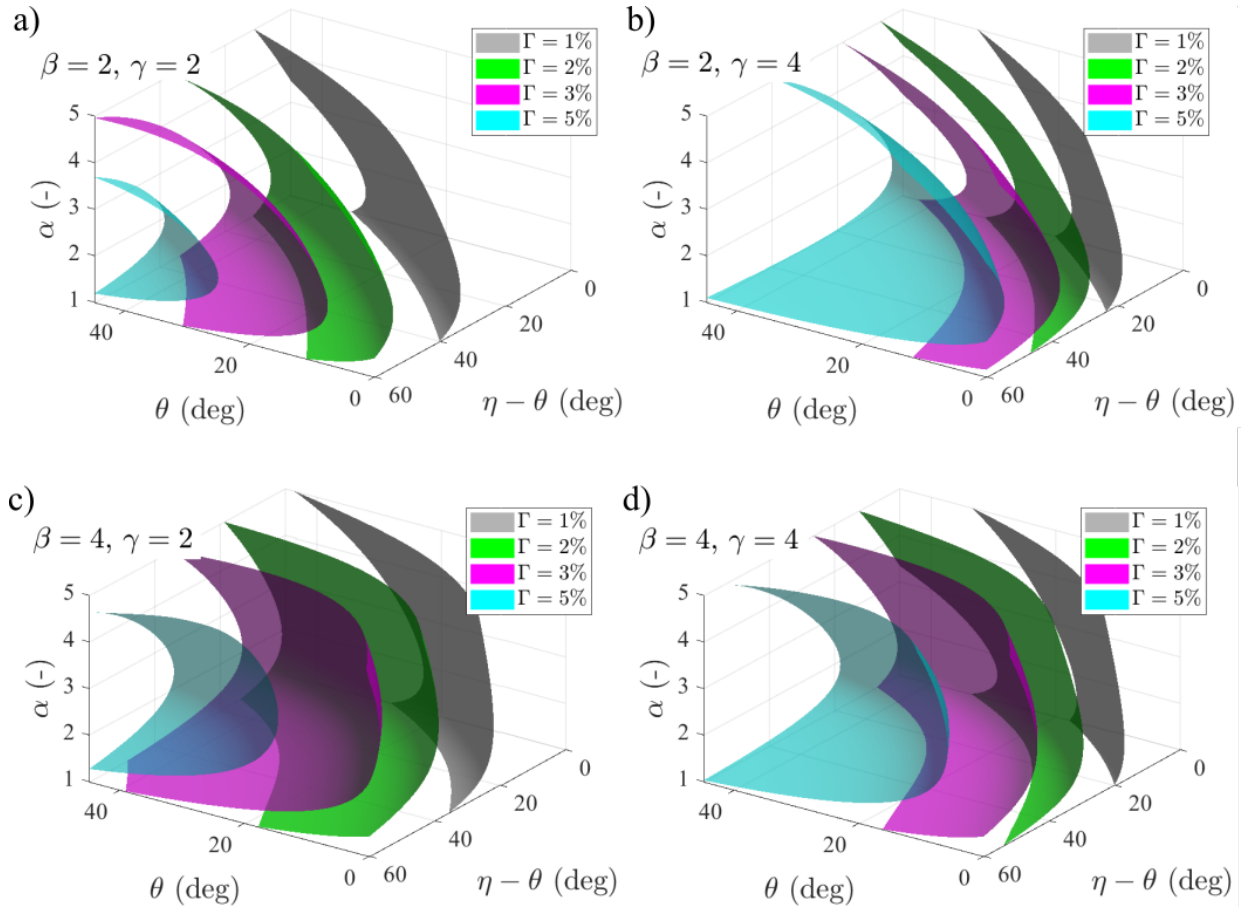

Figure 3: Shell plots of the vibration tolerance for two-beam cantilevers. Each shell represents the design surface that results in the given vibration tolerance. The height and engage stiffness of the cantilever designs were kept constant at 2 µm and 10 N/m respectively. Each plot shows the effect of changing α, θ and η while β and γ is changed between plots.

σ increases. At the same time the angles θ and η keep increasing. However, since the height is constant, W_1 has to increase in order to maintain an engage stiffness of 13.1 N/m. This limits the growth of θ, since

$$\theta \leq \arccos\left(\frac{W_1/d + 1}{\sigma}\right). \tag{13}$$

In Figure 5 this appears as a splitting of the θ and $\eta - \theta$ curves.

This behaviour continues until $\sigma \approx 6.7$. Based on the calculations made as a part of this work, the exact value of σ depends on the total length and engage stiffness, with observed values ranging from 6 to 7. After σ has reached this value the design is not changing any more.

6 Conclusion

An expression for the compliance tensor for two-beam cantilevers of arbitrary angle was derived. This expression was used to study the effect of design parameters on the vibration tolerance of a cantilever. From this study we learned that the design freedoms depends on the electrode pitch, with significant differences between cases $\sigma < 2\sqrt{2}$ and where $\sigma > 2\sqrt{2}$. Thus two procedures for optimizing the vibration tolerance were developed.

Optimization of the vibration tolerance of a cantilever when $\sigma < 2\sqrt{2}$ involves the following steps. First the width of both beams (W_1 and W_2) are minimized. The two angles, θ and η are then maximized. Finally the lengths of the beams (L_1 and L_2) as well as the height (H) is adjusted to achieve the target stiffness. In the adjustment, it can be utilized that $C_{zz}^{-1} \propto H^4/L_1^3$.

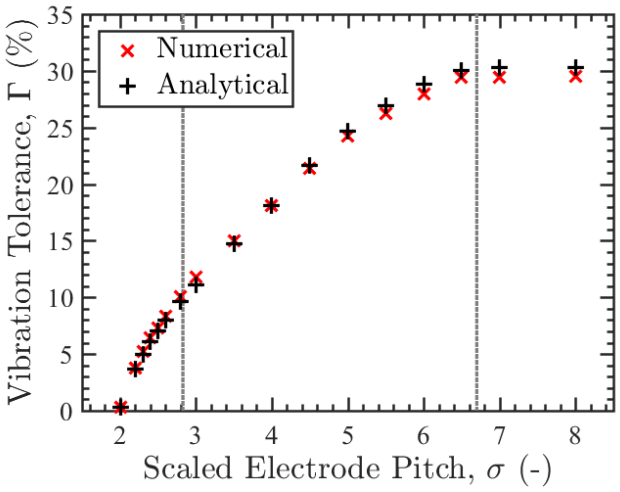

Figure 4: The maximum achievable vibration tolerance for a cantilever, with an engage stiffness of $C_{zz}^{-1} = 13.1$ N/m, a minimum feature size of 0.5 µm and a total length of $L_T = 12.2$ µm, as a function of the electrode pitch in units of minimum feature size. The gray dotted lines are at $\sigma = 2\sqrt{2}$ and $\sigma = 6.7$.

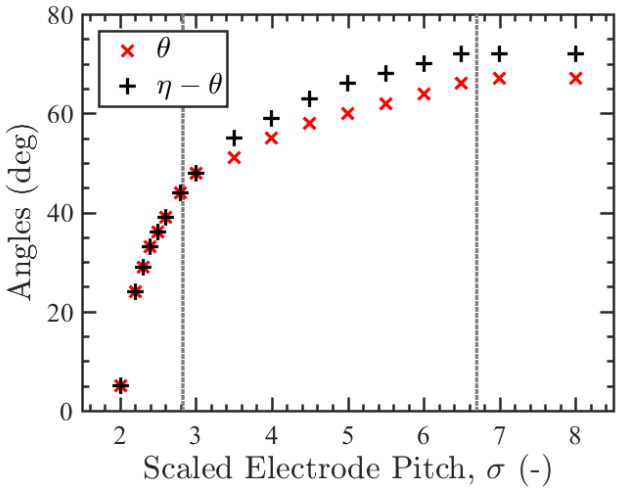

Figure 5: The angles θ and η as a function of the electrode pitch, for the cantilever designs with the largest vibration tolerance. The cantilevers have an engage stiffness of $C_{zz}^{-1} = 13.1$ N/m, a minimum feature size of 0.5 µm and a total length of $L_T = 12.2$ µm. The gray dotted lines are at $\sigma = 2\sqrt{2}$ and $\sigma = 6.7$.

If $\sigma > 2\sqrt{2}$ the optimization process is different. In this case the first step is still to minimize the width of the second beam (W_2). Afterwards, find the width of the first beam (W_1) and angle to the probe body θ that results in the largest vibration tolerance, utilizing that $\theta = \arccos([W_1/d + 1]/\sigma)$ and that $\eta = \arccos(2/\sigma) + \theta$. Simultaneously the beam lengths (L_1 and L_2) and height (H) is adjusted to achieve the target stiffness.

Acknowledgements

The authors are thankful for financial support from Innovation Fund Denmark project no. 8057-00010A and Independent Research Fund Denmark project no. 8048-00088B.

The authors also like to thank Lior Shiv and Lauge Gammelgaard for fruitful discussions on cantilever design and optimization.

Appendix I

In this appendix the derivation of the compliance matrix is shown in detail. It is assumed that both beams follow the Euler-Bernoulli beam differential equations (EB-equation), and elongation and compression are included. In order to derive the Compliance elements four moments of inertia are needed. For the rotation of beam 1 (B1) and beam 2 (B2) around the z''-axis, the rotation of B1 around the y''-axis and lastly the rotation of B2 around an axis orthogonal to B2 that lies in the $x''y''$-plane.

$$I_{z''1} = \frac{W_1^3 H}{12}, \qquad I_{z''2} = \frac{W_2^3 H}{12}$$
$$I_1 = \frac{W_1 H^3}{12}, \qquad I_2 = \frac{W_2 H^3}{12}$$

Force in the x''-direction

A force applied in the x''-direction will give rise to a constant shear force in B2, $V_2 = F_{x''} \sin\eta$. This shear force will result in a constant bending moment $M_1 = F_{x''} L_2 \sin\eta$ in B1 and the linear bending moment $M_2 = F_{x''}(L_2 - \ell)\sin\eta$ in B2, where ℓ indicates position on B2.

The EB-equation is first solved for B1,

$$\frac{\mathrm{d}^2}{\mathrm{d}x''^2}\delta''(x'') = -\frac{M_1}{EI_{z''1}} \quad \Big| \quad \text{BC:} \quad \begin{aligned} \delta''(0) &= 0 \\ \tfrac{\mathrm{d}}{\mathrm{d}x''}\delta''(0) &= 0 \end{aligned}$$

giving the deflection and slope of the beam at point B.

$$\delta''_{yx1} = -\frac{F_{x''} L_1^2 L_2}{2EI_{z''1}} \sin\eta$$

Under the small angle assumption the angle of the deflection is equal to the slope of the beam.

$$\theta_{x''} = -\frac{F_{x''} L_1 L_2}{EI_{z''1}} \sin\eta$$

The EB-equation is then solved for B2, in a (ℓ, m)-coordinate system that is rotated with the angle η compared to the standard (x'', y'')-coordinate system.

$$\frac{\mathrm{d}^2}{\mathrm{d}\ell^2}\delta''(\ell) = -\frac{M_2}{EI_{z''2}} \quad \left| \begin{array}{rl} \text{BC:} & \delta''(0) = 0 \\ & \frac{\mathrm{d}}{\mathrm{d}\ell}\delta''(0) = \theta_{x''} \end{array} \right.$$

Solving this gives a deflection in the m-direction ($\delta_{\ell x''}$), that can then be translated into a deflection in the $x''-$ and $y''-$direction. The total deflection due to bending in x'' and y'' becomes:

$$\delta''_{xx} = -\delta''_{\ell x}\sin\eta = \frac{4F_{x''}}{EH}\left[\frac{L_2^3}{W_2^3} + 3\frac{L_1L_2^2}{W_1^3}\right]\sin^2\eta$$

$$\begin{aligned}\delta''_{yx} &= \delta''_{\ell x}\cos\eta + \delta''_{yx1} \\ &= -\frac{4F_{x''}}{EH}\left[\frac{L_2^3}{W_2^3} + 3\frac{L_1L_2^2}{W_1^3} + \frac{3}{2}\frac{L_1^2L_2}{W_1^3\cos\eta}\right]\cos\eta\sin\eta\end{aligned}$$

A force in the x''-direction would also lead to an elongation or compression of the beams

$$\delta''_{xxE} = \frac{F_{x''}}{EH}\left[\frac{L_1}{W_1} + \frac{L_2}{W_2}\cos^2\eta\right]$$

$$\delta''_{yxE} = \frac{F_{x''}}{EH}\frac{L_2}{W_2}\cos\eta\sin\eta$$

The compliance matrix elements is then found by the sum of the deflections divided by the force and results in the following elements.

$$\begin{aligned}C''_{11} &= \frac{4L_1^3}{EH^4}\left[\frac{\gamma^3}{\alpha^3} + 3\frac{\beta^3}{\alpha^2}\right]\sin^2\eta \\ &\quad + \frac{L_1}{EH^2}\left[\beta + \frac{\gamma}{\alpha}\cos^2\eta\right] \qquad (14)\end{aligned}$$

$$\begin{aligned}C''_{21} &= -\frac{4L_1^3}{EH^4}\left[\frac{\gamma^3}{\alpha^3} + 3\frac{\beta^3}{\alpha^2} + \frac{3}{2}\frac{\beta^3}{\alpha\cos\eta}\right]\cos\eta\sin\eta \\ &\quad + \frac{L_1}{EH^2}\frac{\gamma}{\alpha}\cos\eta\sin\eta \qquad (15)\end{aligned}$$

Force in the y''-direction

The bending moment for the two beams can be found to be $M_1 = -F_{y''}(L_1 + L_2\cos\eta - x'')$ and $M_2 = -F_{y''}(L_2 - \ell)\cos\eta$.

Solving the EB-equation for B1 gives the deflection and slope of B1 at point B. The equation and boundary conditions looks similar to the equation for a force in the x''-direction.

$$\delta''_{yy1} = \frac{F_{y''}}{EI_{z''1}}\left[\frac{1}{3}L_1^3 + \frac{1}{2}L_1^2L_2\cos\eta\right]$$

$$\theta_{y''} = \frac{F_{y''}}{EI_{z''1}}\left[\frac{1}{2}L_1^2 + L_1L_2\cos\eta\right]$$

The EB-equation for B2 can now be solved in the (ℓ, m)-coordinate system, using similar boundary conditions as for the force pointing in the x''-direction, afterwards the deflection is translated back to x'' and y'' components. The total deflection becomes due to bending becomes:

$$\begin{aligned}\delta''_{xy} &= -\delta''_{\ell y}\sin\eta \\ &= -\frac{4F_{y''}}{EH}\left[\frac{L_2^3}{W_2^3} + \frac{3}{2}\frac{L_1^2L_2}{W_1^3\cos\eta} + 3\frac{L_1L_2^2}{W_1^3}\right]\cos\eta\sin\eta\end{aligned}$$

$$\begin{aligned}\delta''_{yy} &= \delta''_{\ell y}\cos\eta + \delta''_{yy1} \\ &= \frac{4F_{y''}}{EH}\left[\frac{L_1^3}{W_1^3}\frac{1}{\cos^2\eta} + \frac{L_2^3}{W_2^3} + 3\frac{L_1^2L_2}{W_1^3\cos\eta} + 3\frac{L_1L_2^2}{W_1^3}\right]\cos^2\eta\end{aligned}$$

A force in the y''-direction would also give rise to an elongation or compression of the beams

$$\delta''_{xyE} = \frac{F''_y}{EH}\frac{L_2}{W_2}\cos\eta\sin\eta$$

$$\delta''_{yyE} = \frac{F''_y}{EH}\frac{L_2}{W_2}\sin^2\eta$$

Using the (α, β, γ)-notation the compliance matrix elements becomes:

$$\begin{aligned}C''_{12} &= -\frac{4L_1^3}{EH^4}\left[\frac{\gamma^3}{\alpha^3} + \frac{3}{2}\frac{\beta^3}{\alpha\cos\eta} + 3\frac{\beta^3}{\alpha^2}\right]\cos\eta\sin\eta \\ &\quad + \frac{L_1}{EH^2}\frac{\gamma}{\alpha}\cos\eta\sin\eta \qquad (16)\end{aligned}$$

$$\begin{aligned}C''_{22} &= \frac{4L_1^3}{EH^4}\left[\frac{\beta^3}{\cos^2\eta} + \frac{\gamma^3}{\alpha^3} + 3\frac{\beta^3}{\alpha\cos\eta} + 3\frac{\beta^3}{\alpha^2}\right]\cos^2\eta \\ &\quad + \frac{L_1}{EH^2}\frac{\gamma}{\alpha}\sin^2\eta \qquad (17)\end{aligned}$$

Force in the z''-direction

The bending moment for the two beams due to a force in z is $M_1 = F_{z''}(L_1 + L_2\cos\eta - x'')$ and $M_2 = F_{z''}(L_2 - \ell)$. Using the same procedure as for the x''- and y''-direction, it can be shown that the displacement due to bending is given by:

$$\delta''_{zz} = \frac{4F_{z''}}{EH^3}\left[\frac{L_1^3}{W_1} + \frac{L_2^3}{W_2} + 3\frac{L_1^2L_2}{W_1}\cos\eta + 3\frac{L_1L_2^2}{W_1}\cos^2\eta\right]$$

Since a force is applied orthogonal to the bend on the cantilever, a torsion is introduced. The angle of this torsion is directly proportional with the arm of the force multiplied with the length of the twisted beam.

$$\varphi_{z''} = \frac{F_{z''}L_1L_2}{GJ}\sin\eta$$

Where G is the shear modulus and J is the torsion constant.

$$G = \frac{1}{2}\frac{E}{1+\nu}$$

$$J = HW_1^3\left(\frac{1}{3} - \frac{64W_1}{\pi^5 H}\sum_{n=1,3,5}^{\infty}\frac{1}{n^5}\tanh\frac{n\pi H}{2W_1}\right)$$

Where ν is Poisson's ratio and $\mathbb{O}$ is the set of all odd natural numbers.
When calculating the displacement it is important to remember the to take the angle of the second beam into account again.

$$\delta''_{zzT} = \varphi_{z''}L_2\sin\eta = \frac{F_{z''}L_1L_2^2}{GJ}\sin^2\eta$$

Combining these and using the (α, β, γ)-notation the compliance matrix element becomes

$$C''_{33} = \frac{4L_1^3}{EH^4}\left[\beta + \frac{\gamma}{\alpha^3} + 3\frac{\beta}{\alpha}\cos\eta + 3\frac{\beta}{\alpha^2}\cos^2\eta + \frac{\beta^3}{\alpha^2}\frac{1+\nu}{2k_\beta}\sin^2\eta\right] \quad (18)$$

Where k_β is a function of β and is given by

$$k_\beta = \frac{1}{3} - \frac{64}{\pi^5\beta}\sum_{n=1,3,5}^{\infty}\frac{1}{n^5}\tanh\frac{n\pi\beta}{2}$$

Due to the assumption of small angles, and the 1D model used, there are no contributions to the x''- and y''-displacements as a result of a force in the z''-direction and vice versa.

Appendix II

Three macroscopic cantilevers were printed in Polylactic Acid (PLA) ($E = 2.347$ GPa [33] and $\nu = 0.33$ [34]) using an Ultimaker 2 3D-printer. The dimensions of the cantilevers are shown in Table 1. A cantilever was secured on a vertical post mounted on a z-stage (resolution 5 µm) so that the cantilever tip was resting in near-contact with a high precision scale (resolution 0.1 N). While the cantilever was engaged on the scale and then disengaged, the resulting force was measured. The results are summarized in Figure 6.

Initially during engagement, the straight cantilever width sliding contact (Figure 6 a) follows the theoretical line for C_{zz}^{-1}, which is indicative of sliding contact. The small discontinuities in the force-deflection curve is likely related to a stick-slip phenomenon caused by the macroscopic roughness of the surface. As the engage depth increases the cantilever starts to plastically deform, resulting in the contact force tapering off. The disengage shows a large hysteresis, some of which is likely caused by plastic deformation, while the rest is most likely caused by some phenomena not treated here. The stick-slip effect is not visible during disengage where the force deflection curve resembles a pure sliding for engage depth less than 3 mm.

		Cantilever contact type		
Dimension	Unit	Sliding	Stick-slip	Static
L_1	(mm)	60	60	60
L_2	(mm)	30	30	30
W_1	(mm)	3.9	1.9	1.9
W_2	(mm)	3.9	1.9	1.9
H	(mm)	4.1	5.1	5.1
η	(deg)	0	90	140
θ	(deg)	0	45	70

Table 1: Dimensions of the straight cantilever, expected to form a sliding contact, and the two bent cantilevers, expected to form stick-slip and static contact respectively, used in the experiment.

The bent cantilever with static contact (Figure 6 c) shows a very similar behaviour, where the contact force increases almost linearly with the engage depth. Similar to the sliding contact some plastic deformation seems to occur. Unlike the sliding contact case, there are no sign of the scale roughness, supporting the notion that this contact is indeed static. The hysteresis observed for the static contact is reduced to only the apparent plastic deformation.

The bent cantilever with stick-slip (Figure 6 b) shows a more pronounced "sawtooth" like behaviour, where the contact force increases linearly in phases, with a partial release of tension in between. The tension is released as the transverse force exceeds the friction force and the cantilever tip slides on the surface. Each build-up follows the slope of K_{zz} (static contact), but with each release the force drops to the slope of C_{zz}^{-1} (sliding contact).

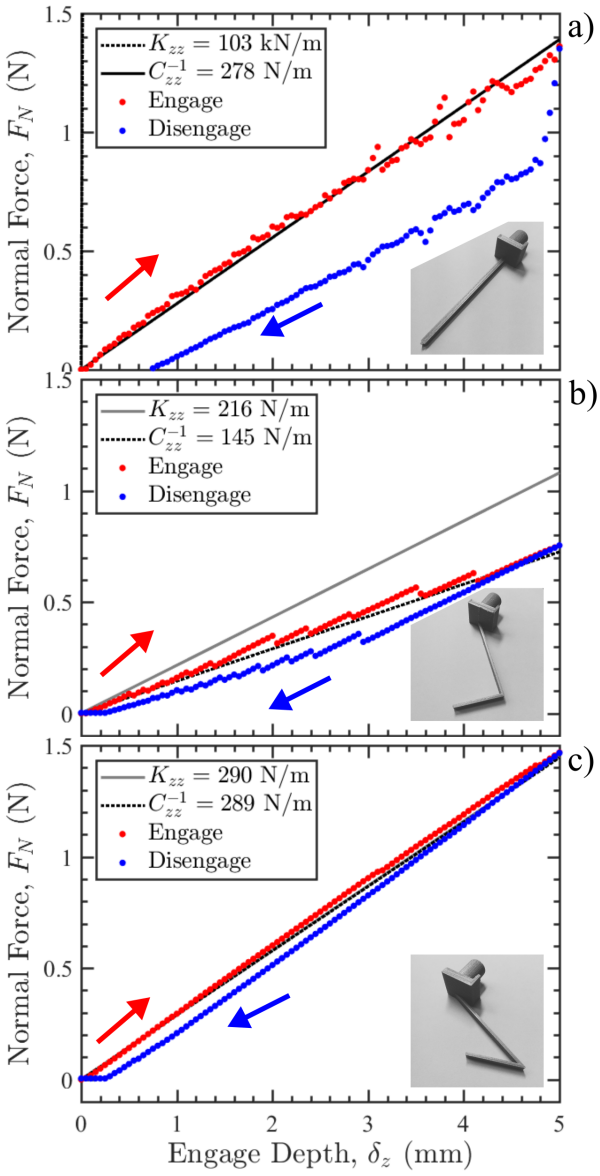

Figure 6: Normal force as a function of engage depth for macroscopic 3D printed cantilevers made of Polylactic Acid (PLA). A picture of the cantilever is shown in each plot. The full and dotted lines show the expected force if the stiffness is given by K_{zz} or C_{zz}^{-1} respectively. Both K_{zz} and C_{zz}^{-1} are calculated analytically. The red and blue dots indicate measured force during engagement and disengagement respectively. a) Straight cantilever expected to form a sliding contact. K_{zz} is so large that the corresponding line is on top of the y-axis. b) Bent cantilever expected to form a stick-slip contact. c) Bent cantilever expected to form a static contact.

Appendix III

In the calculations for Section 4 and 5 the following parameter design space was considered:

$$\begin{aligned} \theta &\in [0^\circ,\ \arccos(2/\sigma)] & \Delta\theta &= 1^\circ \\ \eta &\in [0^\circ,\ \arccos(2/\sigma) + \theta] & \Delta\eta &= 1^\circ \\ \alpha &\in [1.5,\ 2.5] & &\text{with 41 steps} \\ H &\in [2,\ 12] \times d & &\text{with 51 steps} \\ W_1 &\in [1,\ \sigma\cos\theta - 1] \times d & &\text{with 51 steps} \end{aligned}$$

In the case where $\arccos(2/\sigma) > 75^\circ$, the upper bounds on the angles θ and η were replaced with 75° and $75^\circ + \theta$ respectively. Variable limits on the parameters ensured that calculations on physically unfeasible designs were avoided, which drastically reduced the number of calculations at small values of σ. The following parameters were kept constant during the calculations:

$$\begin{aligned} W_2 &= d \\ L_T &= 12.2\ \mu\text{m} \\ \phi &= 30^\circ \\ C_{zz}^{-1} &= 13.1\ \text{N/m} \end{aligned}$$

For every permutation of α, θ and η, the engage stiffness and the vibration tolerance were calculated for all combinations of W_1 and H. Values of W_1 and H resulting in 13.1 N/m engage stiffness were identified using linear interpolation between neighboring grid points.

The optimization runs through all parameters by going through nested for-loops in the order θ, η and α going from outer to inner for-loop. Thus for any combination of θ and η, all values of α are visited before η is incremented by one step. This repeats until all values of η have been visited, at which point θ is incremented by one step.

Based on the results in Section 5.1, we know the highest vibration tolerances are found at large angles. Assuming the global maximum of the vibration tolerance is also the only maximum, a large run-time improvement can be achieved by looping through the angles in decreasing order and terminating the for-loop if the vibration tolerance in a step is lower than in the preceding step.

References

[1] F. Wenner. A method of measuring earth resistivity. *Bulletin of the Bureau of Standards*, 12:469–478, 1915.

[2] L. B. Valdes. Resistivity Measurements on Germanium for Transistors. *Proceedings of the IRE*, 42(2):420–427, 1954.

[3] F. M. Smits. Measurement of Sheet Resistivities with the Four-Point Probe. *Bell System Technical Journal*, 37(3):711–718, 1958.

[4] I Miccoli, F Edler, H Pfnür, and C Tegenkamp. The 100th anniversary of the four-point probe technique: the role of probe geometries in isotropic and anisotropic systems. *Journal of Physics: Condensed Matter*, 27(22):223201, may 2015.

[5] A. K. Wong. Microlithography: trends, challenges, solutions, and their impact on design. *IEEE Micro*, 23(2):12–21, March 2003.

[6] C. L. Petersen, R. Lin, D. H. Petersen, and P. F. Nielsen. Micro-scale sheet resistance measurements on ultra shallow junctions. In *2006 14th IEEE International Conference on Advanced Thermal Processing of Semiconductors*, pages 153–158, Oct 2006.

[7] Trudo H. Clarysse, Alain Moussa, Frederik Leys, Roger Loo, Wilfried Vandervorst, Mark C. Benjamin, Robert J. Hillard, Vladimir N. Faifer, Michael I. Current, Rong Lin, and et al. Accurate sheet resistance measurement on ultra-shallow profiles. *MRS Proceedings*, 912:0912–C05–07, 2006.

[8] Trudo Clarysse, Alain Moussa, Brigitte Parmentier, Janusz Bogdanowicz, Wilfried Vandervorst, Hugo Bender, Markus Pfeffer, Martin Schellenberger, Peter F. Nielsen, Sune Thorsteinsson, Rong Lin, and Dirch Petersen. Photovoltage versus microprobe sheet resistance measurements on ultrashallow structures. *Journal of Vacuum Science & Technology B*, 28(1):C1C8–C1C14, 2010.

[9] Dirch H. Petersen, Ole Hansen, Torben M. Hansen, Peter Bøggild, Rong Lin, Daniel Kjær, Peter F. Nielsen, Trudo Clarysse, Wilfried Vandervorst, Erik Rosseel, Nick S. Bennett, and Nick E. B. Cowern. Review of electrical characterization of ultra-shallow junctions with micro four-point probes. *Journal of Vacuum Science & Technology B: Microelectronics and Nanometer Structures*, 28(1):C1C27, 2010.

[10] T. Clarysse, J. Bogdanowicz, J. Goossens, A. Moussa, E. Rosseel, W. Vandervorst, D. H. Petersen, R. Lin, P. F. Nielsen, Ole Hansen, G. Merklin, N. S. Bennett, and N. E.B. Cowern. On the analysis of the activation mechanisms of sub-melt laser anneals. *Materials Science and Engineering B: Solid-State Materials for Advanced Technology*, 154-155(1-3):24–30, 2008.

[11] C. L. Petersen, F. Grey, I. Shiraki, and S. Hasegawa. Microfour-point probe for studying electronic transport through surface states. *Applied Physics Letters*, 77(23):3782–3784, 2000.

[12] C. L. Petersen, T. M. Hansen, P. Boggild, A. Boisen, O. Hansen, T. Hassenkam, and F. Grey. Scanning microscopic four-point conductivity probes. *Sensors and Actuators, A: Physical*, 96(1):53–58, 2002.

[13] Dirch H. Petersen, Ole Hansen, Torben M. Hansen, Peter R E Petersen, and Peter Bøggild. Static contact micro four-point probes with <11 nm positioning repeatability. *Microelectronic Engineering*, 85(5-6):1092–1095, 2008.

[14] S. Keller, S. Mouaziz, G. Boero, and J. Brugger. Microscopic four-point probe based on su-8 cantilevers. *Review of Scientific Instruments*, 76(12):125102, 2005.

[15] J K Kim, Y S Choi, and D W Lee. Surface-adaptable all-metal micro-four-point probe with unique configuration. *Journal of Micromechanics and Microengineering*, 25(7):075023, jun 2015.

[16] Sune Thorsteinsson, Fei Wang, Dirch H. Petersen, Torben Mikael Hansen, Daniel Kjær, Rong Lin, Jang Yong Kim, Peter F. Nielsen, and Ole Hansen. Accurate microfour-point probe sheet resistance measurements on small samples. *Review of Scientific Instruments*, 80(5), 2009.

[17] Dirch H. Petersen, Ole Hansen, Rong Lin, and Peter F. Nielsen. Micro-four-point probe Hall effect measurement method. *Journal of Applied Physics*, 104(1), 2008.

[18] Maria-Louise Witthøft, Frederik W. Østerberg, Janusz Bogdanowicz, Rong Lin, Henrik H. Henrichsen, Ole Hansen, and Dirch H. Petersen. A variable probe pitch micro-hall effect method. *Beilstein Journal of Nanotechnology*, 9:2032–2039, 2018.

[19] Alberto Cagliani, Frederik W. Østerberg, Ole Hansen, Lior Shiv, Peter F. Nielsen, and Dirch H. Petersen. Breakthrough in current-in-plane tunneling measurement precision by application of multi-variable fitting algorithm. *Review of Scientific Instruments*, 88(9), 2017.

[20] Dirch Hjorth Petersen. *Micro Four-Point Probe and Micro Hall Effect: Methods for Reliable Electrical Characterization of Ultra-Shallow Junctions*. PhD thesis, 2009.

[21] Trudo H. Clarysse, Alain Moussa, Frederik Leys, Roger Loo, Wilfried Vandervorst, Mark C. Benjamin, Robert J. Hillard, Vladimir N. Faifer, Michael I. Current, Rong Lin, and Dirch H. Petersen. Accurate Sheet Resistance Measurement on Ultra-Shallow Profiles. *MRS Proceedings*, 912:1–7, 2006.

[22] Trudo Clarysse, Alain Moussa, Brigitte Parmentier, Janusz Bogdanowicz, Wilfried Vandervorst, Hugo Bender, Markus Pfeffer, Martin Schellenberger, Peter F. Nielsen, Sune Thorsteinsson, Rong Lin, and Dirch Petersen. Photovoltage versus microprobe sheet resistance measurements on ultrashallow structures. *Journal of Vacuum Science & Technology B, Nanotechnology and Microelectronics: Materials, Processing, Measurement, and Phenomena*, 28(1):C1C8–C1C14, 2010.

[23] D. M. A. Mackenzie, K. G. Kalhauge, P. Whelan, F. W. Østergaard, I. Pasternak, W. Strupinski, P. Bøggild, P. U. Jepsen, and D. H. Petersen. Wafer-scale quality assessment of graphene using micro four-point probe mapping. *Manuscript submitted for publication in Nanotechnology*, 2019.

[24] Henrik H. Henrichsen, Ole Hansen, Daniel Kjær, Peter F. Nielsen, Fei Wang, and Dirch H. Petersen. Precision of single-engage micro Hall effect measurements. *2014 International Workshop on Junction Technology, IWJT 2014*, pages 55–58, 2014.

[25] D. C. Worledge. Reduction of positional errors in a four-point probe resistance measurement. *Applied Physics Letters*, 84(10):1695–1697, 2004.

[26] Daniel Kjaer, Ole Hansen, Frederik Westergaard Lsterberg, Henrik Hartmann Henrichsen, Christian Markvardsen, Peter Folmer Nielsen, and Dirch Hjorth Petersen. Characterization of positional errors and their influence on micro four-point probe measurements on a 100 nm Ru film. *Measurement Science and Technology*, 26(9), 2015.

[27] Kristoffer G Kalhauge, Henrik H Henrichsen, Fei Wang, Ole Hansen, and Dirch H Petersen. Vibration tolerance of micro-electrodes. *Journal of Micromechanics and Microengineering*, 28(9):095010, jun 2018.

[28] Fei Wang, Dirch H Petersen, Helle V Jensen, Christian Hansen, Dennis Mortensen, Lars Friis, and Ole Hansen. Three-way flexible cantilever probes for static contact. *Journal of Micromechanics and Microengineering*, 21:085003, 2011.

[29] Stephen Timoshenko and J N Goodier. *Theory of Elasticity*. McGraw-Hill, New York, third edition, 1970.

[30] Jie Liu, Han Jiang, Qian Cheng, and Chaoming Wang. Investigation of nano-scale scratch and stick-slip behaviors of polycarbonate using atomic force microscopy. *Tribology International*, 125:59 – 65, 2018.

[31] COMSOL. Comsol homepage. `http://COMSOL.com/`, 11 2019.

[32] Stephen D. Senturia. *Microsystem Design*. Springer, New York, NY, 1 edition, 2001.

[33] Ultimaker. Techinical data sheet pla. `https://ultimaker.com/download/74599/UM180821%20TDS%20PLA%20RB%20V10.pdf`, 11 2019.

[34] Kuentz. Additive manufacturing and characterization of polylactic acid (pla) composites containing metal reinforcements. `https://ntrs.nasa.gov/archive/nasa/casi.ntrs.nasa.gov/20160010284.pdf`, 11 2019.